Martin Buschmann, BSc

Evaluation and implementation of a grid-based Boltzmann equation solver for dose calculation in clinical radiation therapy treatment planning

MASTER THESIS

For obtaining the academic degree
Diplom-Ingenieur

Master Programme of
Technical Physics

Graz University of Technology

Supervisor:

Assoc.Prof. Dipl.-Phys. Dr.rer.nat. Wolfgang Sprengel

Institute of Materials Physics

Graz, March 2014

Deutsche Fassung:
Beschluss der Curricula-Kommission für Bachelor-, Master- und Diplomstudien vom 10.11.2008
Genehmigung des Senates am 1.12.2008

EIDESSTATTLICHE ERKLÄRUNG

Ich erkläre an Eides statt, dass ich die vorliegende Arbeit selbstständig verfasst, andere als die angegebenen Quellen/Hilfsmittel nicht benutzt, und die den benutzten Quellen wörtlich und inhaltlich entnommenen Stellen als solche kenntlich gemacht habe.

Graz, am ……. ……..
(Unterschrift)

Englische Fassung:

STATUTORY DECLARATION

I declare that I have authored this thesis independently, that I have not used other than the declared sources / resources, and that I have explicitly marked all material which has been quoted either literally or by content from the used sources.

……. ……..
date (signature)

Contents

Danksagung

Diese Masterarbeit wurde am Institut für Materialphysik der TU Graz in Zusammenarbeit mit dem Univ.-Klinikum für Strahlentherapie-Radioonkologie Graz erstellt. Ganz besonders möchte ich mich bei Dr. Peter Winkler und Dipl.-Ing. Stefan Odreitz bedanken, die mir diese Arbeit ermöglicht haben und mich während der Durchführung sehr gut betreut haben. Auch bei allen anderen im Team der Klinik möchte ich mich bedanken, die mir immer zur Seite standen und bei der Lösung vieler Probleme weiterhalfen.

Dank gebührt Assoc.Prof. Dr. Wolfgang Sprengel für die Betreuung der Arbeit. Er nahm sich viel Zeit für anregende Diskussionen, die oft auch über das Gebiet dieser Arbeit und die Physik hinausgingen.

Mein besonderer Dank geht an meine Eltern, Susanne und Hans Buschmann. Mein Studium wäre ohne ihre moralische und finanzielle Unterstützung nicht möglich gewesen. Sie motivierten mich stets und zeigten Interesse an meinem Fach, wenn auch es mir nicht immer möglich war, komplexe physikalische Sachverhalte verständlich zu erklären. Auch bei meiner restlichen Familie möchte ich mich bedanken und hier insbesondere bei meinem Bruder Andreas. Als älterer Bruder war er immer eine große Orientierungshilfe für mich.

Zu guter letzt spreche ich ein großes Dankeschön an all meine Freunde und Studienkollegen aus. Ihre Freundschaft und Unterstützung gaben mir Kraft in jeder Phase meines Studiums.

List of abbreviations

AAA	Anistropic Analytical Algorithm
AXB	Acuros XB
CCCS	Collapsed Cone Convolution Superposition
^{60}Co	Cobalt-60
CPE	charged particle equilibrium
CT	computer tomograph
DTA	distance to agreement
DVH	dose volume histogram
GAI	Gamma agreement index
GBBS	grid-based Boltzmann solver
HU	Hounsfield unit
ICRP	International Commission on Radiological Protection
IMRT	Intensity modulated radiotherapy
ICRU	International Commission on Radiological Units and Measurements
LBTE	linear Boltzmann transport equations
MC	Monte Carlo
MLC	multi leaf collimator
MU	monitur unit
OAR	organs at risk
OBI	On Board Imager
PMMA	Poly(methyl methacrylate), acrylic glass
PTV	planning target volume
SSD	source surface distance
TLD	thermoluminescence dosimeter
TPS	treatment planning system
VMAT	Volumetric modulated arc therapy

Abstract

In modern external radiation therapy treatment planning of cancer patients, the dose distribution in a patient is calculated based on a three-dimensional CT scan. The Acuros XB dose calculation algorithm is a new algorithm, which is based on the solution of the linear Boltzmann transport equation and has recently been implemented in a commercial treatment planning system. The aim of this thesis, was to configure the algorithm in the treatment planning system and evaluate its accuracy in dose calculation for use in routine clinical treatment planning. The algorithm was configured by adjusting the physical parameters, which model the radiation source. The accuracy of the algorithm was evaluated by comparing dose calculations to dosimetric measurements and well-established algorithms. The measurements were performed in partly self-developed phantoms, composed of heterogeneous materials, upon exposure to ionizing photon radiation from a medical linear accelerator. The dosimetric impact of using the Acuros XB algorithm for treatment planning in clinical cases was assessed by calculating dose distributions on datasets of real patients.

The dose calculations of Acuros XB in inhomogeneous phantoms were in very good agreement with the measurements. The performance of Acuros XB was equal or better compared to the established algorithm in the treatment planning system. However, the Acuros XB algorithm showed tendencies to underestimate the dose in some material environments, e.g. in bone tissue. The results of the dosimetric study on clinical cases suggest that the mean dose calculated by Acuros XB in the target volume and the surrounding organs of head and neck tumor patients is 1-3% lower compared to two established algorithms. The dose conformity to the target volume in lung tumor patients did not show any significant change when recalculated by Acuros XB.

Kurzfassung

In der modernen Bestrahlungsplanung für Tumorpatienten wird die Dosisverteilung im Patienten auf Basis eines dreidimensionalen CT Scans berechnet. Der Dosisberechnungsalgorithmus Acuros XB ist ein neuer Algorithmus, der auf der Lösung der linearen Boltzmann-Transport-Gleichung basiert, und kürzlich in einem kommerziellen Bestrahlungsplanungssytem implementiert wurde. Das Ziel dieser Arbeit war die Konfiguration des Algorithmus' im Bestrahlungsplanungssystem und die Evaluierung der Genauigkeit der Dosisberechnung für die klinische Routine. Der Algorithmus wurde durch Anpassung der physikalischen Parameter, die die Strahlungsquelle modellieren, konfiguriert. Die Genauigkeit des Algorithmus wurde evaluiert durch den Vergleich von Dosisberechnungen mit dosimetrischen Messungen und etablierten Algorithmen. Die Messungen wurden in, zum Teil eigens dafür entwickelten, Phantomen aus heterogenen Materialien bei Bestrahlung mit ionisierender Photonenstrahlung aus einem medizinischen Linearbeschleuniger durchgeführt. Der dosimetrische Einfluss der Verwendung des Acuros XB Algorithmus für die Bestrahlungsplanung klinischer Fälle wurde anhand von Dosisberechnungen auf Datensätzen realer Patienten untersucht.

Die Dosisberechnungen des Acuros XB in inhomogenen Phantomen waren in sehr guter Übereinstimmung mit den Messungen. Die Genauigkeit des Acuros XB war gleich oder besser im Vergleich zum etablierten Algorithmus im selben Bestrahlungsplanungssystem. Jedoch zeigte der Acuros XB Algorithmus Tendenzen die Dosis in manchen Materialumgebungen zu unterschätzen, z.B. in Knochengewebe. Die Ergebnisse der dosimetrischen Studie an klinischen Patienten legen nahe, dass die mittlere Dosis im Zielvolumen und den Risikoorganen von Patienten mit Kopf-Hals-Karzinom, berechnet durch Acuros XB, 1-3% niedriger ist im Vergleich mit zwei etablierten Algorithmen. Die Dosiskonformität um das Zielvolumen in Lungen-Tumor-Patienten zeigte keine signifikante Änderung bei der Neuberechnung mit Acuros XB.

1 Introduction

In modern radiation therapy a treatment plan is created in an individualized optimization process with the aim of delivering maximum dose to the tumor volume while sparing surrounding healthy tissue. The dose distribution in the patient is simulated by a dose calculation algorithm on a three-dimensional CT dataset. For optimal dose delivery with high accuracy, the tissue heterogeneities in the patient have to be accounted for in the dose calculation [1]. This presents a big challenge for the algorithms.

Several different dose calculation algorithms are used in clinical environments. In earlier times mostly pencil beam algorithms were employed. These were replaced by algorithms based on convolution and superposition of fluence distributions with the help of pre-computed scattering kernels. Occasionally Monte Carlo (MC) methods are in clinical use. The dose calculation algorithms have to fulfill stringent accuracy criteria, especially in the presence of tissue heterogeneities. Additionally, the calculation time should be kept short not to delay the clinical routine workflow, which can be an issue for MC methods.

The algorithm Acuros XB (Varian Medical Systems, Palo Alto, CA, USA) uses a novel approach for dose calculation in external radiation treatment planning. The algorithm calculates deterministic solutions to the **coupled system of linear Boltzmann transport equations** (LBTE) for photons and electrons by discretizing the particle fluences in space, energy and angle. The concept of grid-based LBTE solvers was first used for neutron transport problems [2] and just recently has been applied to radiation oncology physics [3, 4]. The motivation for the use of LBTE solvers in radiotherapy is the high accuracy of dose calculation with less computational effort than MC methods.

The Acuros algorithm was developed based on the prototype software Attila [5] by Transpirce Inc. (Gig Harbor, WA, USA) [6]. The Acuros XB (AXB) algorithm for external radiotherapy has been implemented in the Eclipse treatment planning system (Varian Medical Systems) in 2010 [7].

The AXB algorithm has recently become available for treatment planning at the Department of Therapeutic Radiology and Oncology at the Medical University of Graz. In this study its performance and accuracy was evaluated for clinical photon radiation therapy. This was achieved by benchmarking against established algorithms and dosimetric measurements.

Summary of previous research

Since the release of the Acuros algorithm, its accuracy was validated computationally and experimentally in several studies. Most of the verifications were performed through comparison to MC methods, which present a gold standard in the accuracy of dose calculations, and superposition/convolution algorithms (AAA and CCCS, see sec. 2.3), which are well-established in clinical routine. A good overview of the evaluation studies of AXB was published in a review by Kan et. al. [8].

The AXB was validated in homogeneous water in simple geometries [7,9–11]. The AXB calculations were compared to measured data, MC simulations and superposition/convolution methods. The agreement of AXB was found to be better than 2%, comparable to the established algorithms.

The next step was the verification with inhomogeneous simple geometric phantoms using single open fields of different photon energies [6,7,10,12–17]. The studies report discrepancies of less than 2% in most cases between AXB and MC. Some studies compared the accuracy of AXB to AAA [12–17] and found larger differences between AAA and MC in the presence of lung, air and high density materials.

Some investigations were performed to asses the accuracy of AXB using multiple clinical setup fields against MC [6] and measurements [11,14,18–20] for various tumor locations. The MC study showed excellent agreement between AXB and MC. The experimental studies showed good agreement ($\pm 5\%$) of measured and AXB-calculated point doses and all recommendations regarding dose accuracy were met by AXB in heterogeneous phantoms, except for one study [18]. The experimental validations also compared the accuracy between AXB and AAA and found equivalent or better accuracy for AXB. The AXB algorithm performed better than near air/tissue interfaces for small fields.

Various studies were performed to evaluate the dosimetric impact of the calculation of clinical treatment plans with AXB [17,21–23]. In these studies treatment plans for lung cancer, breast cancer and nasopharyngeal carcinomas, originally calculated by AAA, were recalculated by AXB. The various investigations show that in general AXB predicts lower doses to organs at risk (OAR) and target volume than AAA. The difference is about 1-2% for soft tisse and about 4% for bone.

Aim of this work

The aim of this work was to implement and evaluate the Acuros XB algorithm for routine clinical radiation therapy treatment planning in the Eclipse

treatment planning system (TPS). The workflow and the structure of this thesis consist of the following steps:

Part 1: Implementation and configuration

Before the AXB algorithm can be used for dose calculations, it has to be configured properly in the TPS. This is achieved by adjusting the source model of the algorithm, which models the radiation produced by a real medical linear accelerator. The model is described by several physical parameters such as the bremstarget spot size and the electron contamination dose. The optimal values for the parameters have to be determined by optimization processes and by comparison of calculated beam data to dose measurements in a water phantom.

Part 2: Phantom measurements

The next step is to assess the accuracy in dose calculation of the AXB algorithm experimentally. Several different dosimetry techniques are used to measure the absorbed dose in phantoms upon exposure to high energy photon radiation from a medical linac:

- ion chamber dosimetry
- dosimetry with radiochromic films
- diode dosimetry
- thermoluminescence dosimetry

The dose distributions resulting from these radiation fields are calculated by the AXB algorithm in the TPS on CT scans of the phantoms. The phantoms used were developed in this thesis and are composed of heterogeneous materials to study the algorithms's treatment of inhomogeneities and interfaces in dose calculation.

First, simple geometric phantoms and single open fields are used for the experiments. Different material situations are realized and its effect on the calculated dose distributions are investigated. Second, measurements in an anthropomorphous phantom with multiple clinical radiation fields are performed to investigate the accuracy of AXB in a clinical application.

Part 3: Dosimetric study for clinical cases

The last step is the assessment of the dosimetric implications of the use of AXB for the calculation of clinical treatment plans on real patients. The differences in dose distributions calculated by AXB and superposition/convolution methods are analyzed for a group of patient datasets with head and neck tumors and lung tumors.

In all steps the algorithm's accuracy and performance was benchmarked against the Analytical Anisotropic Algorithm (AAA), which is a superposition/ convolution-type algorithm currently in use for routine treatment planning in the Eclipse TPS at the department. In chapter 6, where clinical cases are investigated, comparisons to the Collapsed Cone Convolution Superposition (CCCS) algorithm in the Pinnacle TPS (Philips, Amsterdam, Netherlands) were also made.

2 Principles of dosimetry and dose calculation

2.1 Basics of radiation physics

2.1.1 Interactions of photons with matter

Here the various possible types of photon interactions with absorbing media are discussed. Photon radiation is indirectly ionizing radiation, which transfers its energy to kinetic energy of charged secondary particles. Those secondary particles then deposit their energy in the medium. Some, but not all, photon interactions play an important role in medical radiation physics [24].

The photon may interact with a tightly bound orbital electron, with the nucleus or with a free orbital electron of an absorber atom. A tightly bound electron can be considered as an electron with a binding energy of the order of the photon energy. The binding energy of a free electron is much smaller than the photon energy [25]. The probability of a specific interaction depends on the energy of the photon and the density and atomic number of the absorber, and is described by an interaction cross section [24, 25]. After the interaction the photon may be absorbed completely by transferring all its energy (photoelectric effect) or it may be scattered coherently (Rayleigh scattering) or incoherently (Compton effect). Figure 2.1 depicts the different interactions an photon can undergo with an electron.

Photoelectric effect

The photoelectric effect is the interaction of a photon with a tightly bound orbital electron. In this process, the photon is absorbed. Its energy is transferred to the electron, which is ejected as a photoelectron from the bound shell. The photoelectron causes further interactions in the absorber. The incoming photon needs to have sufficient energy to overcome the electron's binding energy E_b and the excess energy is transferred into kinetic energy of the photoelectron E_k

$$E_k = h\nu - E_b \tag{1}$$

The interaction creates a vacancy in the bound shell, which is quickly filled by rearrangement of the other electrons in the atom. In this process a characteristic X-ray or an Auger electron is emitted. For photons with high enough energy the most probable interaction is with the K-shell electrons.

The photoelectric effect is the predominant form of interaction for gamma rays with relatively low energies, which are used in radiography. The process

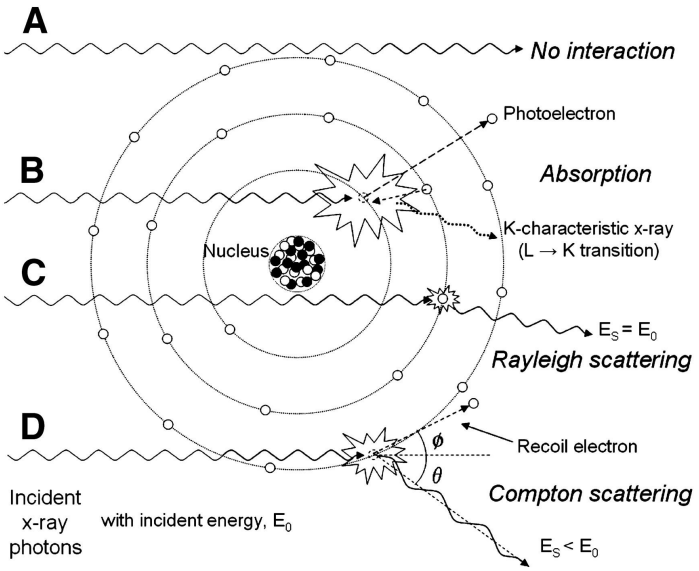

Figure 2.1: Illustrative summary of photon interactions: (A) no interaction. (B) photoelectric effect. (C) Rayleigh scattering. (D) Compton scattering. Pair production and photonuclear effect are not shown [26]

is enhanced for absorber materials with high atomic number Z. A rough approximation for the probability of the photoelectric absorption interaction is given by

$$\tau \cong const. \times \frac{Z^n}{E_\gamma^{3.5}} \tag{2}$$

where the exponent n varies between 4 and 5 [27]. The Z-dependence of the photon absorption probability is the main reason for the use of high-Z-materials (e.g. lead) in gamma radiation shielding.

Coherent (Rayleigh) scattering

In coherent (or Rayleigh) scattering the photon is scattered elastically on the bound electrons of the atom. The scattered photon conserves its original energy after the interaction and the absorber atom is neither excited nor ionized in the process. The direction of the photon is changed by a scattering angle θ in the scattering event. The whole absorber atom absorbs the transferred momentum, but the recoil energy is very small.

As no energy transfer occurs from the photon to the atom, Rayleigh scattering plays no role in the energy transfer coefficient, but it contributes

to the attenuation coefficient.

Coherent scattering plays a significant role only for low energy photons (below a few hundred keV) and its relative importance is larger in high-Z materials. The atomic cross section is given by [25]

$$\sigma_R \propto \left(\frac{Z}{h\nu}\right)^2 . \tag{3}$$

In tissue the relative importance of Rayleigh scattering is small compared to other interactions and contributes only a few percent to the attenuation coefficient.

Incoherent (Compton) scattering

Compton scattering occurs when a photon interacts with a loosely bound ('free') orbital electron of an absorber atom. The photon $h\nu$ loses part of its energy to the recoil electron, assumed to be at rest initially. The scattered photon $h\nu'$ has a lower energy than the original photon $h\nu' < h\nu$ and is deflected through a scattering angle θ. The scattering angle θ is defined as the angle between the original photon direction and the scattered photon direction, it ranges from 0° (forward scattering) to 180° (back scattering). By using the conservation of energy and momentum and neglecting the binding energy of the electron ($E_b \ll h\nu$), the relation between photon energies and scattering angle can be expressed as

$$h\nu' = h\nu \frac{1}{1 + \frac{h\nu}{m_0c^2}(1 - \cos\theta)} \tag{4}$$

where m_0c^2 is the rest mass energy of the electron [27].

After the interaction the recoil electron (Compton electron) is ejected from the atom with the kinetic energy E_k, which is given by

$$E_k = h\nu \frac{1 - \cos\theta}{\frac{m_0c^2}{h\nu} + 1 - \cos\theta} \tag{5}$$

The recoil angle ϕ is defined as the angle between the incident photon direction and the recoil electron direction. It ranges from $\phi = 0°$ to $\phi = 90°$. The maximum energy transfer to the Compton electron is reached at $\theta = 180°$ (photon backscatter).

The probability of Compton scattering per atom is proportional to the atomic number Z (i.e. to the number of electrons available for scattering)This process is of large relative importance in human tissue, as it has a high

electron density. There is no analytical expression for the energy dependence, but a rough estimate of the Compton cross section σ_c is given by [28]

$$\sigma_c \approx \rho \frac{Z}{A} \frac{1}{E_\gamma^n}, \quad n = 0.5 - 1. \tag{6}$$

The angular distribution of scattered photons is described by the Klein-Nishina formula for the differential scattering cross section $d\sigma/d\Omega$ [24].

Pair production

Pair production is a process, only possible when the photon energy exceeds twice the electron rest mass energy, $2m_0c^2 = 1.022$ MeV. In this process the photon interacts with the Coulomb field of a nucleus. The photon energy is transformed into mass energy of two particles, a electron-positron pair is created. The photon disappears and the excess energy above the required 1.022 MeV is transformed into kinetic energy of the particles involved. Shortly after the pair production, the positron will find another electron in the absorber material to annihilate with and two annihilation photons ($h\nu = 511$ keV) are produced as secondary particles. The probability of pair production is approximately proportional to the logarithm of the photon energy, $\log E_\gamma$, and Z^2/A.

Pair production can also occur in the Coulomb field of an orbital electron, this effect is called triplett production and the threshold energy is $4m_0c^2$. The energies typically used in diagnostic radiography are not sufficient for pair production, but the process occurs in radiotherapy with high enough energies.

Photonuclear reaction

Photonuclear reaction is a process, where a high energy photon is absorbed by the nucleus of an atom. This interaction leads to the emission of one or several protons or neutrons from the nucleus and thereby to a transformation of the nuclide to a, mostly unstable, reaction product. The energy threshold for a photonuclear reaction is of the order of 10 MeV and strongly depends on the reaction and the nucleus. The probability for photonuclear interaction is generally much smaller than for other photon interactions, and the cross section shows resonances at certain energies. Photonuclear reactions are negligible when examining photon attenuation in absorbers, but photonuclear reactions may induce radioactivity in radiotherapy treatment rooms by activation of structure materials, machine components or air. This may be present a health hazard for treatment personnel [25].

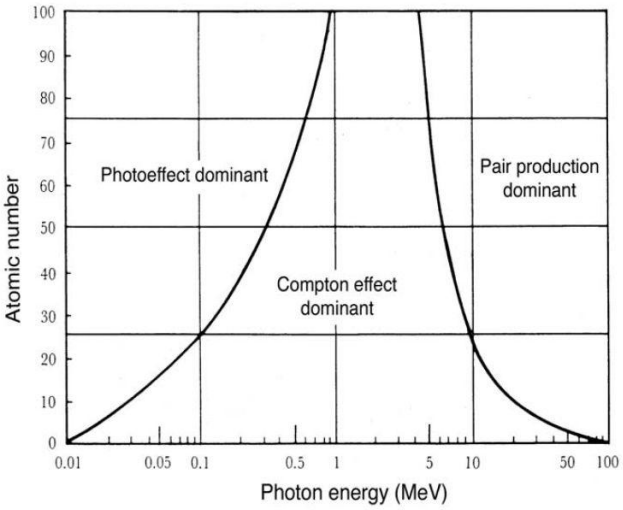

Figure 2.2: Relative importance of the three major forms of photon interactions as function of Z and photon energy $E_{h\nu}$ (see Ref. 25, page 37).

Table 1: Characteristics of the different photon interactions [28]

Interaction	f(Z,A)	f(E_γ)	secondary radiation	attenuation coeff.
Photoelectric effect	Z^4/A -$Z^{4.5}/A$	$1/E^{3.5}$ (E <<511 keV), $1/E$ (E >>511keV)	e^-, X-rays, UV, Auger e^-	τ
Compton scattering	Z/A	$1/E^{0.5}$ - $1/E$	γ, e^-	σ_C
Rayleigh scattering	$Z^{2.5}/A$	$1/E^2$	γ	σ_R
Pair production	Z^2/A	$\log E_\gamma$ ($E > 1.022$ MeV)	e^-, e^+	κ
Photonuclear reaction	resonance	$E_\gamma > E_{threshold}$	n, p, γ, fission	σ_{np}

Summary

For low photon energies the photoelectric effect is the predominant effect, at higher energies mainly the Compton effect occurs. Above energies of 20 MeV pair production becomes predominant in biological tissue (Z_{eff} =7.5). Figure 2.2 shows the predominant interaction as a function of photon energy and atomic number of the medium. Table 1 summarizes the characteristics of the photon interactions. For radiation therapy the dominant process is the Compton effect.

2.1.2 Photon beam attenuation

The intensity of a photon beam gets attenuated, when interacting with an absorber of thickness x according to

$$I(x) = I_0 e^{-\mu x}. \tag{7}$$

I_0 is the intensity of the beam before the interaction and μ is the linear attenuation coefficient, which depends on the beam energy and the absorber material (density ρ, mass number A, atomic number Z). The conventional unit for μ is cm^2/g. As the attenuation coefficient frequently shows a direct proportionality with the density, the attenuation is often expressed with the mass attenuation coefficient $\mu_m = \mu/\rho$ [25].

The attenuation coefficient μ can be expressed as a sum of the individual photon interaction contributions:

$$\mu = \tau + \sigma_R + \sigma_C + \kappa_{pair}(+\sigma_{pn}) \tag{8}$$

The last term σ_{pn}, which describes photonuclear reactions, is mostly negligible.

For the description of dosimetric effects two additional attenuation coefficients are needed, the energy transfer coefficient μ_{tr} and the energy absorption coefficient μ_{en}.

$$\mu_{tr} = \frac{\bar{E}_{tr}}{E_\gamma} \cdot \mu \tag{9}$$

$$\mu_{en} = \frac{\bar{E}_{en}}{E_\gamma} \cdot \mu \tag{10}$$

Here, $\bar{E}_{tr}$ is the average energy transferred to charged particles in the absorber and $\bar{E}_{en}$ is the average energy deposited by the charged particles in the absorber.

The energy transfer coefficient is also set up of the individual interaction contributions:

$$\mu_{tr} = \tau_{tr} + (\sigma_C)_{tr} + \kappa_{tr} \tag{11}$$

The two coefficients μ_{tr} and μ_{en} are related by

$$\mu_{en} = \mu_{tr}(1 - G) \tag{12}$$

where G is the radiative fraction. Rayleigh scattering does not contribute to the energy transfer coefficient and the energy absorption coefficient as the energy transfer is zero [25, 28].

The local energy absorption is mostly governed by the charged secondary particles produced by the primary interaction of the photons. The secondary photons, like scattering radiation and bremsstrahlung, which are produced during the interactions transport their energy away from the location of primary interaction due to their low interaction probability. These photons may even leave the absorber without interaction. This radiation does not contribute to local energy absorption, which is considered in the energy absorption coefficient μ_{en}. The radiative fraction G is defined as the mean

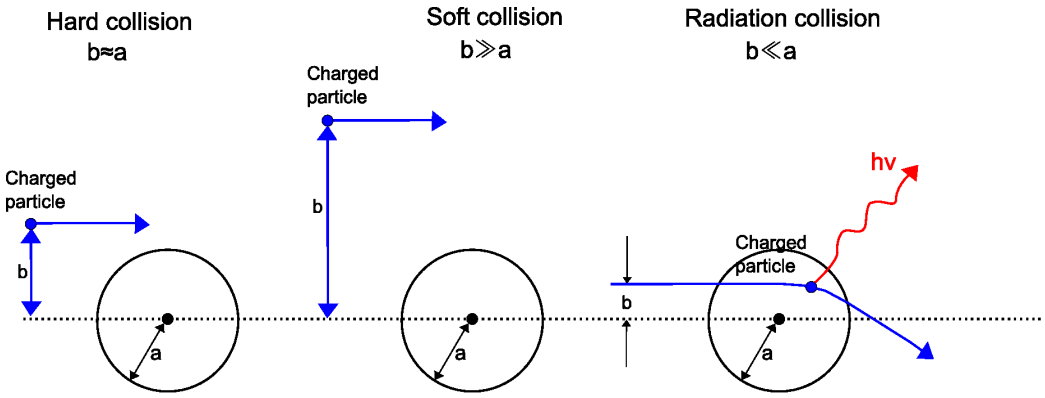

Figure 2.3: Three different types of collisions of a charged particle with an atom, depending on the impact parameter b and the atomic radius a.

fraction of the energy that is transferred through primary photon interactions to charged particles and then lost through various radiation processes. The corresponding dosimetric quantity to the energy absorption coefficient is the absorbed dose. For low photon energies the energy transfer coefficient and the energy absorption coefficient are almost equal [28].

2.1.3 Interactions of electrons with matter

Interactions of electrons with matter are not only important in electron therapy, but also in photon radiotherapy as secondary electrons are released after the primary interactions of photons (Compton effect). The electron interacts with the absorber atoms through its Coulomb electric field. Generally the energy transfer per interaction process is small, so a large number of interactions is necessary to transfer the kinetic energy of the particle, resulting in a continuous slowing down of the electron. The quantity used to describe this energy loss of a charged particle is the stopping power.

As the electron travels through an absorber, the Coulomb field of the electron interacts with the orbital electrons and the nucleus of an absorber atom. The type of interaction with an atom of radius a depends on the size of the impact parameter b (see Fig. 2.3). The impact parameter b is defined as the perpendicular distance between the electron path and the atomic nucleus [25]. Three cases can be distinguished:

- Soft collisions ($b \gg a$): Coulomb interaction of the incident electron with the orbital electrons of the atom, only a small amount of the kinetic energy is transferred

- Hard collisions ($b \approx a$): Coulomb interaction of the incident electron

with the orbital electrons of the atom, a substantial amount of the kinetic energy is transferred

- Radiation collisions ($b \ll a$): Coulomb interaction of the incident electron with the nuclear field of the atom, a radiative interaction takes place and the electron may lose a significant amount of energy by emitting a bremsstrahlung photon

Interactions with orbital electrons (soft and hard collisions)

In the case of a large impact parameter b the incident electron interacts with the whole electron shell. If no excitation or ionization occurs the electron loses only a small amount of its kinetic energy, it is elastically scattered. The electron changes its direction of motion and some momentum is transferred to the atom.

The incident electron may also transfer some of its kinetic energy, which leads to excitation or ionization of an orbital electron. The low energy secondary electron which may be released, will deposit its energy right at the site of interaction. The incident electron is inelastically scattered. These small-energy transfer interactions are called soft collisions.

As the impact parameter gets smaller the electron may have a direct impact interaction (binary collision) with a single orbital electron. Due to the significant amount of energy transferred in this interaction, it is referred to as hard collision. The secondary electron released in this process is called a δ-ray. The δ-electron is highly energetic and undergoes further Coulomb interactions with absorber atoms. The incident electron loses roughly 50% of its kinetic energy in a hard collision [24].

Interactions with the nucleus (radiation collisions)

When the impact parameter is very small ($b \ll a$), the electron interacts with the atomic nucleus through its Coulomb field. Those interactions may be elastic or inelastic and may change the electrons direction of motion. If the incident electron is scattered inelastically in the nucleus field, the electron transfers a part of its kinetic energy into the emission of X-ray photons. This type of radiation is called bremsstrahlung. Those photons contaminate the original photon beam [28]. The angular distribution of the bremsstrahlung is proportional to $\frac{\sin^2\theta}{1-\beta\cos\theta}$. θ is the angle between the electrons direction of motion and the vector from the electron to the point of observation, and β is the velocity of the electron scaled by the speed of light $\frac{v}{c}$. For small electron velocity ($\beta \to 0$), the maximum photon intensity is at $\theta = 90°$. As

the velocity approaches the speed of light the peak of the distribution moves to forward direction [25].

Stopping power

As an electron moves through an absorber medium it gradually loses its kinetic energy E_k through inelastic interactions. This is described quantitatively by the rate of energy loss per unit path length, also called the linear stopping power S_{tot}. The electron transfers its energy to the medium through collisions, or to photons trough radiation losses. Therefore, the total stopping power is the sum of the collision stopping power and the radiation stopping power.

$$S_{tot} = \frac{dE_k}{dx} = S_{col} + S_{rad} \tag{13}$$

The common unit for the stopping power is MeV/cm. Typically the stopping power is divided by the mass density of the absorber material ρ, giving the mass stopping power S_{tot}/ρ. The collision stopping power is important for radiation dosimetry as the dose D can be described by

$$D = \phi \left(\frac{S_{col}}{\rho} \right) \tag{14}$$

where ϕ is the fluence of electrons [25].

The mass stopping power can be used to calculate the electron range R in the absorber

$$R = \int_0^{E_{ki}} \left(\frac{S_{tot}}{\rho}(E) \right)^{-1} dE \tag{15}$$

where E_{ki} is the initial kinetic energy.

The mass collision stopping power defined above S_{col}/ρ is called the unrestricted mass collision stopping power. The maximum energy transferred to an orbital electron is half the energy $E_k/2$ of the kinetic energy of the electron. To determine the energy transferred to a localized region of interest, the concept of restricted mass collision stopping power is used. Here, the energy transfer to secondary δ-electrons is limited by a threshold value Δ. This excludes high energetic secondary particles from hard collisions as they carry their kinetic energy away and escape from the region of interest. The restricted mass collision stopping power L_Δ is given by

$$L_\Delta = \frac{dE_\Delta}{dx} \tag{16}$$

where dE_Δ is the energy lost by charged particles through collisions minus the total kinetic energy of the charged particles released with kinetic energies higher than Δ. A typical value for Δ is 10 keV for measurements with ionization chambers [24, 25].

2.2 Dosimetric principles and quantities

Radiation dosimetry is the quantitative determination of energy deposited in a medium resulting from exposure to directly or indirectly ionizing radiation through measurement and calculation. Due to the importance of dosimetry in the medical application of radiation, quantities and measurement procedures in dosimetry are defined by publications of international organizations like the International Commission on Radiological Units and Measurements (ICRU) [27, 29]. In this section the fundamental dosimetric quantities and units are defined.

2.2.1 Fluence

A number of particles dN is impinging on a sphere of cross-sectional area dA. The particle fluence Φ is defined as the quotient

$$\Phi = \frac{dN}{dA}. \tag{17}$$

The unit of particle fluence is m^{-2}.

The energy fluence Ψ is equivalently the quotient of the radiant energy dE and the area dA. For a monoenergetic beam with energy E the following relation between particle and energy fluence holds:

$$\Psi = \frac{dE}{dA} = \frac{dN}{dA}E = \Phi E \tag{18}$$

For polyenergetic beams an energy dependent particle fluence spectrum Φ_E and energy fluence spectrum Ψ_E can be defined:

$$\Phi_E(E) = \frac{d\Phi}{dE}(E) = \frac{1}{E}\frac{d\Psi}{dE}(E) = \frac{1}{E}\Psi_E(E) \tag{19}$$

2.2.2 KERMA

The quantity KERMA (short for **k**inetic **e**nergy **r**eleased per unit **ma**ss) is defined for indirectly ionizing radiation, so photons and neutrons. First the uncharged particles transfer their energy to the secondary charged particles trough interactions. Then the secondary particles deposit their energy in

the medium. KERMA is a non-stochastic quantity. It describes the initial transfer from energy to matter. KERMA is defined as the mean sum of the initial kinetic energy per unit mass of all secondary charged particles released through primary interactions [30]

$$K = \frac{d\bar{E}_{tr}}{dm}. \tag{20}$$

E_{tr} includes the energy of charged particles emitted after de-excitation of atoms. The unit of KERMA is J/kg. The name for this unit is gray (1 Gy = 1 J/kg). For radiation with fluence spectrum Φ_E, KERMA in a material with density ρ is given by

$$K = \Phi_E E \frac{\mu_{tr}}{\rho} dE = \Psi_E \frac{\mu_{tr}}{\rho} dE \tag{21}$$

Although KERMA does not describe where the energy of the secondary particles is absorbed, it is sometimes used as an approximation of absorbed dose.

A closely related quantity is the collision KERMA K_{col}. The collision KERMA is the kinetic energy of the charged particles released and subsequently locally dissipated as ionization. It is equal to the KERMA excluding the radiative energy loss since the photons transport their energy away from the interaction site. The collision KERMA is given by

$$K_{col} = \Psi_E \frac{\mu_{en}}{\rho} dE. \tag{22}$$

The collision KERMA is related to the KERMA by

$$K_{col} = K(1 - G). \tag{23}$$

2.2.3 TERMA

Similarly to the KERMA, the quantity TERMA (total energy released per unit mass) can be defined. It is given by the product of the energy fluence and the linear mass attenuation coefficient μ/ρ

$$T = \Psi_E \frac{\mu}{\rho} dE. \tag{24}$$

As KERMA only describes the kinetic energy released and TERMA the total energy released, it is clear that $T > K$ [1, 31].

2.2.4 Absorbed Dose

Absorbed dose is the most important quantity used in radiotherapy. In contrast to KERMA, the absorbed dose does not neglect where and how the secondary charged particles transfer their energy.

The mean energy imparted $\bar{\epsilon}$ in a given volume is

$$\bar{\epsilon} = R_{in} - R_{out} + \sum Q \tag{25}$$

where R_{in} is the mean radiant energy of all charged and uncharged particles that enter the volume, R_{out} is the mean radiant energy of all charged and uncharged particles that leave the volume, and $\sum Q$ is the mean sum of all changes of the rest energy of elementary particles that occur in the volume [30].

The absorbed dose D in a medium is then defined as the quotient of $d\bar{\epsilon}$ by the mass dm:

$$D = \frac{d\bar{\epsilon}}{dm} \tag{26}$$

The absorbed dose takes into account that the absorption of energy from electrons does not take place at the primary interaction site where the energy is transferred. The main contribution to the dose comes from the released secondary electrons. The separation energies are different for different atoms, so the absorbed dose from the same radiation field is different for every material. Therefore the absorbed dose has to be specified together with the material [28]. The dose is a non-stochastic quantity and can be used for directly and indirectly ionizing radiation. The SI unit for absorbed dose is J/kg and its unit name is gray.

2.2.5 Exposure

The exposure X describes the ability of photons to ionize air. It is given by

$$X = \frac{dQ}{dm} \tag{27}$$

where dQ is the mean total charge of ions of one sign produced when all the electrons and positrons created by photons incident on a mass dm of air are completely stopped in air [30]. The unit of exposure is C/kg.

The relation between total air KERMA and exposure is given by:

$$K_{air} = X \left(\frac{W_{air}}{e} \right) \frac{1}{1-G} \tag{28}$$

where W_{air}=33.97 eV is the average energy needed to produce an ion pair in air.

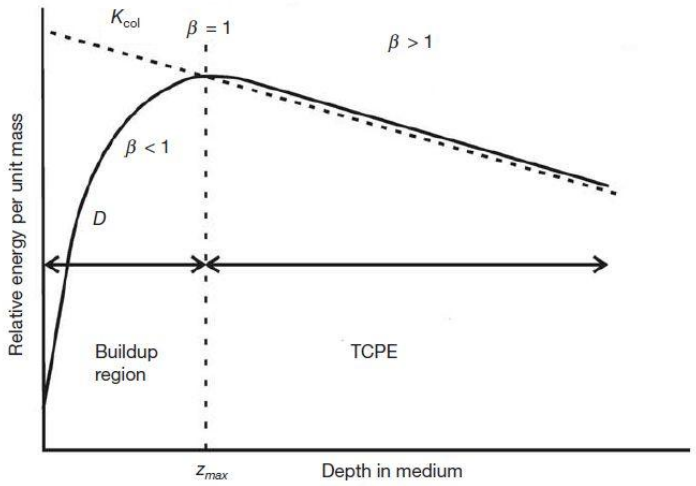

Figure 2.4: Collision KERMA and absorbed dose as a function of depth in a medium irradiated by a high energy photon beam, the dose buildup region and the region of transient charged particle equilibrium are marked (see Ref. 25, page 59)

2.2.6 Charged particle equilibrium, buildup

The transfer from photon energy to kinetic energy of charged particles does not lead to absorbed energy at that location since the secondary electrons released may transfer their energy away or produce bremsstrahlung photons. The collision KERMA is closely related to the dose. The ratio of the two quantities is given by

$$\beta = \frac{D}{K_{col}}. \tag{29}$$

The case of $\beta = 1$ is called charged particle equilibrium (CPE). The CPE occurs when the number of charged particles leaving a volume is equal to the number entering. As a high energy photon beam is entering a medium, the photon fluence gets attenuated. Therefore the collision KERMA is greatest at the surface and decreases with depth. The dose increases since the secondary electrons released travel for a finite range before depositing their energy. This effect is called dose buildup. The dose reaches a maximum at a certain depth and then decreases with the collision KERMA, see Fig. 2.4. True CPE only occurs at the dose maximum, where β is one. After the dose maximum a constant ratio of dose and collision KERMA is reached, this is called transient charged particle equilibrium [25].

The dose as a function of depth in Fig. 2.4 is called a depth dose curve.

The dose buildup at the surface is of importance in high energy photon therapy as the skin of the patient is spared from radiation damage.

2.3 Dose calculation algorithms

In modern radiotherapy a high accuracy in dose delivery is necessary to deposit the required dose to diseased tissue while minimizing dose to surrounding healthy tissue and organs at risk (OAR). In the individual treatment planning process the dose in the 3D treatment volume is evaluated with high accuracy. Dose calculation algorithms for external photon beams have been developed to calculate the dose distribution in the treatment volume [32]. In this section the concepts and physical assumptions of the different algorithms are presented, focusing on the algorithms used in this work. An extensive review of dose calculation in external photon radiotherapy was published by Ahnesjö and Aspradakis [33].

2.3.1 Correction based method

The semi empirical correction based methods are the simplest algorithms. The dose calculations are performed based on measured data in a water phantom (percentage depth doses and profiles). The measured data is modified with empirical correction factors to account for attenuation, scattering and radiological path length in the patient. It is assumed that the total dose is a sum of the primary and the scattered radiation dose [34].

$$D = D_{prim} + D_{scat} \tag{30}$$

The corrected dose distribution within inhomogeneous tissue D_{inhom} is given by:

$$D_{inhom}(x, y, z) = ICF(x, y, z) \times D_{H_2O}(x, y, z) \tag{31}$$

where $D_{H_2O}(x, y, z)$ is the reference dose distribution in a homogeneous water phantom and $ICF(x, y, z)$ is an inhomogeneity correction factor accounting for tissue heterogeneity and patient contour. There are several methods to calculate ICF, but since this algorithm was mainly used in earlier days of radiotherapy this is not discussed here in further detail.

Correction based methods usually assume electronic equilibrium and are inaccurate near heterogeneities

2.3.2 Model based methods

Model based algorithms are based on physical models of radiation interaction rather than on measured beam data. These methods employ analytical

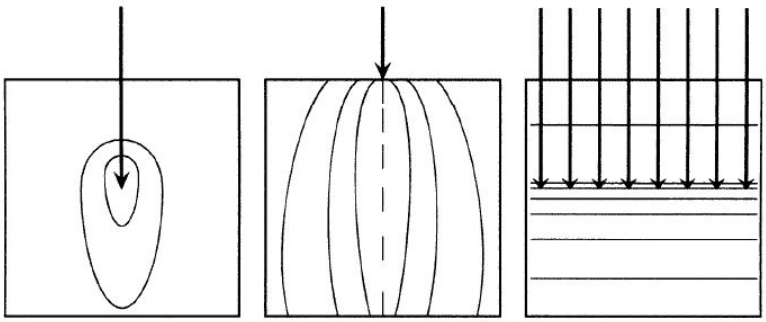

Figure 2.5: Different scatter kernel geometries: point kernels (left), pencil kernels (center) and planar kernels (right). The lines indicate isodose curves [33].

calculation of photon interaction and describe energy deposition and transport by secondary particles with pre-calculated kernels. For these algorithms the beam has to be modeled explicitly and therefore a complex radiation source model describing all components and beam forming elements has to be employed.

Convolution models

An example for this group of algorithms is the pencil beam algorithm. The absorbed dose in a point (x, y, z) is calculated by

$$D(x, y, z) = \int\int \Psi(x', y') \frac{K(x - x', y - y', z)}{\rho} dx' dy'. \tag{32}$$

$K(x, y, z)$ is a scatter kernel, which describes the absorbed dose from secondary electrons and photons around the primary interaction point. The term Ψ is proportional to the primary photon fluence on the surface of the scatter kernel. The dose is obtained by performing a convolution of the fluence with the kernel. The depth of the dose deposition is scaled by the density of the medium ρ, but the kernel is laterally invariant. The scatter kernels are usually derived by Monte Carlos simulations. The pencil beam model uses a dose deposition kernel produced from a pencil beam, but other irradiation geometries can be used as well, see fig. 2.5.

The main advantage of simple convolution models is the simplification in calculation. The Fourier transform of the dose distribution can be calculated as the product of the Fourier transforms of the fluence and the deposition kernel. For homogeneous media this method is elegant and efficient, but in heterogeneous media this simplicity is lost [32]. The scatter kernel is not

invariant to spatial shifts and has to be modified. Therefore, the convolution in Eq. 32 cannot be employed. This pencil beam model does not consider the lateral scatter in the presence of heterogeneities well as the pencil kernel is only scaled in depth.

Superposition/convolution algorithms

The simple convolution model can be modified for heterogeneous cases. This, however, removes some of the calculation advantages. The dose deposition kernels are modified in all three dimensions to correctly account for electron transport. In this case the dose calculation cannot be considered as a convolution any more, but as a superposition of distributions. This leads to the name of superposition-convolution algorithms.

The equation for dose in the superposition/convolution model is

$$D(\vec{r}) = \int T(\rho_{\vec{r}'} \cdot \vec{r}')K(\rho_{\vec{r}-\vec{r}'} \cdot (\vec{r} - \vec{r}'))d^3\vec{r}'. \tag{33}$$

Here $T(\vec{r})$ is the Terma and $K(\vec{r})$ is again the scatter kernel. The difference to the convolution in Eq. 32 is the density scaling of the kernel. $\rho_{\vec{r}-\vec{r}'} \cdot (\vec{r}-\vec{r}')$ is the radiological distance from the primary interaction site $\vec{r}'$ to the dose deposition site $\vec{r}$, it is given by

$$\rho_{\vec{r}-\vec{r}'} \cdot (\vec{r} - \vec{r}') = \int_{\vec{r}'}^{\vec{r}} \rho(\vec{x})d^3\vec{x}. \tag{34}$$

$\rho_{\vec{r}'} \cdot \vec{r}'$ is the radiological distance from the source to the primary photon interaction site. ρ is the electron density. In this model the scatter kernel is scaled in all three dimensions. As a result Eq. 33 is a superposition of distributions. The kernel gets stretched in low density materials and compressed in high density materials.

The assumption for the superposition model is that the path between the primary interaction point and the dose deposition point is the relevant path for a primary scattered photon, multiple photon scattering is neglected.

An example for a superposition/convolution type algorithm is the Anisotropic Analytical Algorithm implemented in the Eclipse treatment planning system, which is described in more detail in sec. 2.3.5. Another algorithm of this type is the Collapsed Cone Convolution Superposition algorithm (CCCS), which is used in the Pinnacle TPS (Philips, Amsterdam, Netherlands).

2.3.3 Monte Carlo methods

In contrast to the model based algorithms, which are based on analytical equations, the Monte Carlo (MC) method is a stochastic method. A huge

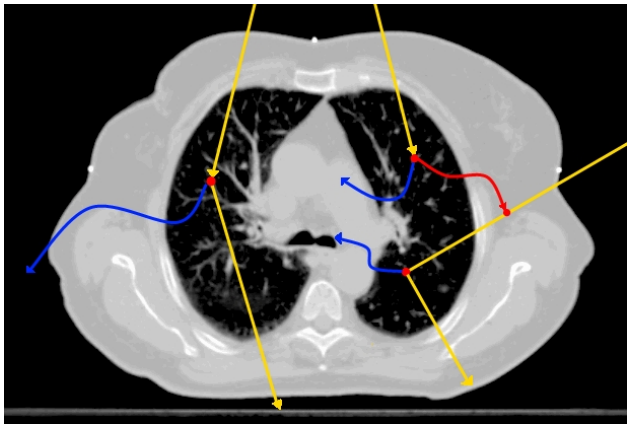

Figure 2.6: Monte Carlo dose calculation: three particle histories in the patient model. Photon (yellow), electron (blue) and positron (red) tracks are shown. The red dots represent sites of interaction.

amount of particle tracks (called histories) is simulated by pseudo-random numbers. Most particles undergo multiple interaction events until their energy is used up or they get absorbed. Figure 2.6 shows an example of two particle histories in a patient model. MC algorithms are considered the most accurate predictors for dose distributions when a sufficient number of histories is calculated and they are therefore often used as reference for the evaluation of other techniques. Unfortunately, for the calculation of dose distributions with clinical acceptable precision, the computation time may be in the order of hours.

The interaction events of the particles are sampled from probability distributions. These distributions are given by the cross sections of the individual interaction types (see sec. 2.1.1). For simulation of photon and electron transport these probability distributions have to be known.

In a simple simulation process for photon transport, it is assumed that the electrons generated by interaction events are absorbed on the spot. The photons follow an exponential attenuation. The distance s between two interactions of a photon is given by

$$s = -\lambda \ln(1 - \xi) \tag{35}$$

where λ is the mean free path for the photon energy at the beginning of the step and ξ is a random number, $0 \leq \xi \leq 1$. The type of interaction after this step is sampled from the relative probability distribution p_i, which is the ratio of the individual cross section to the total cross section. The type of

interaction $j(\zeta)$ is selected by another random number ζ such that

$$\sum_{i=1}^{j-1} p_i = P_{j-1} \leq \zeta < \sum_{i=1}^{j} p_i = P_j. \tag{36}$$

$j(\zeta)$ can be the photoelectric, Compton, Rayleigh or pair production effect [35].

The simulation of electron transport requires a different approach, since it is not possible to simulate the very large number of interactions an electron undergoes when slowing down. For this purpose so-called 'condensed history' techniques are used, where interactions are classified into groups [35].

The energy deposition into the voxels of the patient is calculated from billions of particle histories. The statistical variance per voxel decreases with increasing number of histories with $1/\sqrt{N_{hist}}$, where N_{hist} is the number of histories [36].

The pre-calculated scatter kernels used in model based algorithms are mostly obtained via MC calculations.

2.3.4 Acuros XB

A novel approach for dose calculation is the deterministic solution of the linear Boltzmann transport equation (LBTE). This new group of algorithms was developed with the motivation to calculate dose distributions with comparable accuracy to MC methods, but with shorter calculation times. A prototype software was the Attila® algorithm [5], which was originally developed for nuclear physics applications and later adopted for radiotherapy dose calculations [3, 4]. Optimization of Attila for radiotherapy applications led to the development of the Acuros algorithm [6].

Those algorithms, which solve the LBTE explicitly by discretization of fluences in space, angle and energy, are called grid-based Boltzmann solvers (GBBS) [6]. The MC algorithms and GBBS solve the same problem, the first approach giving a stochastic solution and the second approach obtaining an explicit solution. Both methods converge to the same solution of the Boltzmann equation.

The Acuros XB algorithm (AXB) for external treatment planning was released by Varian Medical Systems (Palo Alto, CA, USA) and was implemented in the Eclipse treatment planning system. The algorithm is described in detail in Varian product documentations [37, 38] and recalled here.

The algorithm

The Acuros dose calculation consists of four steps:

1. transport of source model fluence into the patient
2. calculation of scattered photon fluence in the patient
3. calculation of scattered electron fluence in the patient
4. dose calculation

Steps 1 to 3 calculate the electron fluence in every voxel of the patient. Step 1 is the only one, which is performed for every field orientation. Steps 2 to 4 are only performed once for a treatment plan. For a volumetric modulated arc therapy (VMAT) plan, one field has a large number of different orientations and step 1 has to be repeated for every angle. The next steps will be performed once, which makes the calculation time of Acuros less sensitive to the number of fields or orientations.

Steps 1 to 3 solve the time-independent system of coupled Boltzmann transport equations for electrons and photons:

$$\hat{\Omega} \cdot \vec{\nabla} \Psi^{\gamma} + \sigma_t^{\gamma} \Psi^{\gamma} = q^{\gamma\gamma} + q^{\gamma} \tag{37a}$$

$$\hat{\Omega} \cdot \vec{\nabla} \Psi^{e} + \sigma_t^{e} \Psi^{e} - \frac{\partial}{\partial E}(S_R \Psi^{e}) = q^{ee} + q^{\gamma e} + q^{e} \tag{37b}$$

Here, Ψ^{γ} and Ψ^{e} are the angular photon and electron fluences as a function of position $\vec{r} = (x, y, z)$, energy E and direction $\hat{\Omega} = (\mu, \nu, \xi)$. The terms $q^{\gamma\gamma}$, q^{ee} and $q^{\gamma e}$ are the photon-to-photon, electron-to-electron and photon-to-electron scattering sources as function of $(\vec{r}, E, \hat{\Omega})$; q^{γ} and q^{e} are the external photon and electron sources, which present sources from the machine source model. The terms $\sigma_t^{\gamma}(\vec{r}, E)$ and $\sigma_t^{e}(\vec{r}, E)$ are the macroscopic photon and electron total cross sections; $S_R(\vec{r}, E)$ is the restricted collisional plus radiative stopping power [37].

The first term of the left-hand side of Eqs. 37a and 37b is the streaming operator and the second term is the collision or removal operator. Equation 37b is the Boltzmann-Fokker-Planck equation for electrons and the third term on the left side is continuous slowing down operator, which accounts for soft collisions of electrons. The right-hand sides of both equations represent the scattering, production and source terms. An assumption for Eqs. 37 is, that photons can produce electrons, but electrons can not produce photons. Another assumption is, that two electrons are produced during pair production, instead of one electron and one positron. Those assumptions just have a minor effect on the calculated dose [37].

Step 1 q^γ and q^e are the external photon and electron contamination sources and are modeled as anisotropic point sources. q^γ includes the primary source and the extra-focal and scatter sources. The point sources are located at the target of the treatment machine.

Superposition can be used to express the angular photon fluence as a sum of uncollided and collided photon fluence components:

$$\Psi^\gamma = \Psi^\gamma_{unc} + \Psi^\gamma_{coll} \tag{38}$$

Ψ^γ_{unc} describes unscattered photons, which have not yet interacted with the patient or the phantom. Ψ^γ_{coll} refers to photons, which were produced or scattered through a photon interaction in the patient or the phantom.

Equation 38 can be substituted into the first LBTE for photons, which leads to the following equation for the uncollided photon fluence:

$$\hat{\Omega} \cdot \vec{\nabla}\Psi^\gamma_{unc} + \sigma^\gamma_t \Psi^\gamma_{unc} = q^\gamma(E, \hat{\Omega})\delta(\vec{r} - \vec{r}_p) \tag{39}$$

here the external photon source has been modeled as a point source located at position $\vec{r}_p$. This equation can be solved analytically for Ψ^γ_{unc}, which gives an expression for the uncollided angular photon fluence from a point source:

$$\Psi^\gamma_{unc}(\vec{r}, E, \hat{\Omega}) = \delta(\hat{\Omega} - \hat{\Omega}_{\vec{r},\vec{r}_p}) \frac{q^\gamma(E, \hat{\Omega}) e^{-\tau(\vec{r},\vec{r}_p)}}{4\pi|\vec{r} - \vec{r}_p|^2} \tag{40}$$

where $\hat{\Omega}_{\vec{r},\vec{r}_p} = \frac{\vec{r}-\vec{r}_p}{|\vec{r}-\vec{r}_p|}$ is the unit vector from source to destination point of the ray trace. $\tau(\vec{r}, \vec{r}_p)$ is the optical distance between $\vec{r}$ and $\vec{r}_p$.

Step 2 After solving Eq. 40, $q^{\gamma\gamma}_{unc}$ can be calculated from Ψ^γ_{unc}. Then Ψ^γ_{coll} can be solved from the following equation:

$$\hat{\Omega} \cdot \vec{\nabla}\Psi^\gamma_{coll} + \sigma^\gamma_t \Psi^\gamma_{coll} = q^{\gamma\gamma}_{coll} + q^{\gamma\gamma}_{unc} \tag{41}$$

where $q^{\gamma\gamma}_{unc}$ and $q^{\gamma\gamma}_{coll}$ represent the primary and secondary scattered photon sources.

Step 3 The next step is to calculate the electron fluence in the patient. First $q^{\gamma e}_{coll}$ needs to be evaluated. The electron fluence Ψ^e can be calculated by solving the following equation:

$$\hat{\Omega} \cdot \Psi^e + \sigma^e_t \Psi^e - \frac{\partial}{\partial E} S_R \Psi^e = q^{ee} + q^{\gamma e}_{coll} + q^{\gamma e}_{unc} + q^e \tag{42}$$

where $q^{\gamma e}_{unc}$ is the primary scattered electron source, describing electrons which are created in primary photon interactions inside the patient. $q^{\gamma e}_{coll}$ is the

secondary scattered electron source describing electrons which are created in secondary photon interactions inside the patient.

Step 4 After Eq. 42 has been solved to compute the electron fluence, the dose in every grid voxel i is calculated by:

$$D_i = \int_0^\infty dE \int_{4\pi} d\hat{\Omega} \frac{\sigma^e_{ED}(\vec{r}, E)}{\rho(\vec{r})} \Psi^e(\vec{r}, E, \hat{\Omega}) \tag{43}$$

Where σ^e_{ED} is the macroscopic electron energy deposition cross section and ρ is the material density.

Acuros XB can compute the dose in two different quantities: dose-to-water (D_W) and dose-to-medium (D_M). For the calculation of D_M, σ^e_{ED} and ρ are based on the material in grid voxel i. When D_W is calculated those two properties are based on water.

Discretization

Acuros XB discretizes the phase space variables energy, space and angle to solve the equations above.

The spatial discretization is achieved by subdividing the computational volume into spatially variable Cartesian elements. The resolution of the grid is reduced in regions with lower dose and lower gradient. A higher spatial resolution is used inside the beam. Material properties are assumed to be constant in each grid element. This technique is called adaptive mesh refinement [38].

Energy discretization is achieved through the standard multigroup method [2]. The energy derivative of the continuous slowing down operator in Eq. 37b is discretized using the linear discontinuous finite-element method [39].

For the discretization in angle the discrete ordinates method is used [2].

Acuros XB uses an energy cutoff during the photon-electron transport calculations. This cutoff is set at 1 keV for photons and 500 keV for electrons and is not adjustable by the user. When a particle passes below this energy value, it is assumed that the particle is not transported further away and all of its energy is deposited locally in that dose grid voxel.

Material specification

Prior to starting the dose calculation, the algorithm must have a material map of the patient or the phantom. In contrast to other algorithms, like AAA, Acuros XB not only considers the mass and electron density of a

Table 2: Material mass densities for biological materials in Acuros XB

Material	**Density Range [g/cm^3]**
Air	0.000 - 0.020
Lung	0.011 - 0.624
Adipose Tissue	0.554 - 1.001
Muscle, Skeletal	0.969 - 1.093
Cartilage	1.056 - 1.600
Bone	1.100 - 3.000

material, but also its chemical composition. This allows to explicitly describe the physical interaction of radiation with the absorber medium.

The Eclipse TPS determines the mass density and the material type in each voxel of the image grid. The material of a given voxel is determined by its HU (hounsfield unit) value. The HU is a quantitative scale for radiodensity and is a transform of the linear attenuation coefficient μ. The HU value can be converted directly to a mass density or electron density value with the help of the CT scanner calibration curve.

After the mass density is determined, the material assignment is done with the help of the Acuros XB material library, which includes five biological materials (lung, adipose tissue, muscle, cartilage, and bone) and 16 non-biological materials. The maximum density material is stainless steel (8.0 g/cm^3). This automatic material assignment is done for all voxels with density below 3.0 g/cm^3 (maximum density for bone) and only biological materials are automatically assigned. All voxels with a density higher than 3.0 g/cm^3 have to receive a manual assignment by the user and the user can also override the automatic material assignment. The chemical elemental composition of the materials in the material library is based on the ICRP Report 23 [40]. The five biological materials (plus air) and their density ranges in the Acuros XB material library are shown in Tab. 2.

The fundamental material data used in the dose calculation are the macroscopic atomic cross sections σ.

$$\sigma = \frac{N_a \rho}{M} \tilde{\sigma} \tag{44}$$

It is calculated from the microscopic cross section $\tilde{\sigma}$ (in barns/atom = 10^{-24} cm^2/atom) for a particular reaction and the mass density ρ (in g/cm^3). N_a is the Avogadro's number and M is the mass of the atom in atomic mass units. The macroscopic cross section σ is expressed in units of cm^{-1} and describes the probability that a certain interaction will occur per unit path length of a particle.

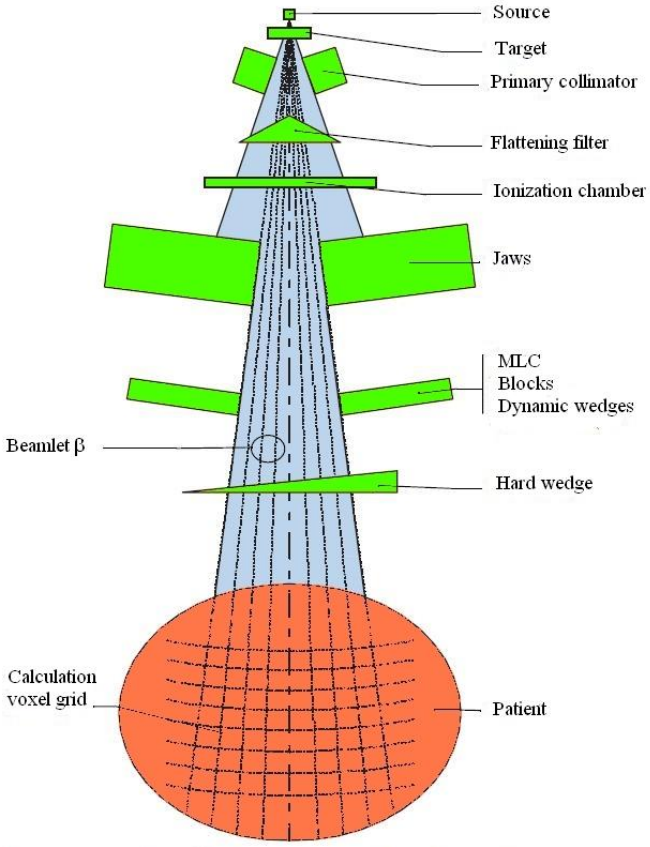

Figure 2.7: Treatment unit components modeled by the source model of Acuros XB and AAA [38]

The cross sections used by Acuros XB are generated by CEPXS [41]. CEPXS is a code for calculating coupled photon-electron cross sections. For modeling photon interactions, CEPXS uses Compton scattering, pair production and the photo-electric effect, but neglects Rayleigh scattering. The energy from bremsstrahlung photons is also not considered. These assumptions should have no significant consequence on the dose distributions generated from radiotherapy beams [38].

Source Model

The source model describes the radiation impinging on the patient or phantom before any interactions take place. Acuros XB employs the same source model as the AAA algorithm. A scheme of the modeled components of the treatment unit is depicted in fig. 2.7. The model consists of four components:

- Primary source: is a point source located at the target plane and describes the bremsstrahlung photons produced in that plane that do not have any interaction with the treatment head. The finite size of the source is modeled by the target spot size parameters in the beam configuration.
- Second source: is a Gaussian plane source located at the bottom plane of the flattening filter. It models the photons that are produced from interactions in the accelerator head outside the target, e.g. in the flattening filter, the primary collimator and the secondary jaws.
- Electron contamination: this component describes the secondary electrons produced in the beam collimators that contaminate the beam and increase the surface dose. The contamination is modeled with a depth-dependent curve that gives the amount of contamination dose at a certain depth.
- Photons scattered from wedge: describes the scattering from hard wedges. It is modeled with a dual Gaussian, where the width of the kernel increases with the distance from the wedge.

2.3.5 Anisotropic Analytical Algorithm (AAA)

The Anisotropic Analytical Algorithm is a pencil-beam kernel-based superposition dose calculation algorithm, which uses Monte Carlo derived scattering kernels. The AAA considers tissue heterogeneity in all three-dimensional directions by the use of different photon scatter kernels in all lateral directions. The dose response in every interaction site is calculated by convolution and the final dose distribution is obtained by superposition of these dose functions. The AAA was developed by Ulmer and Kaissl [42, 43] as a superposition pencil beam algorithm with a triple Gaussian photon kernel for heterogeneity correction. In 2005 the algorithm was implemented in the Eclipse TPS. The AAA algorithm is described in detail in Varian product documentations [38, 44]. The AAA is till now, the only algorithm in clinical use in the Eclipse TPS at the Department of Therapeutic Radiology and Oncology at the Medical University Graz.

Dose Calculation

The source model used by AAA is the same as for Acuros XB, see sec. 2.3.4. For the calculation of the dose distribution, the patient or phantom volume is divided into voxels. The radiation beam is subdivided into finite-sized

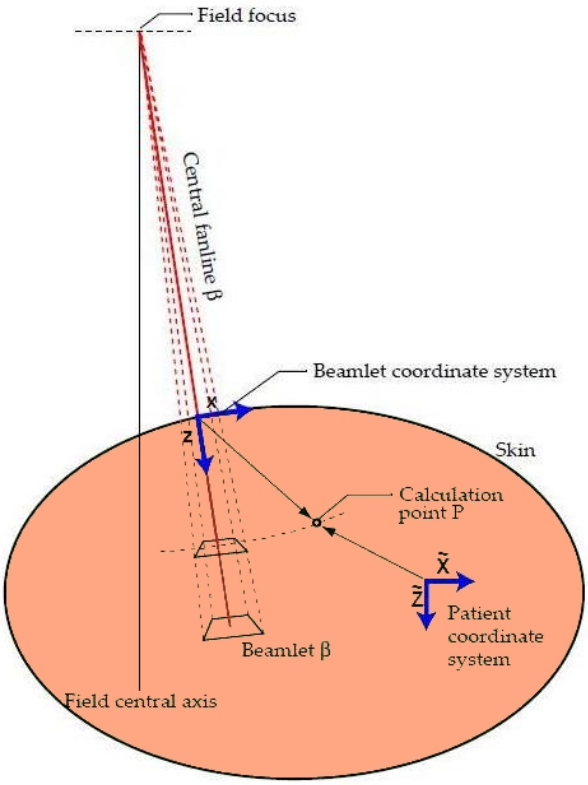

Figure 2.8: Coordinates in patient coordinate system and beamlet coordinate system for the AAA algorithm [38]

beamlets, labeled with β. In contrast to Acuros XB, which uses a Cartesian grid, the AAA uses a diverging coordinate system. The coordinate axes are aligned with the beamlines. The coordinates system is shown in fig. 2.8. In this figure and in the following equations, coordinates are labeled as $(\tilde{x}, \tilde{y}, \tilde{z})$ in the patient coordinate system and as (x, y, z) in the beamlet coordinate system.

For every calculation voxel a mean electron density is determined from the CT image and the density calibration curve. The energy deposition is calculated from convolutions of three sources: the primary photon source, the second photon source and the electron contamination. The convolutions are determined for every beamlet at every depth in the patient. This calculation can be performed analytically. The dose distribution is then obtained by summing over all source term convolutions from all beamlets.

Photon dose

The energy distribution resulting from the photons is modeled with an energy deposition density function $I_\beta(z, \rho)$ and a scatter kernel function $K_\beta(x, y, z)$. Both functions are defined for each beamlet β.

The energy distribution created by photons in point $(\tilde{x}, \tilde{y}, \tilde{z})$ by beamlet β is given by:

$$E_{ph,\beta}(\tilde{x}, \tilde{y}, \tilde{z}) = \Phi_\beta \times I_\beta(z, \rho) \times \int\int_\beta K_\beta(x' - x, y' - y, z) dx' dy' \tag{45}$$

The fluence Φ_β is assumed to be constant over the cross-sectional area of beamlet β. The energy deposition density function describes the area integral of the energy deposit over a spherical surface at depth z:

$$I_\beta(z, \rho) = \int\int h_\beta(x, y, z) dx dy \tag{46}$$

Here h_β is a polyenergetic pencil beam kernel derived from Monte Carlo simulations. The energy deposit considers tissue heterogeneity by radiological scaling:

$$I_\beta(z, \rho) = I_\beta(z') \frac{\rho(0, 0, z)}{\rho_{water}} \tag{47}$$

The distance z' is called the radiological depth:

$$z' = \int_0^z \frac{\rho(t)}{\rho_{water}} dt \tag{48}$$

ρ is the electron density.

The photon scatter function is described by a sum of six exponential functions:

$$K_\beta(x,y,z) = \sum_{k=0}^{5} c_k(z') \frac{1}{r} e^{-\mu_k r} \tag{49}$$

The exponential functions with decay constants μ_k are weighted by the factors c_k. The factors $c_k(z')$ are obtained by doing a least squares fit to the scatter kernels calculated via Monte Carlo. The constants μ_k are chosen in the range from 1 to 100 mm. This scatter kernel is only applied in the case of a homogeneous phantom. In the presence of heterogeneities the scatter kernel is scaled by the local electron density.

$$K_\beta(x,y,z) = \frac{\rho(x,y,z)}{\rho_{water}} \sum_{k=0}^{5} c_k(z') \frac{1}{r} e^{-\mu_k r_d(x,y,z)} \tag{50}$$

r_d is the radiological distance from the kernel origin (0,0,z) to the calculation point (x,y,z).

$$r_d(x,y,\rho) = \int_R \frac{\rho(\vec{t})}{\rho_{water}} |d\vec{t}| \frac{z'}{z} \tag{51}$$

The scatter kernel equations so far would result in an abrupt change in scattering conditions in depth when an interface between two materials is reached. This is compensated by using a one-dimensional scatter kernel $k_z(z)$ in depth direction.

$$k_z(z) = \frac{\rho(z)}{\rho_{water}} \sum_{i=1}^{2} c_i \frac{1}{\mu_i} e^{-\mu_i z'} \tag{52}$$

The kernel is applied in a one-dimensional convolution of energy

$$E'_{ph,\beta} = E_{ph,\beta} * k_z(z) \tag{53}$$

where $*$ is the convolution operator. This technique is called heterogeneity history correction.

Contaminating electrons

The primary photon beam is contaminated with secondary electrons produced in the collimators and air. The energy distribution from a beamlet β due to contaminating electrons is calculated as

$$E_{cont,\beta}(\tilde{x},\tilde{y},\tilde{z}) = \Psi_{cont,\beta} \times I_{cont,\beta} \tag{54}$$

where $\Psi_{cont,\beta}$ and $I_{cont,\beta}$ are the electron fluence and the energy deposit function for contaminating electrons. The electron fluence is obtained by convolving the photon fluence with a sum-of-Gaussians kernel $K_{fl,e}$:

$$K_{fl,e} = \sum_{k=0}^{1} c_k \frac{1}{2\pi\sigma_k^2} \exp\left(-\frac{x^2+y^2}{2\sigma_k^2}\right) \tag{55}$$

The parameters c_k and σ_k are optimized for Acuros XB, which employs the same source model, in sec. 4.2.

Superposition and dose conversion

The absorbed energy in an arbitrary voxel $(\tilde{x}, \tilde{y}, \tilde{z})$ in the patient is calculated as a superposition of the individual contributions from primary photons (Eq. 45), extra-focal photons (Eq. 45) and contaminating electrons (Eq. 54) from all beamlets.

$$E(\tilde{x}, \tilde{y}, \tilde{z}) = \sum_{\beta} (E_{ph1,\beta}(\tilde{x}, \tilde{y}, \tilde{z}) + E_{ph2,\beta}(\tilde{x}, \tilde{y}, \tilde{z}) + E_{cont,\beta}(\tilde{x}, \tilde{y}, \tilde{z})) \tag{56}$$

Finally the absorbed energy is converted to absorbed dose by assuming that the different materials can be modeled by electron density scaling with respect to water.

$$D(\tilde{x}, \tilde{y}, \tilde{z}) = cE(\tilde{x}, \tilde{y}, \tilde{z}) \frac{\rho_{water}}{\rho(\tilde{x}, \tilde{y}, \tilde{z})} \tag{57}$$

3 Materials and methods

This section discusses technological aspects of clinical radiation therapy. The linear particle accelerator as radiation source is described and the measurement principles of the radiation detectors are explained. The equipment and the methods used for acquiring the results are presented.

3.1 Clinical Linear Accelerator

During the history of photon radiotherapy different sources of photons were used: X-ray tubes, betatrons and ^{60}Co units. Since the introduction of the medical linear accelerator (short: linac) in the 1950s, linac therapy became the predominant treatment method over the last decades.

In a medical linac electrons are accelerated to energies from 4 MeV to 25 MeV by radiofrequency electric fields. The frequency ranges from 10^3 to 10^4 MHz with 2856 MHz being the most used frequency [24, 45]. The electrons are accelerated in straight pipe vacuum chambers, called accelerating waveguides.

A typical modern medical linacs provides electron radiation in several energies (from 4 MeV to 22 MeV) and photon radiation in two energies (e.g. 6 MeV and 18 MeV).

3.1.1 Components

A medical linac is usually mounted isocentrically to allow aiming the beam on the patient from various directions. A typical treatment machine consists of the following components:

1. Gantry
2. Gantry stand
3. Modulator with radiofrequency (RF) generator
4. Patient support assembly, treatment couch
5. Control console

Figure 3.1 shows the schematic arrangement of the components in a medical linac. The modulator contains the RF generator and the control electronics. The acceleration unit is located in the gantry. It contains the electron gun, the accelerating waveguide, the cooling system and the vacuum system for the beam-forming elements.

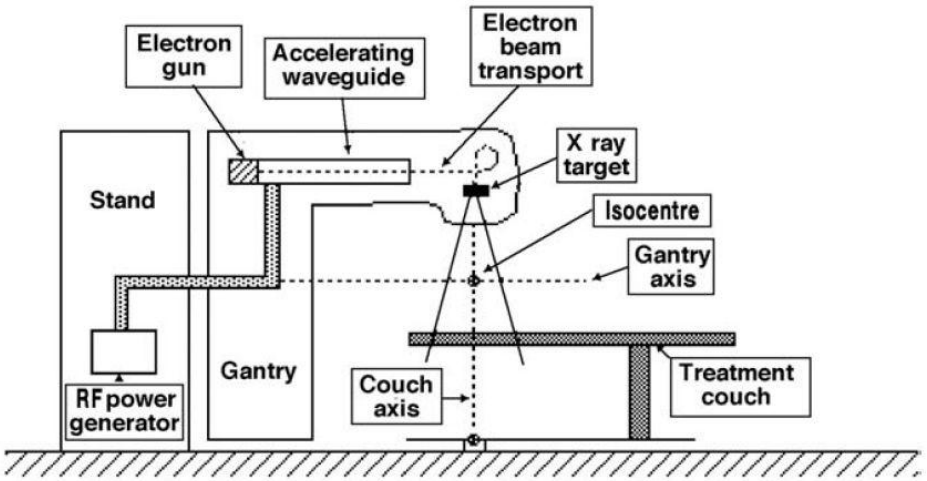

Figure 3.1: Schematic design of a isocentric medical linac: the waveguide is located in the gantry and is parallel to the isocentric axis, the radiofrequency power generator is in the gantry stand [25, p. 140]

3.1.2 Treatment head

The electron beam formed by the acceleration unit has to be further modified for clinical treatment. This is achieved with the linac treatment head where the clinical photon and electron beams are produced with several components for beam manipulation. Typical components in a linac head are:

- bending magnet
- X-ray targets
- flattening filter and electron scattering filter
- primary and secondary collimators
- ionization chambers for beam monitoring
- optional wedges
- multi leaf collimator (MLC)

Figure 3.2 shows an image of a treatment head with the waveguide of a Varian linac. The electron beams enters the treatment head in form of a pencil beam. The beam is bent via a combination of magnets by 270°. In order to create a photon beam the electron beam is directed onto a X-ray

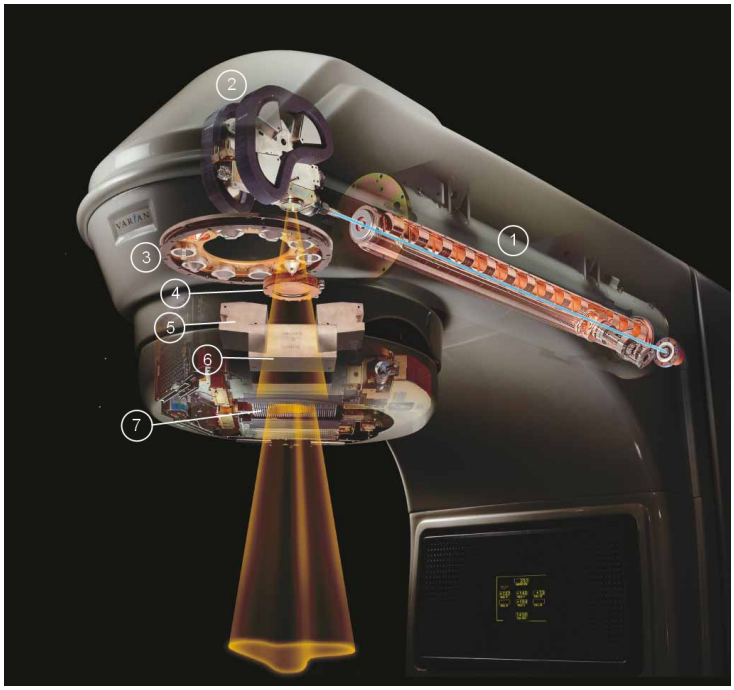

Figure 3.2: Cut through a linac treatment head with its components: 1) accelerating waveguide, 2) 270° bending magnet with X-ray target, 3) carousel with flattening filters for photons and scattering filters for electrons, 4) ionization chambers, 5) upper jaws of secondary collimator, 6) lower jaws of secondary collimator, 7) multi leaf collimator [46]

target. There a fraction of the kinetic energy of the electrons is transformed into X-rays. The bremstarget is made of a material with high atomic number (e.g. tungsten) to achieve high bremsstrahlung production efficiency. The excess energy is transformed into heat which makes cooling of the target necessary. At typical energies of a medical linac, the intensity of the X-rays is peaked in forward direction. The photon beam produced is flattened by a flattening filter to obtain a beam with a constant intensity in the profile.

The radiation beam output of the treatment machine has to be monitored constantly during a patient treatment. Therefore, a medical linac head is equipped with a beam monitoring system, consisting of dual transmission ionization chambers. The collector current in both chambers depends on the dose rate produced. The integrated current which equals to a dose of 10^{-2} Gy in a water phantom under certain conditions is defined as 1 monitor unit (MU). Additionally to measuring the dose, the monitoring system also monitors the beam energy, flatness and symmetry. If deviations in the beam parameters from the preset values occur, the monitoring circuitry terminates

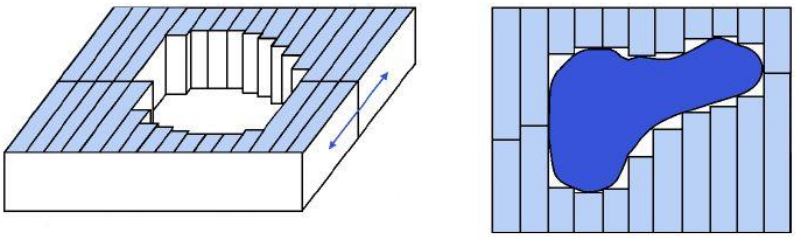

Figure 3.3: The multi leaf collimator allows the production of conformally shaped beams with individual leafs, according to Ref. 47

the radiation. The ionization chamber system must have a minimal effect on the clinical beam [25].

To control the size of a photon radiation field, collimation is achieved with a system of three collimators. The first device is the primary collimator, which defines the maximum field size with a circular shape. This fixed collimator is commonly made out of lead or tungsten [47]. The field is further shaped with the secondary collimator, a set of two upper jaws and two lower jaws. These jaws are adjustable and rotatable and can produce rectangular fields. The field can now be further modified to an irregular field shape with the multi leaf collimator (MLC). The MLC is composed of several collimator leaf pairs (up to 80 currently available) made out of tungsten with each leaf being individually computer controlled. With the MLC the radiation field can be shaped conformally to match the tumor outline with high accuracy (see Fig. 3.3). The development of the MLC opened the possibilities for new techniques in external radiotherapy like IMRT (intensity modulated radiotherapy) and VMAT (volumetric modulated arc therapy) in the last decades.

3.2 Radiation detectors

To measure dose distributions in phantoms several different dosimetry techniques were used. In this section the physical detection principles are described.

3.2.1 Ionization chamber

Gas-filled ionization chambers are the most important detectors for clinical dosimetry [48]. An ionization chamber consists of two parallel conducting

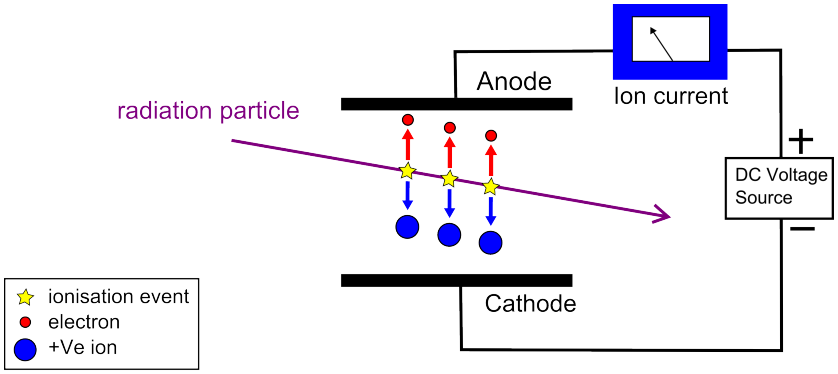

Figure 3.4: Operation principle of an ionization chamber

plates with an electrical field between them, created by application of a voltage. The medium between them is a gas, mostly air, which gets ionized by incoming radiation. The charges created (ions and electrons) are transported to the electrodes, producing an electrical current. At a high enough voltage almost no recombinations occur and the current is proportional to the dose rate. This is the saturation regime, the typical operating condition for ionization chambers. The remaining recombination losses in the saturation regime are corrected by empirical factors [48]. Figure 3.4 shows the operation principle of an ionization chamber.

In practice the ionization chamber is connected to an electrometer, which measures the integrated current and displays a dose value. The dose measured by the chamber depends on several influence quantities. The reading of the dosimeter has to be corrected with factors to obtain the absorbed dose to waterD_w [25, 49].

$$D_w = M \cdot N_{D,w} \cdot \prod_i k_i \tag{58}$$

M is the reading of the dosimeter. $N_{D,w}$ is a calibration factor of the dosimeter obtained from a standards laboratory. The factors k_i correct for influence quantities temperature, pressure, electrometer calibration, the chamber polarity effect and ion recombination.

One correction factor is the quality factor k_Q, which accounts for the use of a beam of quality different from that used in the calibration of the dosimeter. The typical reference beam for the calibration of ionization chambers is produced from a ^{60}Co gamma source. The factor $k_{p,T}$ has to be determined during every experiment, it corrects for air pressure p and air temperature T different from the reference conditions in a standards laboratory. It is defined as:

$$k_{p,T} = \frac{p_0}{p}\frac{T}{T_0} \tag{59}$$

where $p_0 = 101.3$ kPa and $T_0 = 293.15$ K.

3.2.2 Diode dosimetry

The most common solid-state detector is the semiconductor diode. Ionizing radiation may create charges in the semiconductor material by lifting a bound electron from the valence band up to the conduction band. The mobile charge carriers produced in the process (electrons and holes) get separated in the field of the intrinsic zone of the diode. If an external voltage is applied to the diode, a current can be measured. The intrinsic zone acts like an ionization chamber upon exposure to radiation [48].

The most common semiconductor materials for diode dosimeters are silicon and germanium. The energy required to produce an ion pair in air is 10 times higher than in silicon ($E_{air} = 34$ eV, $E_{Si} = 3.8$ eV) and the mass density of silicon is 2000 times higher than the density of air [48]. Therefore a diode is a highly efficient radiation detector with high energy resolution. For some dosimetry problems the use of a solid detection medium can be an advantage over a gas-filled detector [27]. The size of a solid detector can be much smaller than that of an ionization chamber due to the high density of the material. This way a higher spatial resolution can be achieved. A drawback of diode detectors is the performance degradation caused by radiation damage.

3.2.3 Radiochromic films

Radiochromic films contain short carbon-hydrogen-complexes mostly in form of dimers in ordered arrangement. After exposure to ionizing radiation those complexes polymerize to longer molecules. This effect leads to a change of the optical absorbance of the material [48]. The film changes its color directly after exposure and no further chemical processing is required. The absorbance of the material can be measured in a photographic scanner or with a densitometer and should be proportional to the dose. Radiochromic films are insensitive to visible light, thus allowing handling and preparation in room light.

A typical radiochromic film is made by laminating one or two active layers of the detector material between two polyester foils. The films can be cut to any shape needed, but the orientation of the films has to be noted. The scanning direction of the films is of importance due to the orientation of

the active molecules. A duration of at least 12 hours should pass between exposure and scanning of the film, as further chemical development processes occur in the active material during that time. Modern radiochromic films can measure doses in a wide dose range independently of dose rate and energy [50].

3.2.4 Thermoluminescence dosimeter

In certain crystalline materials, electrons are excited to metastable energy states upon exposure to ionizing radiation. The electrons may be trapped in these states for a long period of time. When energy, in form of heat, is put in to the material, the electrons can decay back into the ground states. In this process, light is emitted from the crystal. The amount of luminscence is correspondent to the absorbed dose. Materials, which exhibit this effect are called thermoluminescene detectors (TLD). Common thermoluminscence materials are lithium fluroide and calcium fluoride, which are doped with impurities (Mn, Mg, Ti, etc.) to create trapped states. After exposure to radiation a TLD is heated and the amount of light emitted is recorded. The light intensity as a function of temperature is called a glow curve. A glow curve usually has several peaks, corresponding to different trap energy levels, but not all of them are used for dose determination. The shape of the glow curve depends on the crystal, the heating rate and the radiative history of the individual TLD. The glow peaks at lower temperatures vanish when long enough time passes between exposure to radiation and heating of the crystal, this effect is called fading. Figure 3.5 shows a typical glow curve for a LiF:Mg TLD. The absorbed dose in the crystal is calculated from the area under the glow curve [25, 48].

TLDs are available in various forms, like powder or chips. Before use, TLDs need to be annealed to erase the residual signal and calibrated, since they only serve as relative dosimeters. The dose measured by TLDs is independent of dose rate and radiation quality and the materials are close to tissue-equivalent. A TLD reader consists of a heating stage and a photomultiplier for light detection. During the heating process, the photomultiplier produces a current, which is proportional to the light intensity.

3.3 Experimental equipment used

As the concepts of the medical linac and the radiation detectors has been described above, the equipment used is described in more detail here.

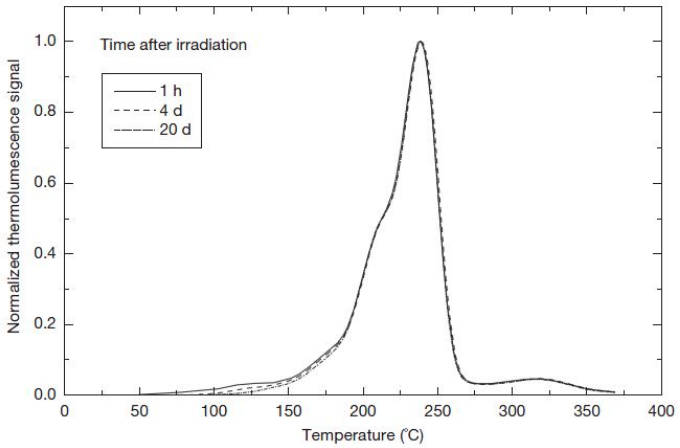

Figure 3.5: Typical glow curve for a LiF:Mg TLD. (see Ref. 25, page 88)

3.3.1 Varian linac

All experiments presented in this work, were performed with the use of four identical medical linacs of type Varian Clinac iX and one linac of type Varian Novalis Tx. The two types are almost identical, except for the mounted MLC.

The Clinac iX can be operated with two photon energies (6 and 18 MeV) and six electron energies (4/6/9/12/16/20 MeV). It is equipped with a MLC of type Varian Millenium 120 consisting of 60 leaf pairs. The maximum field size is 40x40 cm^2. The leafs have a width of 5 mm in the central 20 cm of the field and a width of 10 mm in the outer 20 cm of the field [51].

3.3.2 ArcCHECK Phantom

The ArcCHECK Phantom (Sun Nuclear Corp., Melbourne, FL, USA) is a cylindrical phantom made out of water-equivalent material and equipped with an array of 1386 silicon diode detectors. The diodes are arranged in form of a spiral around the cylinder axis, with 10 mm spacing between the diodes. The diode dimensions are 0.8x0.8x0.03 mm^3. The diameter of the spiral is 21 cm. The cylindrical shape assures that the resolution and precision is constant for every gantry angle. The ArcCHECK phantom is intended for verification of rotational radiation treatments. The phantom is used with the SNC Patient software (Sun Nuclear) that records the dose distribution in the diode array and compares it to the treatment plan dose calculated by a treatment planning system.

The phantom's central cavity has a diameter of 15 cm and can be filled with various accessories. In this work a modular insert, the MultiPlug, was

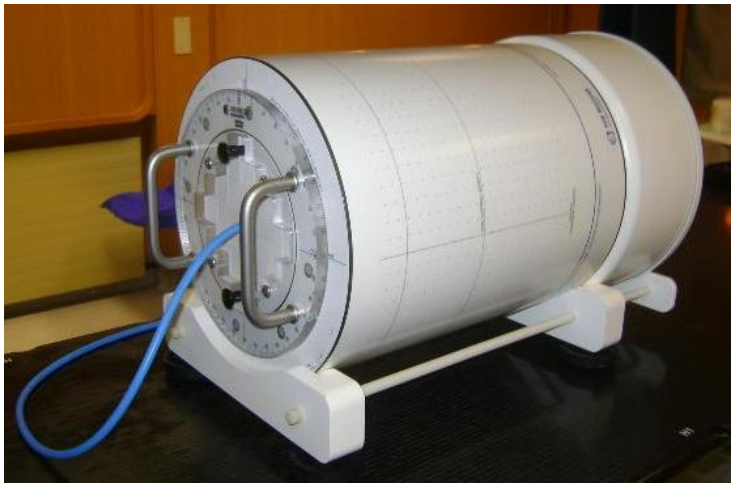

Figure 3.6: ArcCHECK Phantom with ionization chamber and homogeneous insert. The positions of the diodes are marked by dots

used. It allows for positioning of additional radiation detectors and heterogeneity inserts in the cavity of the phantom. In the standard setup, the MultiPlug is a homogeneous cylinder made of water-equivalent RW3 material with a hole in the central axis for measurements with an ionization chamber (see Fig. 3.6). The individual modular parts of the MultiPlug can be removed and replaced with inserts of different density and material composition. The heterogeneity inserts have a rod-like shape (dimensions: 2x2x22 cm^3) and are equivalent to four biological tissues: bone, lung, muscle, adipose tissue. The inserts in the central horizontal plane of the plug can be replaced by a cassette for radiochromic films. Figure 3.7 shows the front end of the MultiPlug insert equipped with heterogeneity inserts and the cassette.

3.3.3 Seven29 chamber array

The 2D-ARRAY seven29 (PTW Freiburg, Freiburg, Germany) is an ion chamber array with 729 (27x27) chambers arranged in a 2D matrix with 1 cm spacing between them (see Fig. 3.8). The chambers have a cubic shape with dimensions 5x5x5 mm^3. The chambers are vented to air. The material of the array is acrylic (PMMA). A maximum field size of 27x27 cm^2 can be measured. By shifting the array three times by 5 mm during an experiment, the number of measuring points can be increased to 2916 and the lateral resolution can be improved to 5 mm. The dose range of the chambers is 200 mGy to 1000 Gy. The array is connected to a computer via an interface and the software MatrixScan (PTW) is used for acquiring measurements [52].

Before every measurement, the ambient pressure and temperature are

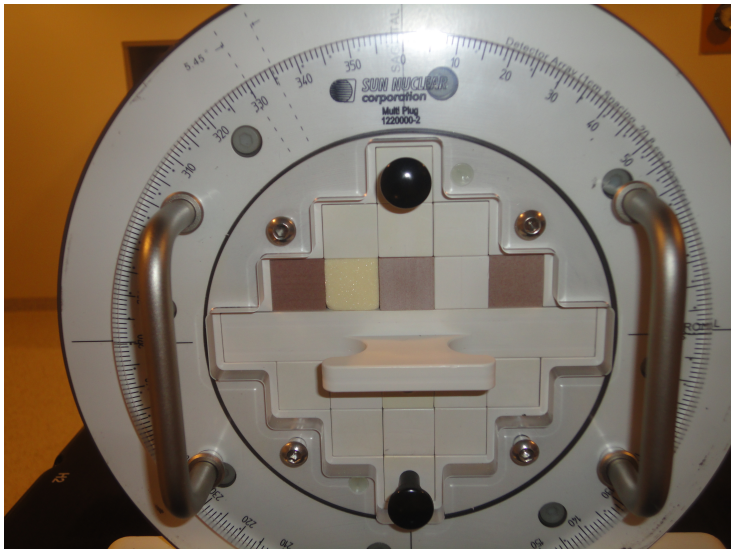

Figure 3.7: MultiPlug insert in the ArcCHECK phantom with heterogeneity inserts and film cassette

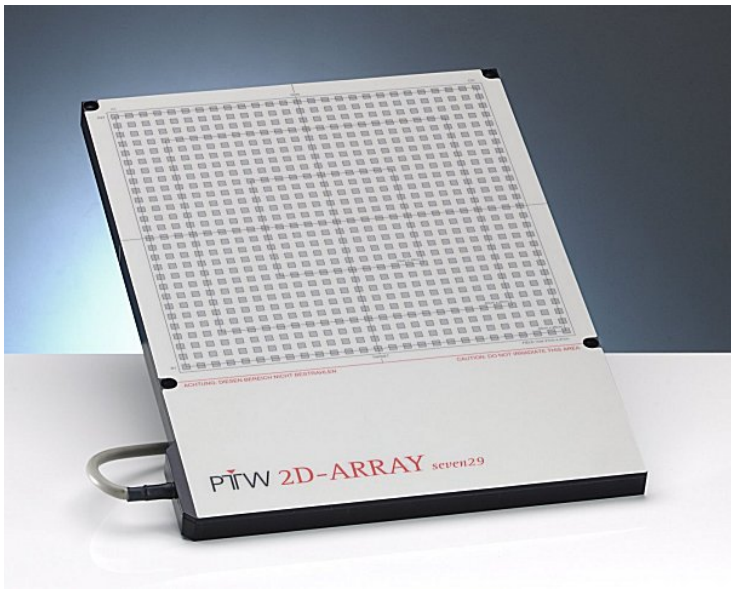

Figure 3.8: 2D-array seven29, the positions of the ionization chambers are marked [52]

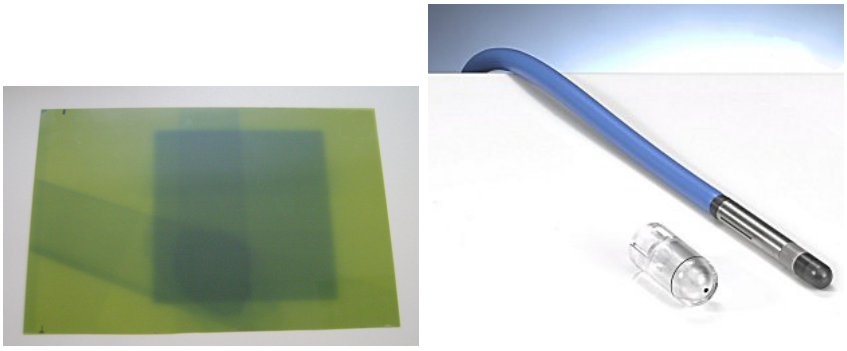

(a) EBT3 radiochromic film (b) 31010 Semiflex ionization chamber [54]

Figure 3.9: Gafchromic EBT3 film and PTW M31010 Semiflex ionization chamber

determined to obtain the correction factor $k_{p,T}$. An additional correction factor k_{user} can be used for cross calibration. It is determined by comparing the dose value of the central chamber in the array with the dose measured by a separate ionization chamber.

3.3.4 Gafchromic EBT3 film

For radiochromic film dosimetry the Gafchromic EBT3 film (International Specialty Products, Wayne, NJ, USA) was used in this work (see Fig. 3.9(a)). The film is made of a 30 micron thick active substrate layer between two polyester foils (125 microns each). The density of the material is near tissue-equivalent. The EBT3 can be used in the dose range from 1 cGy to 40 Gy [53]. The films were usually scanned on the next day after exposure to radiation, but never earlier.

For scanning of the EBT3 the Epson Perfector V700 PHOTO flat bed scanner (Seiko Epson Corp., Suwo, Japan) was used. The maximum resolution is 6400 dpi. The films were scanned in 48 Bit. The conversion of the image into a dose image was achieved with a Matlab program that uses three color channels (red, blue, green) for dose conversion.

3.3.5 31010 Semiflex ionization chamber

For point dose measurements a 31010 Semiflex ionization chamber (PTW Freiburg) was used (see Fig. 3.9(b)). The chamber is vented to air and is waterproof. The ionization volume is 0.125 cm^3. The chamber has a spherical shape to achieve a flat angular response.

Figure 3.10: Different inhomogeneous and homogeneous slabs to arrange into the slab phantom

3.3.6 Slab Phantom

For measurements of dose distributions in heterogeneous media a slab phantom was built in the workshop of the department. The phantom is made of slabs of different materials with dimensions 20x20 cm^2 and varying thicknesses from 1 mm to 2 cm. The slabs can be arranged vertically in any order. The materials used in this phantom were: PMMA, cork (lung-equivalent), bone-equivalent plastic, water-equivalent plastic and air cavities. Solid homogeneous slabs and inhomogeneous slabs were used. Figure 3.10 shows the used slabs of the phantom. To provide exact positioning of the slabs, a stand made of PMMA was used to hold the phantom (see Fig. 3.11). For dose calculation in the treatment planning system, each slab arrangement had to be scanned on a CT and the scan was imported into Eclipse.

The slab phantom was used with two different dosimetry techniques. To perform radiochromic film dosimetry, Gafchromic EBT3 films were cut to dimensions 20x20 cm^2 and were put between the slabs at different positions. Measurements with an ionization chamber were performed in a PMMA slab that has a cavity to accommodate a chamber in the vertical central axis of the phantom, it is shown in Fig. 3.10 on the right bottom.

3.3.7 ATOM Phantom

The ATOM phantom (CIRS Inc., Norfolk, VA, USA) is an anthropomorphous dosimetry phantom, depicted in Fig. 3.12. In this study the adult

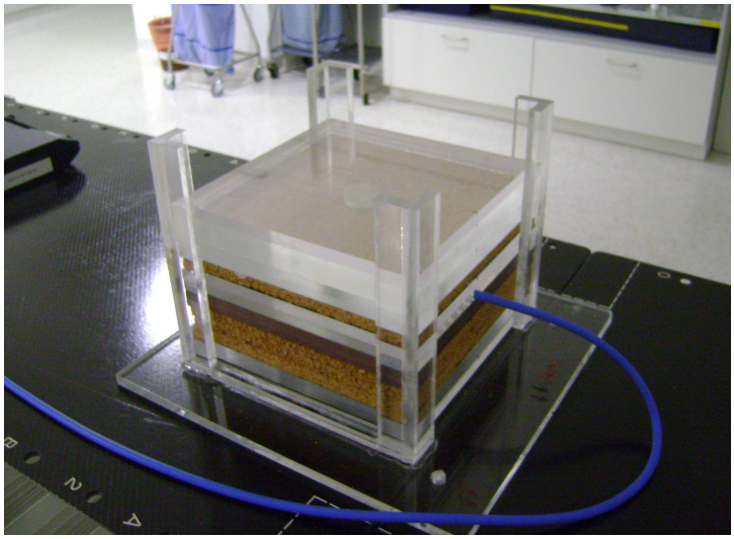

Figure 3.11: Slab phantom with the PMMA stand and ionization chamber

male phantom model 701 (height: 173 cm, weight: 73 kg) was used. The phantom is composed of 39 sectional slabs of 25 mm thickness. The sections are held together by a reinforcement top and base and threads. For all measurements in this work, the top slab (section 01) of the phantom was removed.

The phantom is made out of tissue-equivalent material, imitating the the human anatomy. The tissues simulated in the phantom are soft tissue, bone tissue, cartilage, spinal cord, spinal disks, lung, brain and sinus [55]. Figure 3.13 shows two sections of the phantom, one in the head and neck region and one in the lung region. The different types of tissues are clearly visible.

For dose verification with thermoluminescence dosimeters, the phantom features a 3 cm x 3 cm hole grid. The thru holes have a diameter of 5 mm and are filled with removable solid plugs of corresponding tissue. The TLD chips can be placed in these holes.

3.4 Treatment planning system

All dose calculations in this work were performed with the treatment planning system Eclipse (Varian Medical Systems) in version 11.0.31. The dose calculation algorithms AAA and Acuros XB (both in version 11.0.31) are implemented in this TPS. Eclipse offers many different contouring and modern planning techniques, such as IMRT and VMAT. A screenshot illustrating the user interface for external treatment planning is shown in Fig. 3.14.

The calculation grid size for the dose calculation can be set manually in

Figure 3.12: ATOM phantom

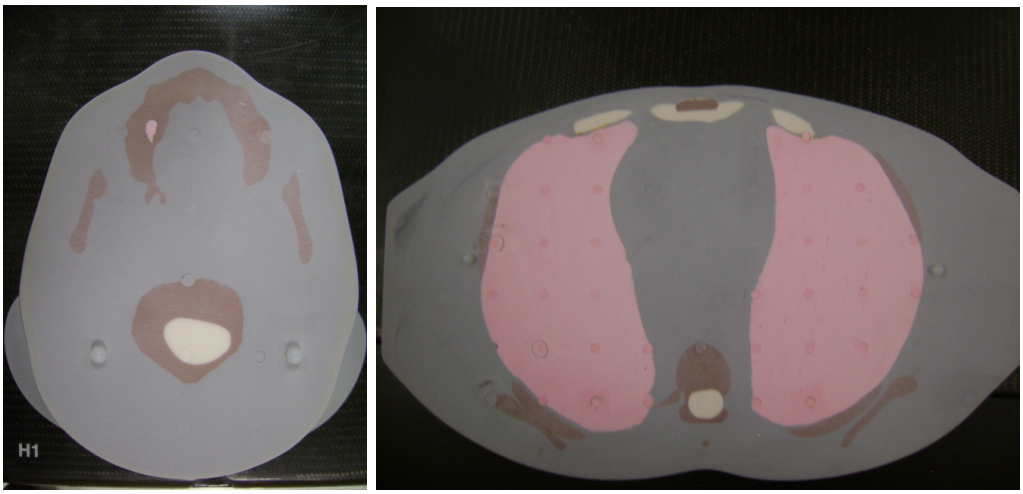

(a) head and neck (b) lung

Figure 3.13: Cross sections through the ATOM phantom in the head and neck region and the lung region

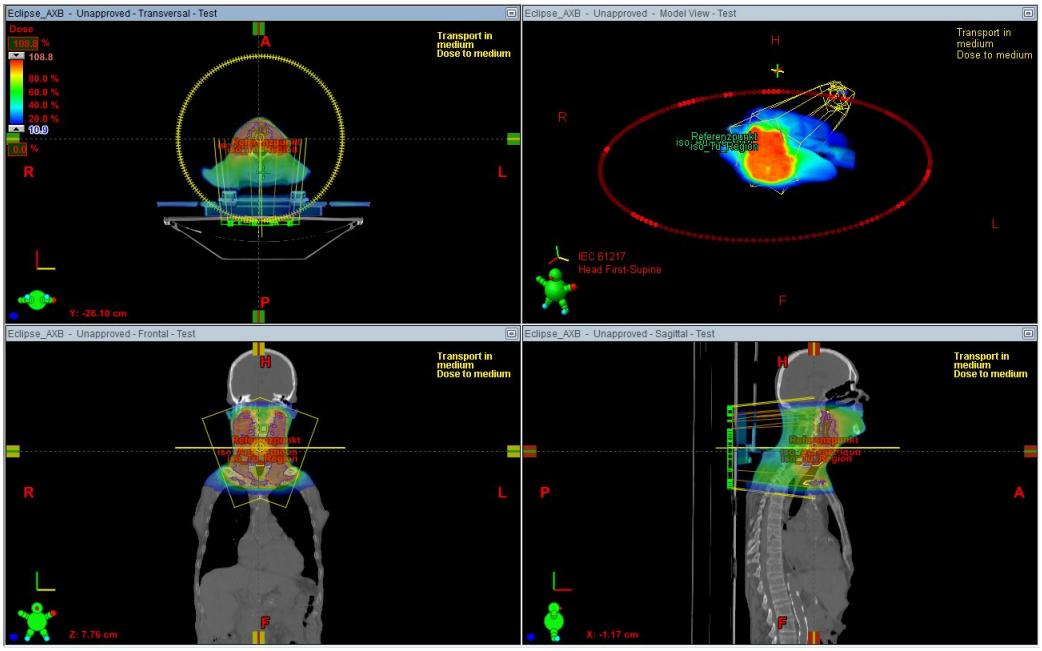

Figure 3.14: Treatment planning system Eclipse of Varian Medical Systems

the TPS in the range of 1 mm to 3 mm for AXB and 1 mm to 5 mm for AAA. In this work the default grid size of 2.5 mm was used for all dose calculations.

3.5 Gamma index evaluation

For comparing dose distributions calculated in the TPS to measured dose distributions, a technique named Gamma index evaluation is used. The technique was developed by Low et. al. [56]. It is a widely used quantitative tool to evaluate dose calculations and treatment plans. The measurement is used as a reference and a dose difference criterion ΔD_M and a distance-to-agreement (DTA) criterion Δd_M are set. The DTA is the distance between a measured data point and the nearest point in the calculated dose distribution that has the same dose.

The gamma index method considers the dose difference and the DTA in its acceptance criterion, which is described by the surface of an ellipsoid

$$1 = \sqrt{\frac{r^2(\vec{r}_m, \vec{r}_c)}{\Delta d_M^2} + \frac{\delta^2(\vec{r}_m, \vec{r}_c)}{\Delta D_M^2}}, \tag{60}$$

where $r(\vec{r}_m, \vec{r}_c) = |\vec{r}_c - \vec{r}_m|$ is the distance between the measured and the

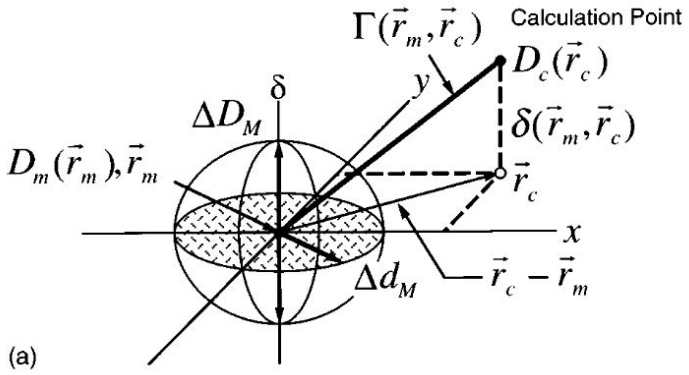

Figure 3.15: Two dimensional representation of dose distribution evaluation criteria using the dose-difference and the distance-to-agreement [56].

calculated dose point and $\delta(\vec{r}_m, \vec{r}_c) = D_c(\vec{r}_c) - D_m(\vec{r}_m)$ is dose difference between the two points. If any dose point of the calculation $D_c(\vec{r}_c)$ lies inside surface of the ellipsoid given by Eq. 60, the calculation passes at $\vec{r}_m$. A geometric representation of the criterion can be seen in Fig. 3.15.

To compare the calculation over the plane $\vec{r}_c - \vec{r}_m$ to the measurement point $\vec{r}_m$ a quality index γ is defined:

$$\gamma(\vec{r}_m) = min\{\Gamma(\vec{r}_m, \vec{r}_c)\}\,\forall \vec{r}_c \tag{61}$$

$$\Gamma(\vec{r}_m, \vec{r}_c) = \sqrt{\frac{r^2(\vec{r}_m, \vec{r}_c)}{\Delta d_M^2} + \frac{\delta^2(\vec{r}_m, \vec{r}_c)}{\Delta D_M^2}} \tag{62}$$

The pass-fail criteria are $\gamma(\vec{r}_m) \leq 1$ for passing and $\gamma(\vec{r}_m) > 1$ for failing the evaluation at measurement point $\vec{r}_m$. As an overall evaluation of a calculated treatment plan, the percentage of measurement points that pass the γ-criterion is given. This number is the Gamma-agreement index (GAI) and has to stay above a certain threshold (e.g. 90%) for a treatment plan to pass the evaluation.

The dose difference criterion ΔD_M is given as a relative difference, where one has to distinguish between a local or global dose criterion. For a global criterion, ΔD_M is constant for all measurement points $\vec{r}_m$ and usually expressed relative to the measured maximum dose (e.g. 3% of D_{max}). For a local dose criterion, ΔD_M is defined relative to the local dose $D_m(\vec{r}_m)$ at point $\vec{r}_m$ (e.g. 3% of $D_m(\vec{r}_m)$), resulting in a smaller acceptable absolute dose difference in low dose regions. Usually dose values below a certain threshold are suppressed and do not contribute to the Gamma evaluation. Typical DTA and dose difference criteria are 3 mm/3% or 2 mm/2%.

In this work the Gamma index evaluation (or Gamma analysis) was used to compare measured and calculated 2D dose distributions. The GAI was used as quantity to compare the agreement of different dose calculations to a measurement. The dose difference criterion was always used as a global criterion relative to the maximum measured dose.

4 Implementation and configuration of the Acuros XB algorithm

In order to use the Acuros XB algorithm in treatment planning in Eclipse, the algorithm has to be implemented and configured in the TPS.

An accurate and precise dose calculation in the treatment planning process can be seen as solving two separate tasks: the modeling of the radiation output of the accelerator (source modeling) and from that the dose calculation in the patient [57]. Errors in the source modeling directly lead to errors in the dose calculation in the patient. So, the first step before using the Acuros algorithm, is to adjust the source model to the treatment machine. The source model (described in sec. 2.3.4) is defined by a set of physical parameters. Values for the parameters are derived by an optimization process. The input for this process are simple dose measurements in a water phantom on the treatment unit. Most of the configuration of the source is done automatically, but some parameters should still be manually adjusted for optimal agreement with the measurements.

4.1 Effective target spot size

The effective target spot size is a parameter in the beam configuration, that models the finite size of the bremsstrahlung target, which is the primary source in the source model (see sec. 2.3.4). There are two independent parameters for the X- and the Y-direction of the spot size. The modeling is achieved by applying a Gaussian smoothing function to the energy fluence of primary photons. The two parameters equal the widths of the Gaussian in the X- and Y-direction at the isocenter plane. The parameters can have a significant effect on the calculated absolute dose level for very small fields and on the shape of the penumbra [38]. The spot size parameters are not automatically optimized.

The Eclipse Algortihms Reference Guide [38] suggests a value of 1 mm for X- and Y-direction for Acuros XB in combination with Varian treatment units, but recommends fine-tuning of the parameter by comparing measurements and calculations.

For this purpose dose profiles and depth dose curves from a 6 MeV photon beam in a water phantom were calculated with several different values for the target spot size and compared to measurements. Measurement data in a water phantom at the treatment machine was available for several different field sizes (3x3/ 4x4/ 6x6/ 10x10/ 20x20/ 40x40 cm^2). The data included relative depth dose curves at the central field axis and relative dose profiles

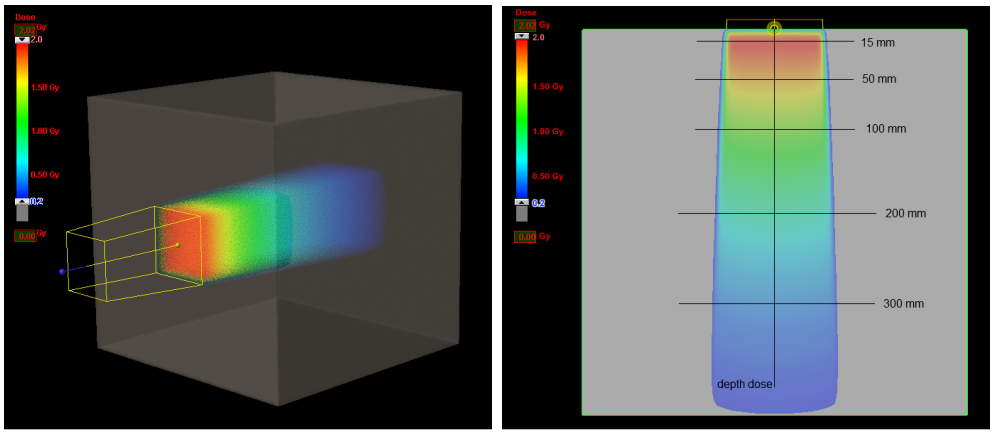

(a) 3D view

(b) 2D view, evaluated profiles and depth dose curves are indicated by lines

Figure 4.1: A 40x40x40 cm^3 water phantom as contoured in Eclipse. A 10x10 cm^2 field with 200 MU and the dose distribution in the phantom are shown.

at several depths (15/ 50/ 100/ 200/ 300 mm). The data had been measured with the Semiflex 31010 ion chamber (field sizes:20x20 - 40x40 cm^2) and a silicon diode detector (field sizes:3x3 - 10x10 cm^2. Diode P from PTW).

As the measurement data was only available in form of relative dose curves, absolute dose measurements had to be conducted in the water phantom to normalize the curves. The phantom was placed at a source-surface distance of 100 cm. The Semiflex 31010 ionization chamber was mounted on a computer controlled chamber holder and absolute dose measurements were performed for all field sizes mentioned above in the central field axis. 200 MU were used for all field sizes. Dose values were acquired at depths 15, 50, 100, 200, and 300 mm.The relative depth dose curves were then normalized to the absolute dose at d=15 mm and the relative dose profiles were normalized to the dose in the central axis at the corresponding depth.

In Eclipse a 40x40x40 cm^3 water phantom was contoured and a Hounsfield unit (HU) of -8 was assigned (see Fig. 4.1). The same dose curves as from the measurement data were calculated and exported. This was repeated with different values for the target spot size parameter. Only the dose profiles for the 40x40 cm^2 field were left out as they are limited by the dimensions of the phantom. The used values for the effective target spot sizes (X- and Y-direction) were: 0.5x0.5 mm^2, 1x1 mm^2, 1.5x1.5 mm^2 and 2x2 mm^2.

Figure 4.2 shows the depth dose curve for a 4x4 cm^2 field in the water phantom as measured and calculated with Acuros XB with the four different

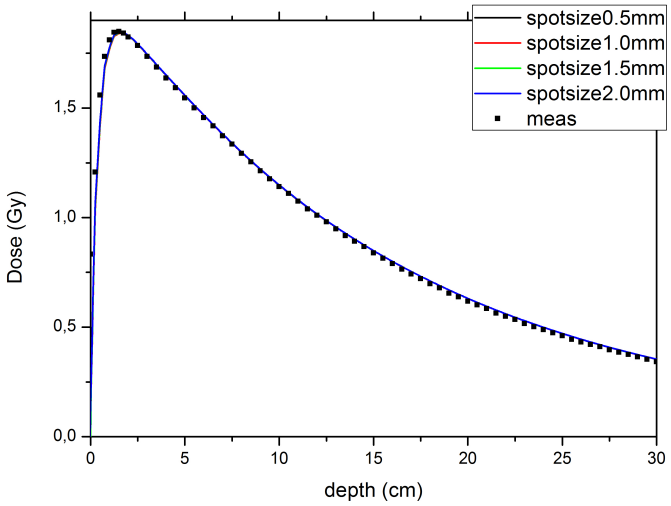

Figure 4.2: Measured and calculated depth dose curve in the water phantom for a 4x4 cm^2 field, 200 MU. Calculation with four different values for the target spot size (in mm) in the AXB source model

spot sizes. All four calculations show good agreement with the measurement and no calculation outperforms the others significantly. This statement holds for all field sizes investigated.

Figure 4.3(a) shows the dose profile for a 3x3 cm^2 field at depth 50 mm in the water phantom as measured and calculated with Acuros XB with the four different spot sizes. Only the part of the penumbra is displayed to emphasize the differences between the calculations. The calculation with spotsize 0.5 mm (short for 0.5x0.5 mm^2) shows the best agreement in the outer part of the penumbra, but performs worst at the inner part of the penumbra. The calculations with spot sizes 1 mm and 1.5 mm have the best overall agreement with the measurement. Figure 4.3(b) shows the dose profile for a 20x20 cm^2 field at depth 100 mm. Spotsize 0.5 mm shows the largest deviations to the measurement. Spotsizes 1.0 mm, 1.5 mm and 2.0 mm all are in good agreement with the measured profile. In overall it is obvious that calculations with spotsizes 1.0 mm and 1.5 mm perform best when small fields and large fields are considered.

To give a more quantitative expression of this, a 1D Gamma analysis for the dose profiles and depth dose curves was performed for the calculations with spotsizes 1.0 mm and 1.5 mm. The gamma criterion was set to 1 mm/1%.

Figure 4.4 shows the measured dose profile for field size 3x3 cm^2 at depth

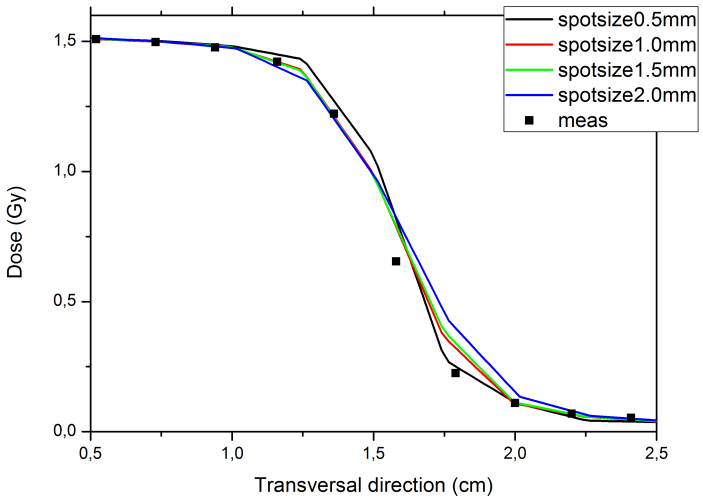

(a) 3x3 cm^2, depth 50 mm

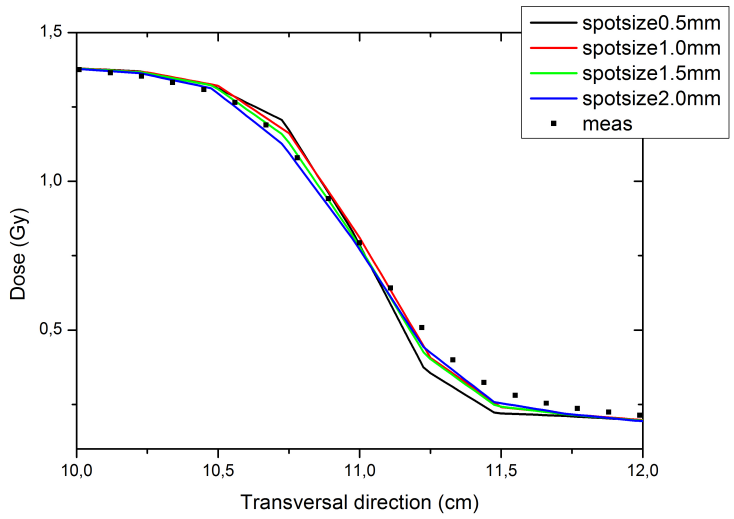

(b) 20x20 cm^2, depth 100 mm

Figure 4.3: Measured and calculated dose profiles in the water phantom. Calculation with four different values for the target spot size (in mm) in the AXB source model

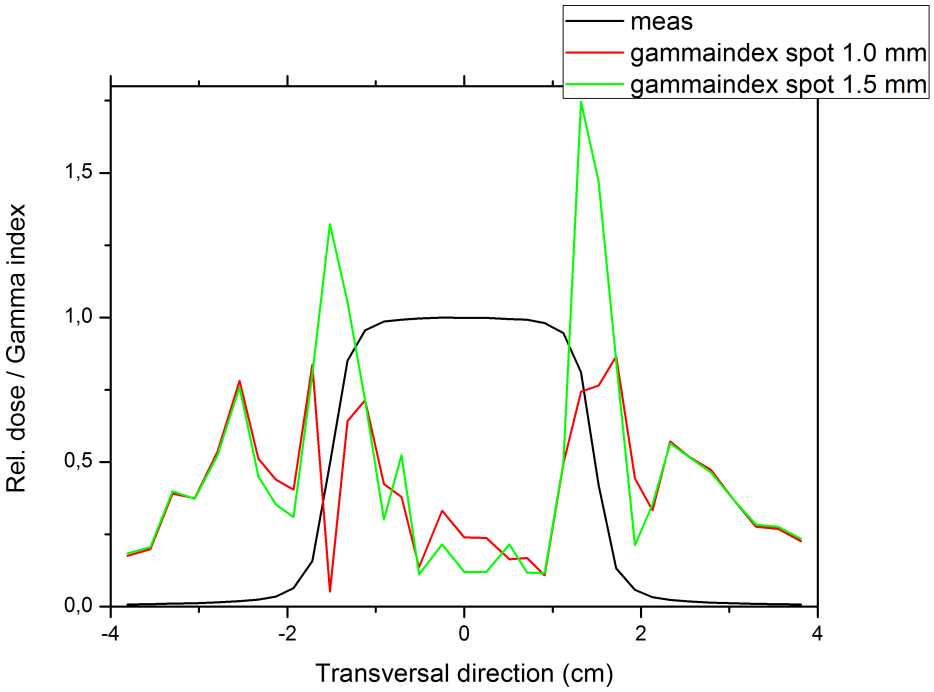

Figure 4.4: 1D Gamma evaluation for two AXB calculations with spot-sizes 1 mm and 1.5 mm, dose profile at depth 15 mm in the water phantom for the 3x3 cm^2 field, gamma criterion: 1 mm/ 1%

15 mm and the one-dimensional distribution of gamma values for the AXB calculations with spot sizes 1 mm and 1.5 mm. The highest gamma values appear at the penumbra. The 1.5 mm spot size calculation exhibits a few gamma indices failing the criterion, whereas in the 1 mm calculation the gamma index is below 1 for all evaluation points.

Figure 4.5 shows the measured depth dose curve for field size 4x4 cm^2 and the one-dimensional distribution of gamma values for the AXB calculations with spot sizes 1 mm and 1.5 mm. High gamma values appear in the buildup region of the curve, but after the dose maximum all points pass the gamma test. Both spot sizes exhibit a very similar gamma index distribution.

The Gamma-agreement index (GAI) was calculated for all depth dose curves and profiles measured in the water phantom. Table 3 shows the average GAIs for all dose profiles and all field sizes calculated in AXB with spot sizes 1 mm and 1.5 mm. Additionally the GAIs for the AAA calculation are presented for comparison. Every GAI value presented in this table is obtained by calculating the average GAI value from the five individual GAI values at every depth (15 mm/ 50 mm/ 100 mm/ 200 mm/ 300 mm). For

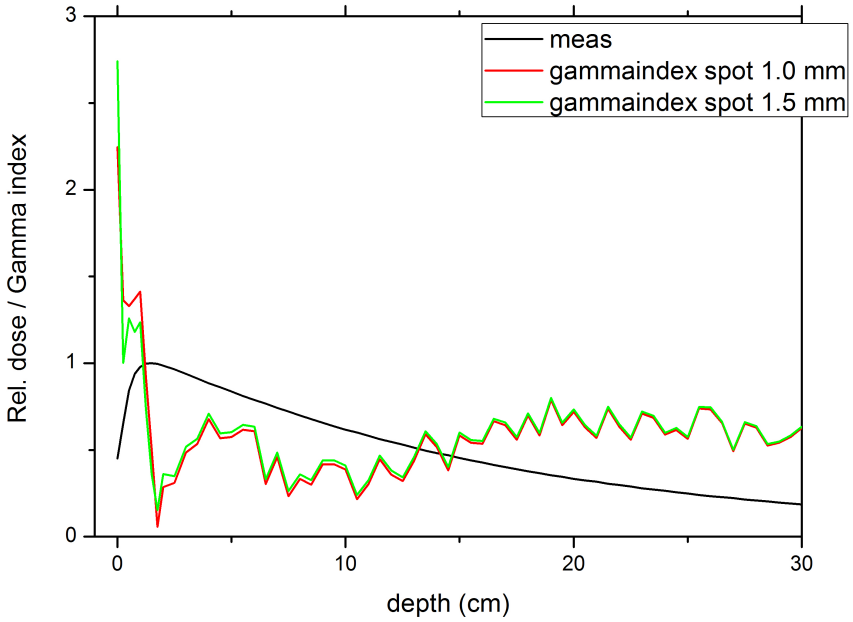

Figure 4.5: 1D Gamma evaluation for two AXB calculations with spot-sizes 1 mm and 1.5 mm, depth dose curve in the water phantom for the 4x4 cm^2 field, gamma criterion: 1 mm/ 1%

Table 3: Average Gamma agreement indexes (criterion: 1 mm/1%) for AXB with spot sizes 1 mm and 1.5 mm and AAA for dose profiles in the water phantom at several depths

Field size (cm^2)	**AXB 1 mm**	**AXB 1.5 mm**	**AAA**
3x3	87.72 %	86.34 %	83.44 %
4x4	88.43 %	86.56 %	83.69 %
6x6	85.69 %	86.88 %	86.85 %
10x10	76.63 %	77.37 %	96.98 %
20x20	75.52 %	76.24 %	68.48 %

Table 4: Gamma agreement indexes (criterion: 1 mm/1%) for AXB with spot sizes 1 mm and 1.5 mm and AAA for dose depth curves in the water phantom

Field size (cm^2)	**AXB 1 mm**	**AXB 1.5 mm**	**AAA**
3x3	81.36%	71.19%	100%
4x4	100%	100%	100%
6x6	100%	100%	100%
10x10	94.92%	100%	100%
20x20	100%	100%	100%
40x40	93.33%	93.33%	95.38%

small fields (3x3 and 4x4 cm^2) AXB 1 mm has the highest GAIs, but it is surpassed by AXB 1.5 mm and AAA at larger field sizes.

Table 4 shows the GAIs calculated from the depth dose curves. Only the gamma indices behind the dose maximum were evaluated since larger deviations occur in the buildup region. For the 3x3 cm field the AXB 1 mm calculation shows better agreement (81.36%) to the measured curve than the 1.5 mm calculation (71.19%). For larger field sizes both show similar performance with almost 100% agreement. In comparison, AAA shows almost perfect agreement for all field sizes.

As a result of this investigations it can be stated that the optimal value for the target spot size parameter in the AXB source model is 1x1 mm^2. The 1 mm calculations show better overall agreement than the 1.5 mm calculation, especially for small field sizes. Advanced radiotherapy techniques like IMRT and VMAT use small field sizes, therefore a value of 1x1 mm^2 for the spot size is favorable and all AXB calculations were conducted with this value for the parameter.

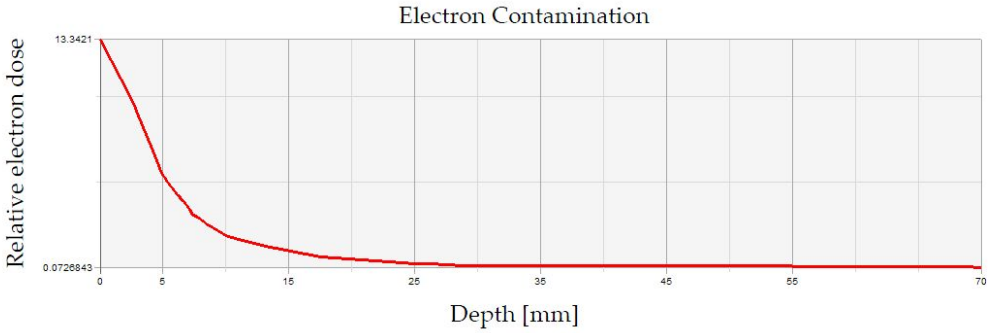

Figure 4.6: Example of an electron contamination curve [38]

4.2 Electron contamination

The electron contamination describes the contamination dose caused by secondary electrons, which are produced from scattering in the treatment machine and air. It is modeled with a depth-dependent curve that describes the laterally integrated electron dose as a function of depth. The curve falls rapidly away from the surface. Figure 4.6 shows an example of an electron contamination curve.

In addition two smoothing parameters σ_0 and σ_1 are used for describing the electron contamination. The shape of the electron fluence is calculated as a convolution of the aperture shape and a 2D sum-of-Gaussians kernel, which is defined by parameters σ_0 and σ_1. Another coefficient c_0 specifies the relative weight of the first Gaussian (σ_0), which is between 0 and 1.

The three parameters σ_0, σ_1 and c_0 are subject to optimization. The optimization process of the beam configuration determined optimal parameter values with

$$\begin{aligned} \sigma_0 &= 35.3274 \text{ mm} \\ \sigma_1 &= 410.666 \text{ mm} \\ c_0 &= 0.0583. \end{aligned} \tag{63}$$

The TPS automatically computes gamma error histograms and average gamma error values for a beam configuration from depth doses and dose profiles for several field sizes in a water phantom. Figure 4.7 shows the gamma error histograms for the beam configuration with contamination parameter values from equation 63. Separate histograms are shown for the regions: Before d_{max}, After d_{max}, Inside field, Penumbra, Outside field. d_{max} stands for the depth of maximum dose in the relative depth dose curve.

Several other contamination parameter values have been tested in the beam configuration. The average Gamma errors are depicted in Tab. 5 for

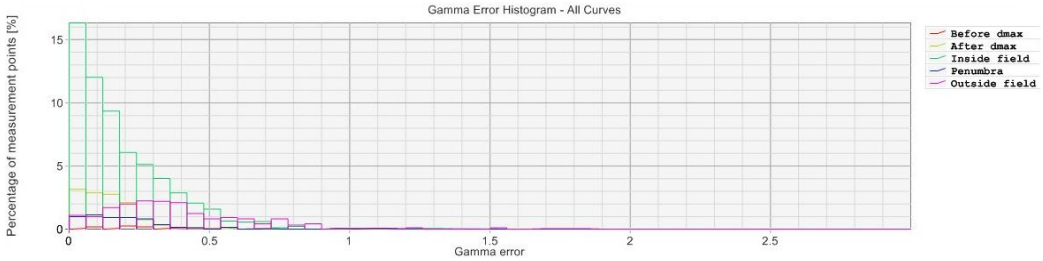

Figure 4.7: Gamma error histograms for different field regions in water for the default electron contamination configuration (see Eq. 63)

Table 5: Average Gamma errors for different electron contamination configurations

σ_0	35.3274	60	5	35.3274	35.3274	60
σ_1	410.666	410.666	410.666	200	500	410.666
c_0	0.0583	0.0583	0.0583	0.0583	0.0583	0.4
Av. γ-error in depth dose curves before d_{max}	0.33	0.42	0.16	0.82	0.45	1.07
Av. γ-error in depth dose curves after d_{max}	0.14	0.14	0.14	0.15	0.14	0.16
Av. γ-error in profiles inside field	0.19	0.19	0.18	0.27	0.18	0.29
Av. γ-error in profiles in penumbra region	0.23	0.23	0.23	0.23	0.23	0.23
Av. γ-error in profiles outside field	0.29	0.39	0.40	0.43	0.38	0.41

several configurations. The default configuration values determined by the optimization process are in the first column. The configuration in the third column (σ_0=5, σ_1=410.666, c_0=0.0583) is the only configuration whose performance is comparable to the default configuration in the first column, all other configurations have higher overall gamma errors. The average gamma error in the depth dose curves before d_{max} is lower (0.16, default: 0.33), but the error in the profiles outside field is higher (0.40, default: 0.29). Since no electron contamination parameter set with considerable better performance could be found by manual 'trial and error' optimization, the default parameter set (see Eq. 63) determined by automatic optimization was used.

5 Phantom measurements

In order to verify the dose distributions calculated in Eclipse by the algorithm Acuros XB, dose measurements in various phantoms were performed. Since the treatment of heterogeneous media in the dose calculation is of special interest, the focus was put on measurements in phantoms with heterogeneous material compositions.

The following dosimetry techniques were used:

- ion chamber dosimetry
- dosimetry with radiochromic films
- diode dosimetry
- thermoluminescence dosimetry.

The experimental results were compared to dose distributions calculated by Acuros XB and AAA.

5.1 ArcCHECK-Phantom with heterogeneities

For measuring doses in the presence of heterogeneities, the ArcCHECK phantom was used together with the modular insert, the MultiPlug (see sec. 3.3.2). Four inserts made of tissue equivalent materials were arranged in the MultiPlug.

For film dosimetry a film cassette made of RW3 material can be inserted in the center of the MultiPlug. The cutout in the cassette was filled with plates made of PMMA material with thicknesses of 1 mm and 1.6 mm. The cassette was put just beneath the heterogeneity inserts. The EBT3 films were put at different positions between the PMMA plates to perform measurements at different depths. Dose distributions were recorded at depths 1 mm, 4.2 mm and 9 mm beneath the inserts. One insert of the MultiPlug features a cavity, where an ionization chamber was placed. The setup was scanned in the CT and imported in the Eclipse treatment planning system. It can be seen in figs. 5.1 and 3.7. An application note from Sun Nuclear [58] suggests that the ArcCHECK should be modeled as a homogeneous phantom with uniform density in the TPS. Therefore the CT image of the ArcCHECK (excluding the MulitPlug) was contoured with a new structure and the original density values of the image were overridden with a uniform density of HU=244 (for Acuros XB) or HU=200 (for AAA), as the application note suggests.

Photon radiation plans were calculated on the CT scan of the phantom with a 6 MeV flattened beam. A 10x10 cm^2 static field with 250 MU was used.

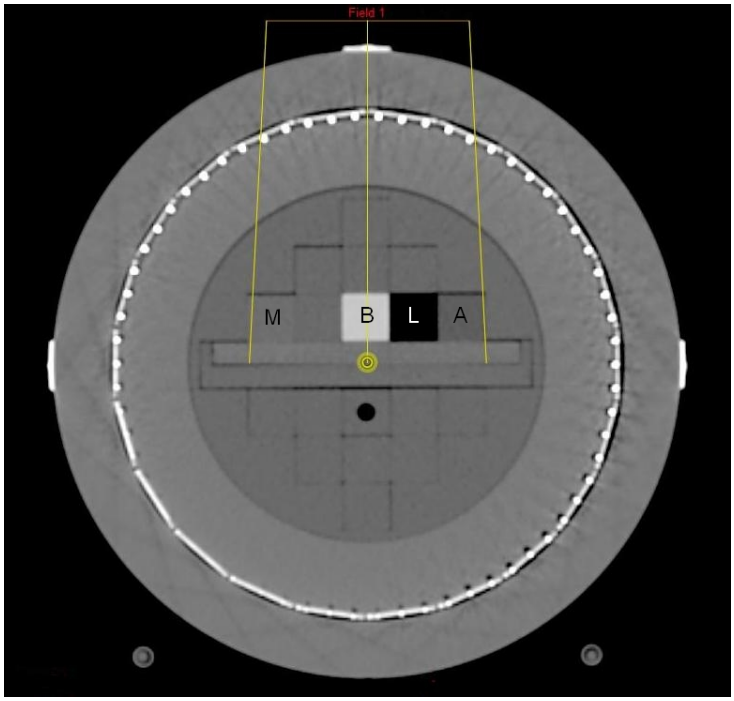

Figure 5.1: One slice of the CT scan of the ArcCHECK phantom in the setup used for measurements. The heterogeneity inserts in the center are equivalent to bone (B), muscular tissue (M), lung (L) and adipose tissue (A). All other inserts in the center are equivalent to water.

The source-surface-distance (SSD) was 86.6 cm. The field can be seen in Fig. 5.1. Dose distributions were calculated with AAA, AXB in dose-to-medium mode (D_M) and AXB in dose-to-water mode (D_W). All measurements were compared to those three different calculations.

5.1.1 Radiochromic film dosimetry

The dose distributions behind the tissue-equivalent materials were measured with EBT3 films. Figure 5.2(a) shows the dose distribution measured at the horizontal plane with distance 1 mm beneath the inserts and Fig. 5.2(b)-(d) shows the dose distribution at the same location, but calculated by the three algorithms AAA, AXB D_M and AXB D_W.

For better visualization of the differences between the dose distributions, the one-dimensional dose profiles along the black line indicated in Fig. 5.2(a) are presented in Fig. 5.3. In this plot it is obvious that the calculation by AXB D_M is in better agreement with the measurement than the other two methods. Especially in the lower dose region behind the bone insert the AAA

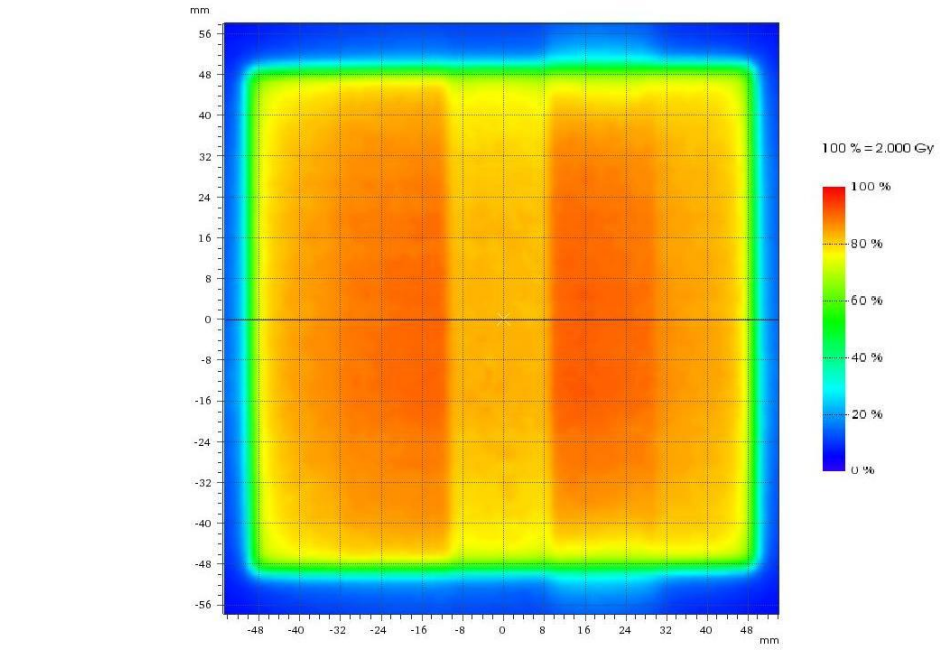

(a) EBT3

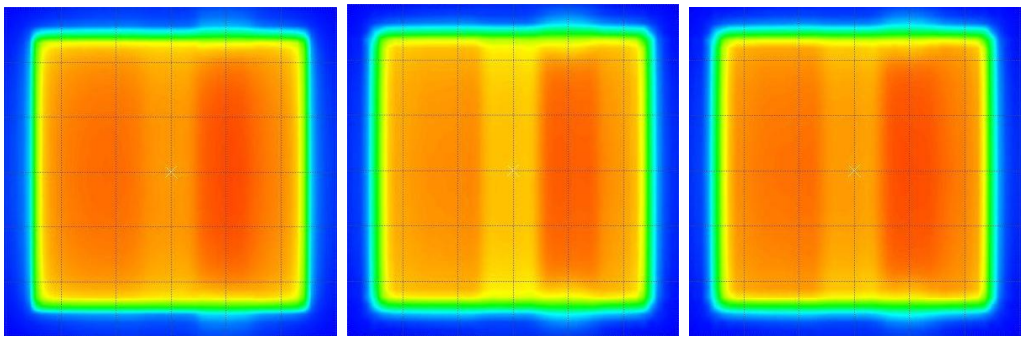

(b) AAA (c) AXB D_M (d) AXB D_W

Figure 5.2: Dose distributions in horizontal plane with distance 1 mm to heterogeneities, measured with EBT3 (a) and calculated in the TPS (b)-(d). The dose value is coded by the color scheme on the right

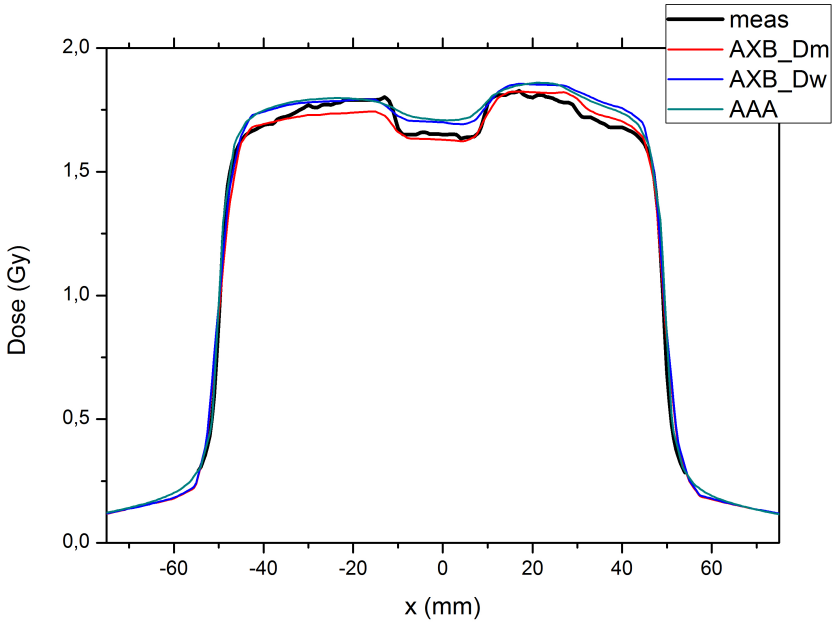

Figure 5.3: Dose profiles along the black line as indicated in Fig. 5.2(a). Profile measured with EBT3 and profiles calculated by the TPS are shown

and the AXB D_W calculations clearly overpredict the dose. Otherwise AXB D_M calculates a dose value too low behind the water-equivalent insert.

For further quantification of the agreement between the dose distributions a 2D gamma analysis was performed where the calculated distributions were compared to the measured dose distribution. The gamma criterion was set to 3 mm/3%. Additionally all dose values below 10% of the maximum dose of the measured data set were suppressed. Figure 5.4 shows the gamma value distributions for all three calculations at the depths 1 mm, 4.2 mm and 9 mm beneath the heterogeneities.

In all three cases, the AXB D_M algorithm clearly outperforms the other two calculations. For the AAA, high gamma values appear especially in the regions behind the bone, lung and adipose inserts. The AXB D_W shows larger differences to the measurement behind the adipose and lung inserts. At depth 1 mm the AXB D_M underpredicts the dose behind the water insert (see Fig. 5.3), but this trend is not seen in the other two film measurements.

Table 6 gives the gamma agreement index (GAI) for all three calculations at every depth where a film measurement was performed. The GAI is the percentage of measuring points that pass the gamma criterion ($\gamma < 1$) when compared to a certain dose calculation.

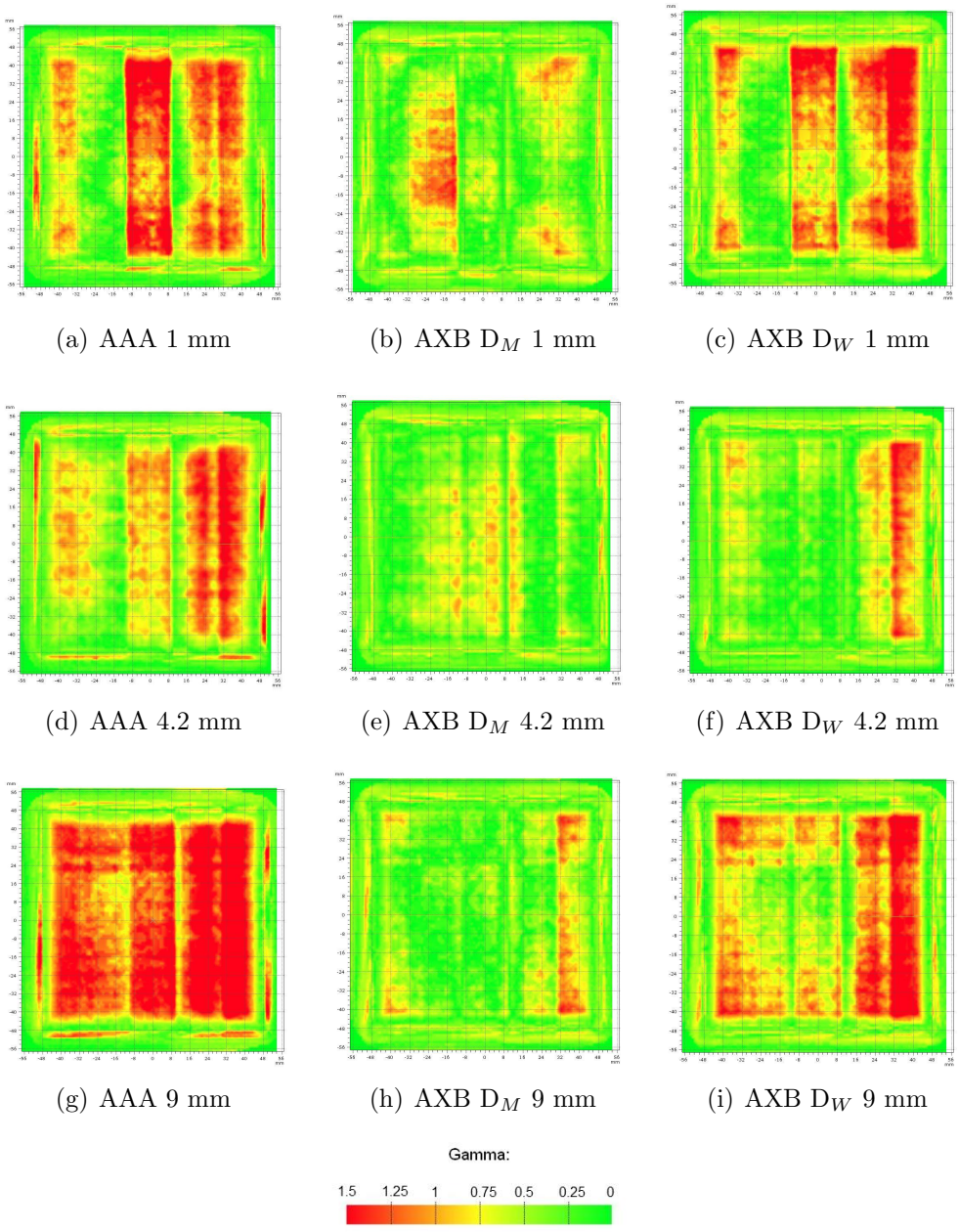

(a) AAA 1 mm (b) AXB D_M 1 mm (c) AXB D_W 1 mm

(d) AAA 4.2 mm (e) AXB D_M 4.2 mm (f) AXB D_W 4.2 mm

(g) AAA 9 mm (h) AXB D_M 9 mm (i) AXB D_W 9 mm

Figure 5.4: Gamma value distributions in horizontal plane with distances 1 mm, 4.2 mm and 9 mm to heterogeneities for three calculations. The gamma value is coded by the color scheme at the bottom

Table 6: Gamma agreement index with gamma criterion 3 mm/3% for three calculations at depth d

Depth d	AAA	AXB D_M	AXB D_W
1 mm	75.4%	95.9%	78.5%
4.2 mm	81.6%	99.6%	94.2%
9 mm	48.6%	97.6%	78.2%

Table 7: Dose values calculated by the TPS and their relative errors to the chamber measurement in the ArcCHECK phantom

Algorithm	Dose (Gy)	relative error
AAA	1.460	1.06%
AXB D_M	1.415	-2.05%
AXB D_W	1.410	-2.40%

The AXB D_M dose calculation clearly shows better agreement with all three measurements.

5.1.2 Ionization chamber dosimetry

The dose in the center of the ArcCHECK phantom was measured with an ionization chamber. The chamber was inserted in the cavity that can be seen in Fig. 5.1 and was placed in the central axis of the field. As the chamber integrates the dose over a certain volume given by its dimensions, the measurement can not be compared to a point dose calculated by the treatment planning software. Therefore a small volume, representing the chamber volume, was contoured and assigned with water density in Eclipse and the mean dose in this volume was calculated, which gives a comparable value to the measurement.

The dose was measured three times and a mean dose value of D_{mean} =1.445 Gy was obtained. Table 7 shows the three dose values calculated in Eclipse and their relative errors to D_{mean}.

The dose calculated by AAA is in very good agreement with the measurement. The two AXB calculations perform worse and underpredict the dose by more than 2%.

5.1.3 ArcCHECK diode measurement

The dose was also measured with the diode array of the ArcCHECK phantom. The dose distribution measured by the cylindrical phantom is mapped

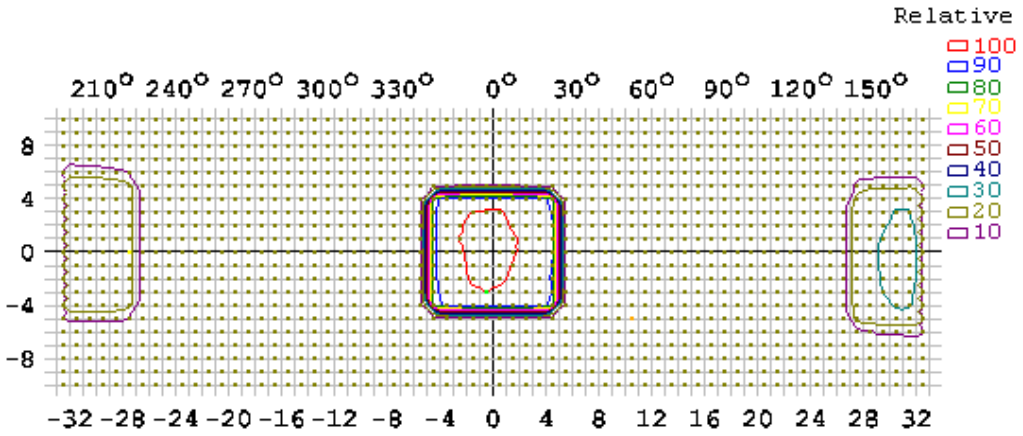

Figure 5.5: Dose distribution measured by the ArcCHECK diode array. Relative isodose curves are shown.

Table 8: Average Gamma agreement indices of three calculations with reference to diode array measurement in the ArcCHECK phantom. Gamma criterion: 1 mm/1%.

Algorithm	**Average GAI**
AAA	96.3%
AXB D_M	92.8%
AXB D_W	92.4%

onto a 2D dose distribution. The measured dose distribution is depicted in Fig. 5.5. The measurement was repeated three times.

The dose distributions calculated by the TPS are compared to the measurement by Gamma index evaluation. The gamma criterion was set to 1 mm/1% and a minimum dose threshold of 10% was set. The dose was calculated with AAA, AXB D_M and AXB D_W. Maps of measuring points failing the gamma criterion are shown in Fig. 5.6. The average gamma agreement indices, which were derived from three measurements, are shown in Tab. 8.

The AAA calculation is in better agreement with the measurement than the two AXB modes. The points failing the gamma analysis are mainly located at the field edge for all calculations. All three calculations have a GAI of more than 90% in this analysis with a very stringent criterion. In this setup this measurement technique is not suited very well to test the treatment of heterogeneous materials in the dose calculation algorithm, as the the diodes are located far away from the inhomogeneity inserts.

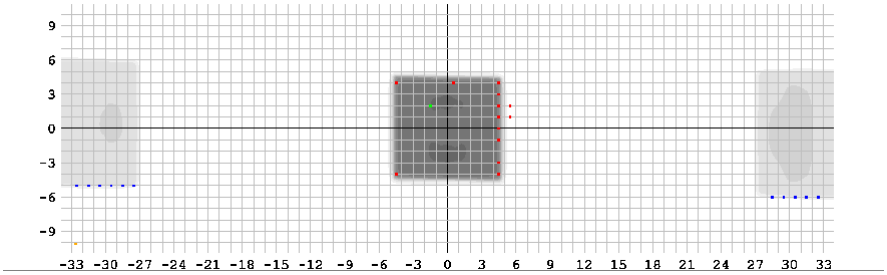

(a) AAA

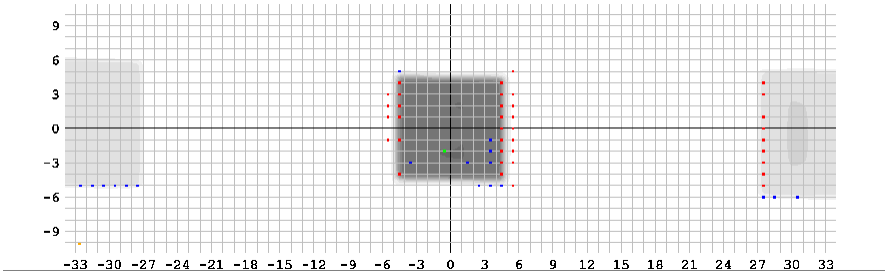

(b) AXB D_M

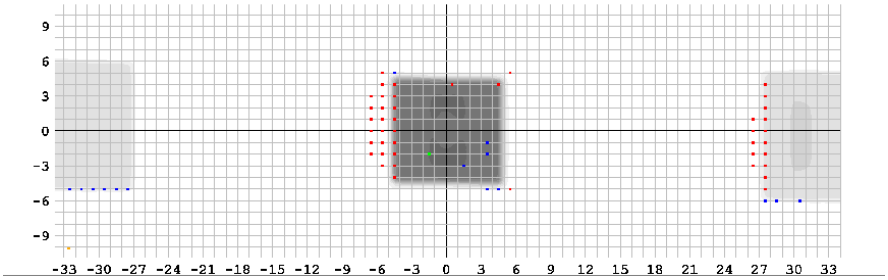

(c) AXB D_W

Figure 5.6: Measuring points failing the gamma criterion (1 mm/1%) for three calculations in the ArcCHECK diode array. Red: hot spots, Blue: cold spots, Green: reference point

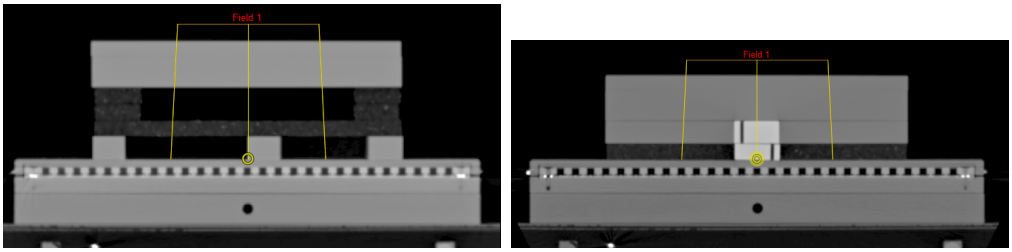

(a) Setup A (b) Setup B

Figure 5.7: CT scans of the two different slab arrangements on the seven29 array. The yellow lines indicate a 10x10 cm^2 field

5.2 Slab phantom measurements

The slab phantom described in sec. 3.3.6 was used to perform more measurements in inhomogeneous media. Several different material configurations were realized and dose distributions were measured with EBT3 dosimetry films and the seven29 ionization chamber array.

5.2.1 Seven29 chamber array

The seven29 chamber array (see sec. 3.3.3) was used to measure the two-dimensional dose distributions in the plane normal to the beam central axis after the photon beam has passed a configuration of several inhomogeneous slabs.

The same slab arrangements that were used in measurements were scanned in the CT together with the chamber array to import into Eclipse. Two different configurations were realized, both shown in Fig. 5.7. The configurations are named setup A (A for air) and setup B (B for bone). Both setups feature 3 cm of PMMA on the top for dose buildup. In setup A this is followed by 3 cm of cork with cutouts for air gaps. The last slab is a 1.5 cm thick PMMA plate, also with cutouts for air. In setup B the buildup section is followed by a 1.5 cm PMMA plate with a cutout in center that is filled by a bone-equivalent cylinder. The next slab is a 1 cm cork plate which also features the bone cylinder in the center.

The slab phantom was put onto the chamber array without the PMMA stand. This leads to some uncertainties in the positioning of the slabs since they are not fixed laterally. A static field with gantry and collimator angle of 0 degrees was used for photon radiation with beam energy of 6 MeV. The distance source to chamber array was set to 100 cm. Two different field sizes were used: 10x10 cm^2 and 20x20 cm^2, both with 200 MU. For measurements with the 10x10 cm^2 field, the resolution of the chamber array was improved

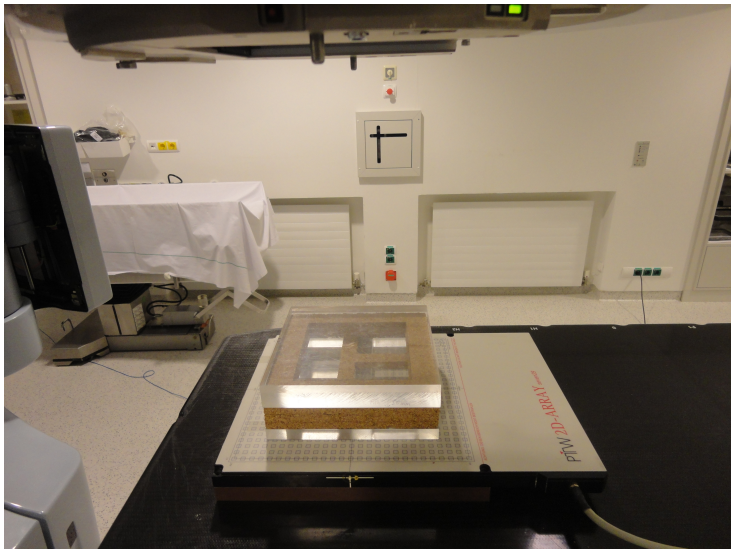

Figure 5.8: Slab phantom in setup A on top of the seven29 array in the treatment room

by performing the experiment four times and shifting the array by 5 mm after each measurement. Figure 5.8 shows the phantom in setup A on the chamber array under the treatment machine.

For the dose calculation on the CT scan in Eclipse, the volume structure which holds the ionization chambers had to be overridden with water material (HU=-8) as the chambers are measuring the dose to water. This procedure is described in [59]. The horizontal dose plane, which cuts the chamber volume in half, was exported. The calculations of AAA and AXB D_M were exported. Since the material of the detectors is defined as water in the TPS, the two Acuros dose-reporting modes D_M and D_W would result in basically the same dose distribution calculated in the measuring plane. For the rest of this section, the AXB D_M calculation is just referred to as AXB.

Figure 5.9 shows the dose distributions as calculated in Eclipse in the measuring plane of setup A for a 20x20 cm^2 field. On the right hand side the dose profiles along the line indicated on the left are presented. The dots represent the measurements of the chamber array. Blue and red dots stand for measuring points, which fail the gamma criterion (2 mm/2%) with a dose value lower or higher than the calculation. The AXB dose profile shows better agreement with the measurements. AAA overpredicts the dose especially in the region after air gaps.

Figure 5.10 shows the dose distribution calculated and measured in setup B for a 20x20 cm^2 field. The dose profile from left to right through the center

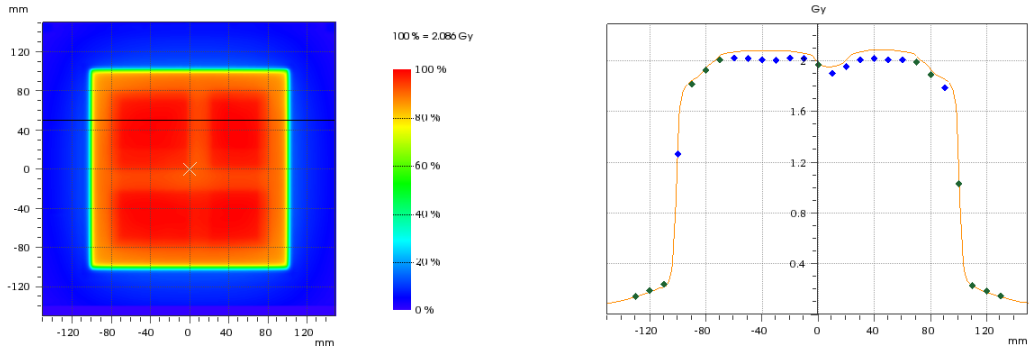

(a) AAA

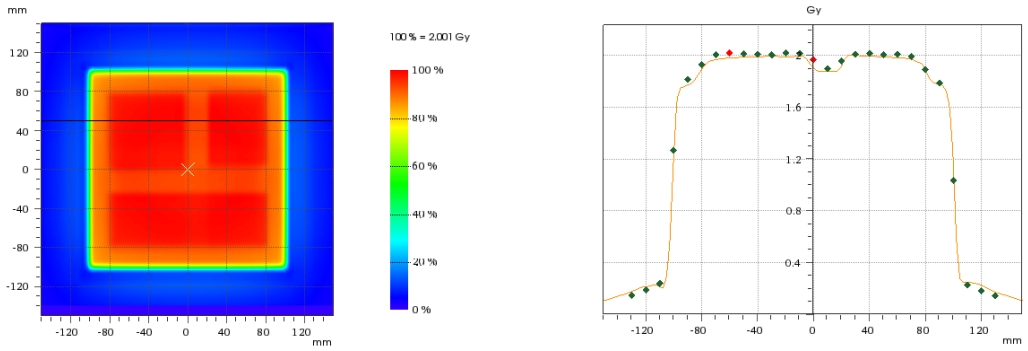

(b) AXB

Figure 5.9: Left: Dose planes as calculated by AAA and AXB in setup A for field size 20x20 cm^2, Right: Dose profiles calculated along the line indicated on the left and measuring points

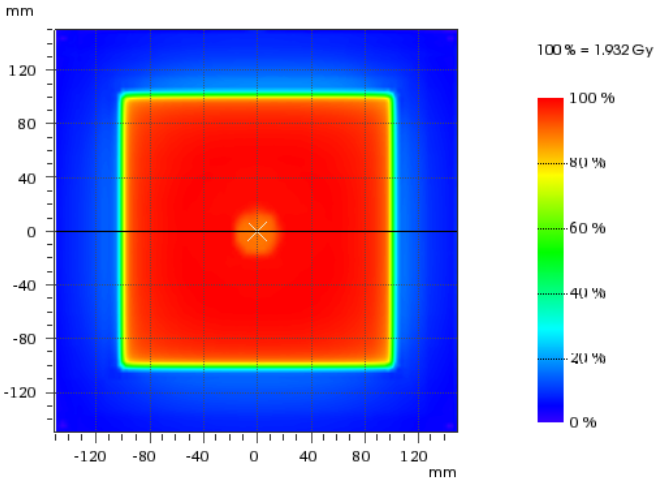

(a) AXB dose plane

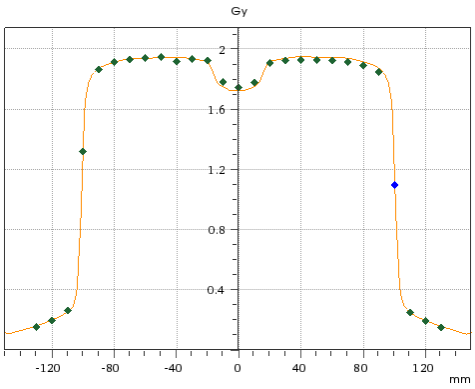

(b) AAA dose profile

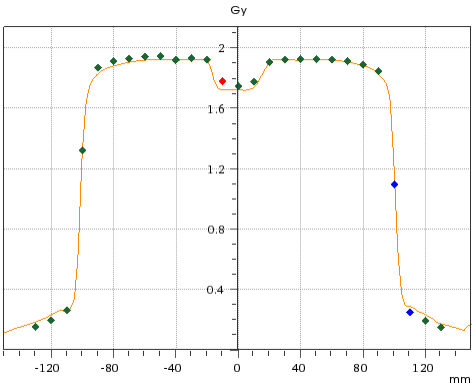

(c) AXB dose profile

Figure 5.10: (a) dose plane as calculated by AXB in setup B for field size 20x20 cm^2, (b) and (c) dose profiles calculated along the line indicated in a) and measuring points

Table 9: Gamma agreement indices (criterion: 2 mm/2 %) for AAA and AXB in setups A and B

Setup A:	**Field size (cm^2)**	**AAA GAI**	**AXB GAI**
	10x10	44.7 %	93.9 %
	20x20	49.3 %	93.8 %
Setup B:	**Field size (cm^2)**	**AAA GAI**	**AXB GAI**
	10x10	89.6 %	90.9 %
	20x20	91.4 %	90.0 %

was calculated by AAA and AXB is compared to the measurement in (b) and (c). Both algorithms show a good agreement with the measurement, but AXB has the tendency to underestimate the dose.

A 2D gamma analysis was performed with the gamma criterion 2 mm/2%. Dose values below a threshold of 10% of the maximum measured value were suppressed. The results for field sizes 10x10 cm^2 and 20x20 cm^2 are depicted in Tab. 9.

AXB clearly outperforms AAA in setup A, while in setup B both algorithms show comparable results. The AAA dose has larger discrepancies to the measurement in phantoms where air gaps are present. The AXB calculation has a gamma agreement of more than 90% in all configurations.

To visualize the dose distribution parallel to the beam direction, depth dose curves along the directions indicated in Fig. 5.11(a)-(b) were exported from the TPS. In setup A, a depth dose curve off-axis parallel to the beam central axis was used, and in setup B a depth dose curve along the beam central axis was used. The curves calculated for a 10x10 cm^2 field with AXB and AAA for the two phantom setups are depicted in Fig. 5.11. Also included in the plot is the measured dose value by one ionization chamber of the array that lies on the curve. The dose was calculated as the mean dose value from three individual measurements, the standard deviation is shown as error bar.

The very different treatment of inhomogeneities by the AAA and AXB algorithms can be seen clearly in the depth dose curves, where large deviations occur especially in the air regions. In setup A the AXB calculation shows very good agreement with the measured point dose, whereas the AAA-calculated dose is more than 2% too high. In setup B, the AAA calculates a higher dose in bone than AXB, but at the depth of the array, both curves coincide and show good agreement with the measurement.

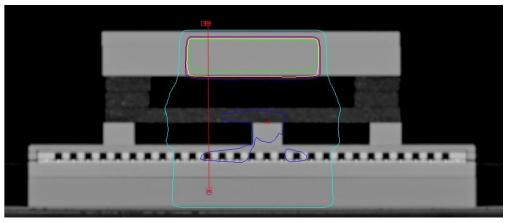

(a) Setup A

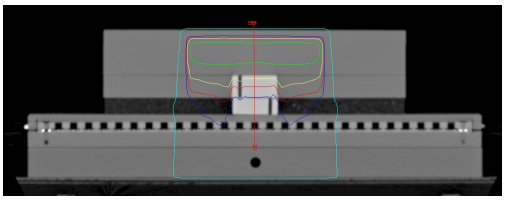

(b) Setup B

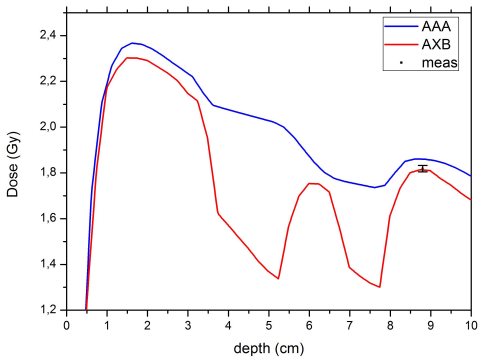

(c) Setup A depth dose

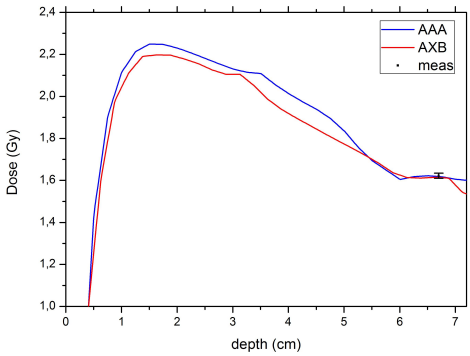

(d) Setup B depth dose

Figure 5.11: Depth dose curves for the two slab phantom setups on the seven29 array, the location of the curves are indicated in (a) and (b), field size: 10x10 cm^2

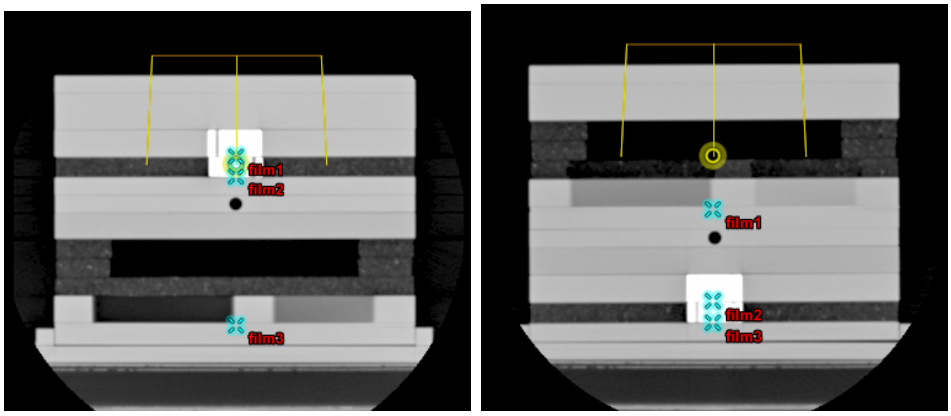

(a) Setup C (b) Setup D

Figure 5.12: CT scans of the two different slab arrangements used for film dosimetry. The yellow lines indicate a 10x10 cm^2 field. The blue crosses indicate the positions of the EBT3 films.

5.2.2 Radiochromic film dosimetry

EBT3 radiochromic films were used to measure the dose distributions in the slab phantom. An advantage over dosimetry with the chamber array is, that the films can be placed inside the phantom between the slabs, allowing for measurements right at the interface between different materials.

The slabs were arranged in two different configurations, which are depicted in Fig. 5.12. The arrangements are similar to the ones used with the seven29 array. Setup C is composed of setup A on the top and setup B (without the 3 cm buildup) on the bottom with a 3.5 cm thick spacer of PMMA and water-equivalent material in between. Setup D has the same arrangement, but the A and B parts are exchanged. Both setups C and D allow for measurements with an ionization chamber in the center of the phantom. Both setups are used with the PMMA stand. Setup C can be seen in Fig. 3.11. The EBT3 films were cut to size 20x20 cm^2 and placed in horizontal planes between the slabs at the locations marked in Fig. 5.12.

For both phantom setups a dose distribution on the CT scan was calculated with a static 10x10 cm^2 photon field. The beam energy was 6 MeV and 250 MU were used. Gantry and collimator angles were 0 degrees. SSD was 94.9 cm for both setups. The dose was calculated with AAA, AXB D_M and AXB D_W and the horizontal dose planes at the locations of the films were exported.

The film measurements in the slab phantoms were performed three times in each setup. To suppress noise in the measured dose, the mean 2D dose dis-

Table 10: Gamma agreement indices (criterion: 3 mm/3 %) for AAA, AXB D_M and AXB D_W in setups C and D

Setup C:	**AAA GAI**	**AXB D_M GAI**	**AXB D_W GAI**
Film 1	87.3%	95.1%	80.8%
Film 2	87.5%	99.9%	94.7%
Film 3	48.2%	90.6%	90.1%
Setup D:	**AAA GAI**	**AXB D_M GAI**	**AXB D_W GAI**
Film 1	55.3%	89.6%	81.3%
Film 2	39.8%	79.9%	63.1%
Film 3	77.7%	95.2%	77.9%

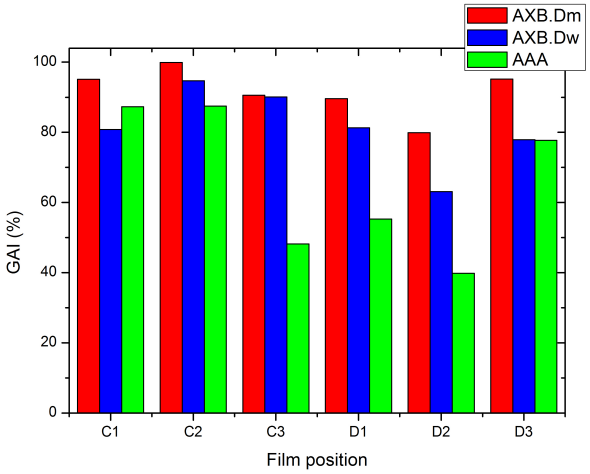

Figure 5.13: Gamma agreement indices from three measurements for AAA, AXB D_M and AXB D_W in setups C and D

tribution was calculated from the three films. The mean measured dose distribution was compared to the dose calculation by performing a 2D-Gamma-analysis. The gamma criterion was set to 3 mm/3% and dose values below 10% of the maximum dose were suppressed. The Gamma agreement index was determined for each film position and for each calculation and it is shown in Tab. 10 and in Fig. 5.13.

For all film positions the AXB D_M calculation is in best agreement with the measured dose distribution. AXB D_W performs better than AAA except for the film position C1. Figures 5.14 and 5.15 present the gamma index distributions and the points failing the gamma analysis for setup C, figs. 5.16 and 5.17 present the same for setup D. As already seen in the chamber array measurements, AAA has difficulties calculating the dose behind air

Table 11: Dose values calculated by the TPS and their relative errors to the chamber measurement in the slab phantom

Setup C:	**Dose (Gy)**	**relative error**
AAA	1.951	1.20%
AXB D_M	1.911	-0.88%
AXB D_W	1.914	-0.72%
Setup D:	**Dose (Gy)**	**relative error**
AAA	2.056	3.85%
AXB D_M	2.010	1.52%
AXB D_W	2.004	1.22%

gaps, which is where films C3 and D1 are placed. AAA overestimates the dose behind air. AXB D_M and AXB D_W show deviations to the measurement in the bone region. At positions C1 and D2, where the film is placed between bone structures, the AXB algorithm underpredicts the dose in the D_M mode and overpredicts dose in the D_W mode. This improves for the D_M mode right behind the bone insert (positions C2 and D3).

Additionally to the film measurements, the dose in the center of the slab phantom was measured with an ionization chamber. The cavity which accommodates the chamber can be seen in Fig. 5.12. The dose was measured three times and mean dose values of $D_{mean,C} = 1.928$ Gy and $D_{mean,D} = 1.980$ Gy were obtained for setups C and D. The doses calculated by the algorithms and the relative errors to D_{mean} are shown in Tab. 11. For setup C all three calculations are in good agreement with the chamber measurement. In setup D, where the chamber is located behind an air gap, AAA overestimates the dose by more than 3%.

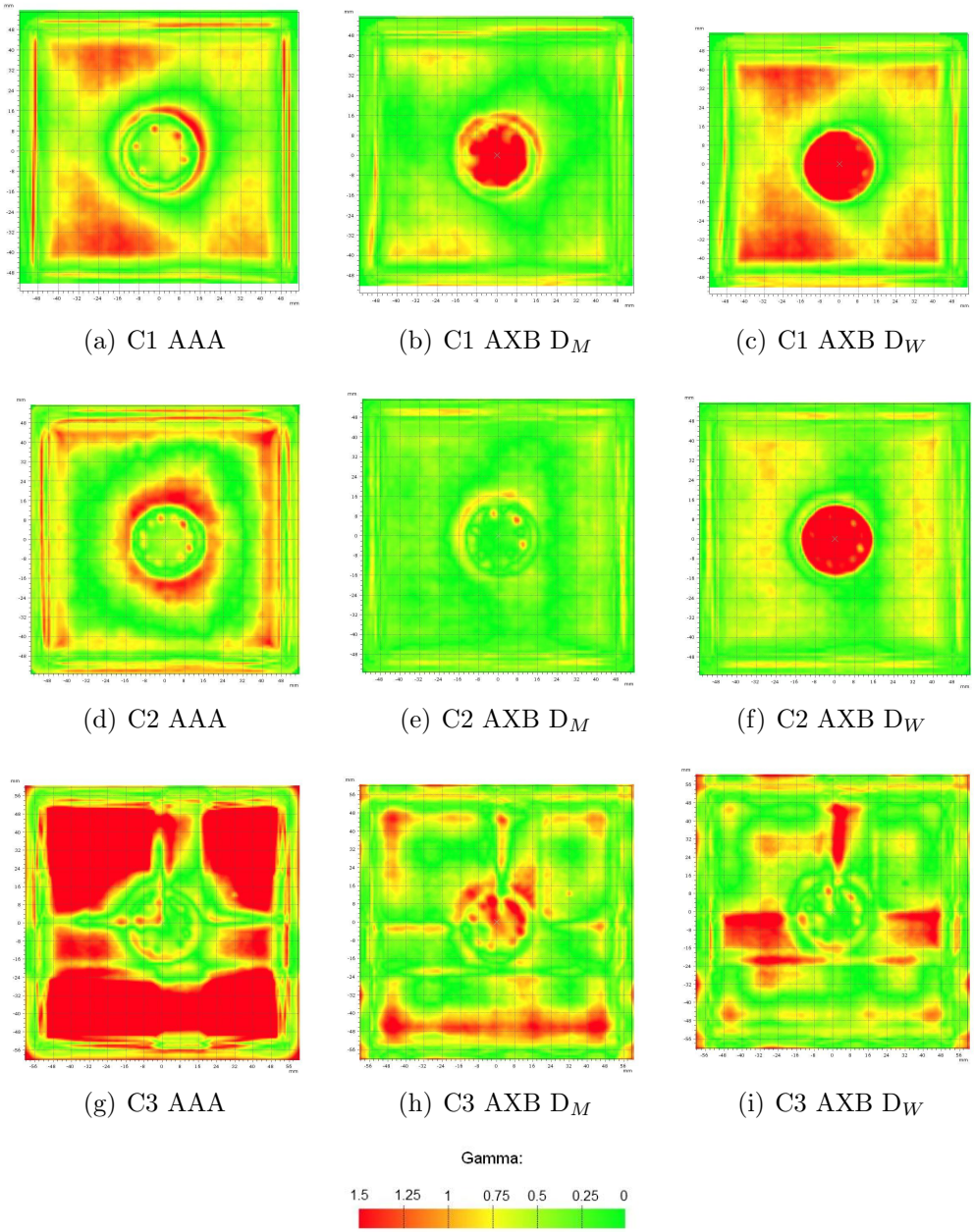

(a) C1 AAA (b) C1 AXB D_M (c) C1 AXB D_W

(d) C2 AAA (e) C2 AXB D_M (f) C2 AXB D_W

(g) C3 AAA (h) C3 AXB D_M (i) C3 AXB D_W

Figure 5.14: Gamma value distributions for three film positions in setup C. The gamma value is coded by the color scheme at the bottom

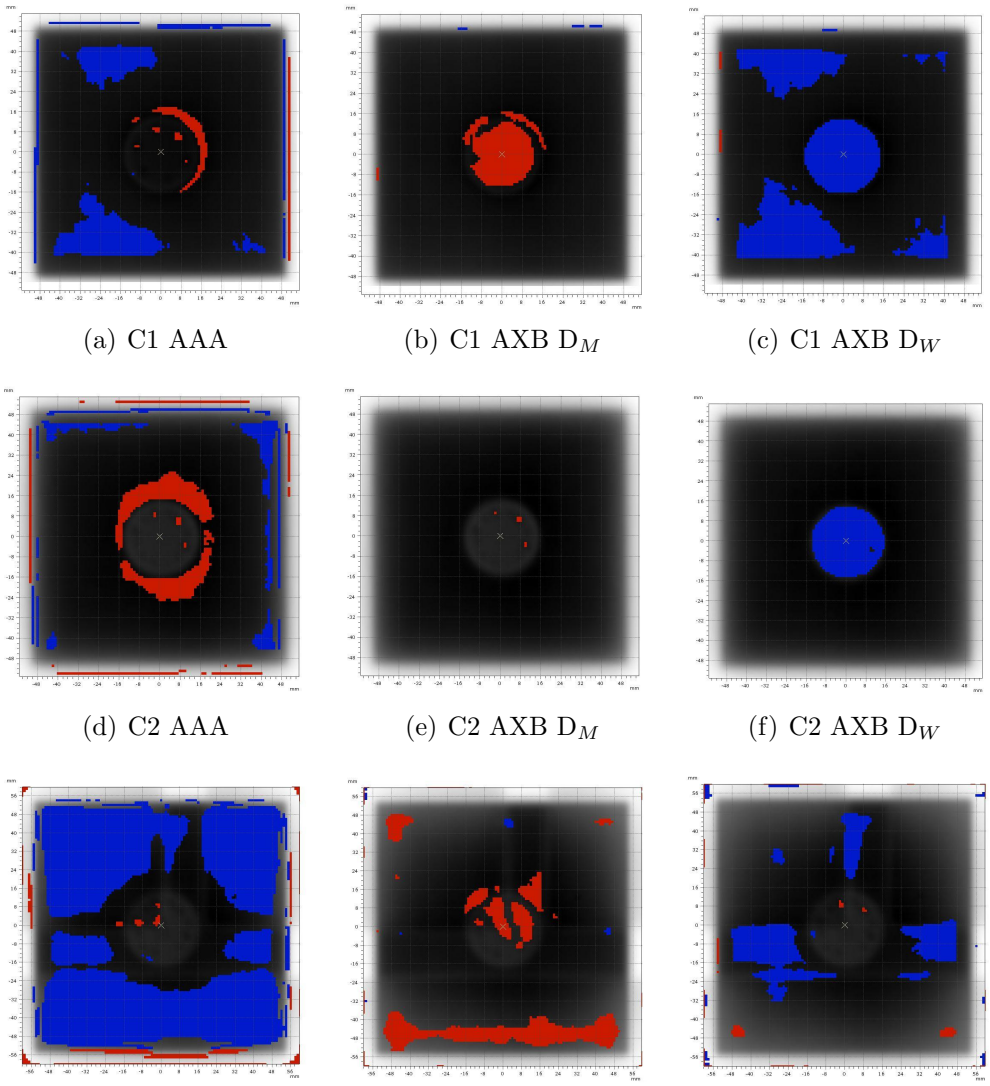

(a) C1 AAA (b) C1 AXB D_M (c) C1 AXB D_W

(d) C2 AAA (e) C2 AXB D_M (f) C2 AXB D_W

(g) C3 AAA (h) C3 AXB D_M (i) C3 AXB D_W

Figure 5.15: Points failing the Gamma evaluation for three film positions in setup C. Red: hot spots, dose underestimated; Blue: cold spots, dose overestimated

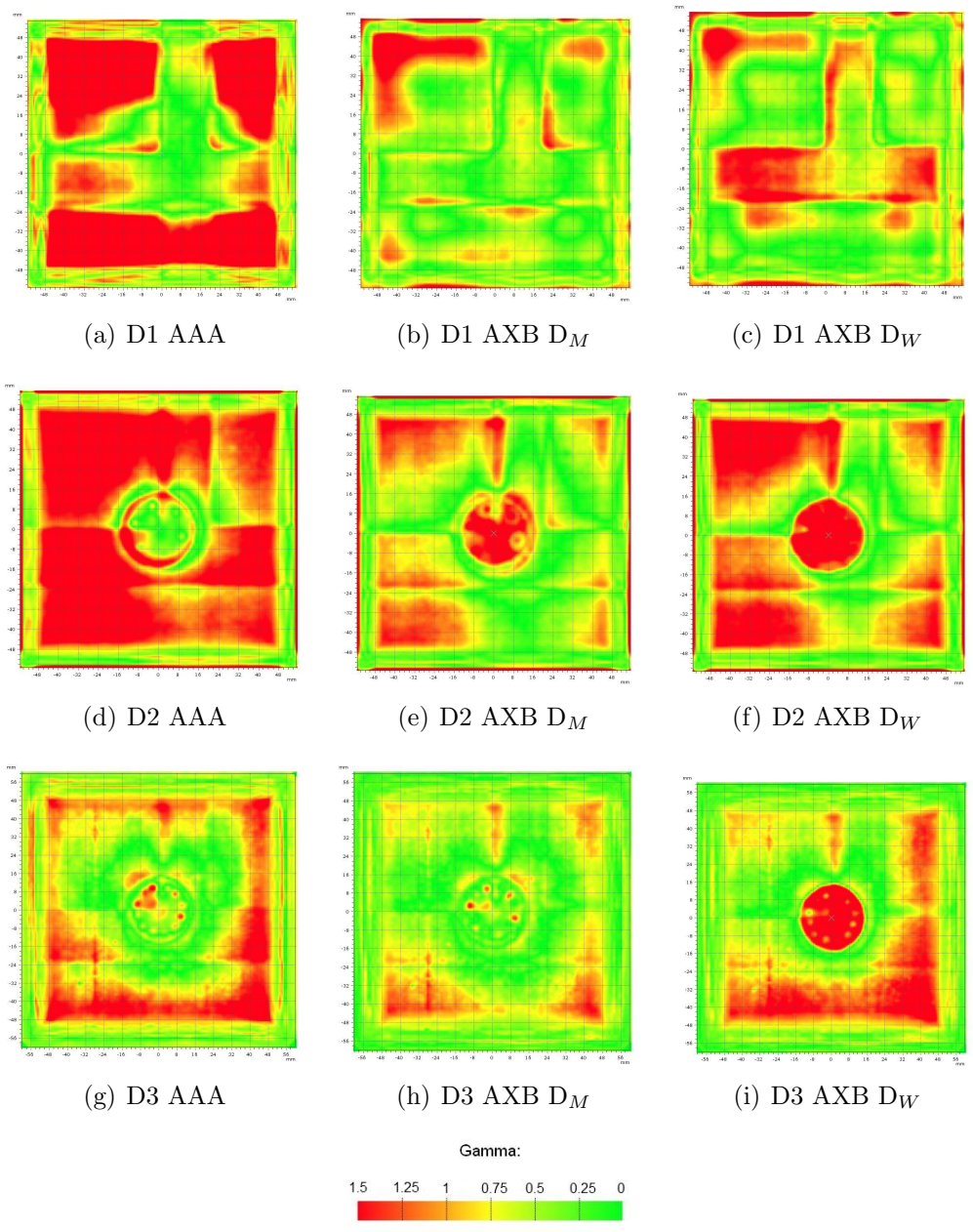

(a) D1 AAA (b) D1 AXB D_M (c) D1 AXB D_W

(d) D2 AAA (e) D2 AXB D_M (f) D2 AXB D_W

(g) D3 AAA (h) D3 AXB D_M (i) D3 AXB D_W

Figure 5.16: Gamma value distributions for three film positions in setup D. The gamma value is coded by the color scheme at the bottom

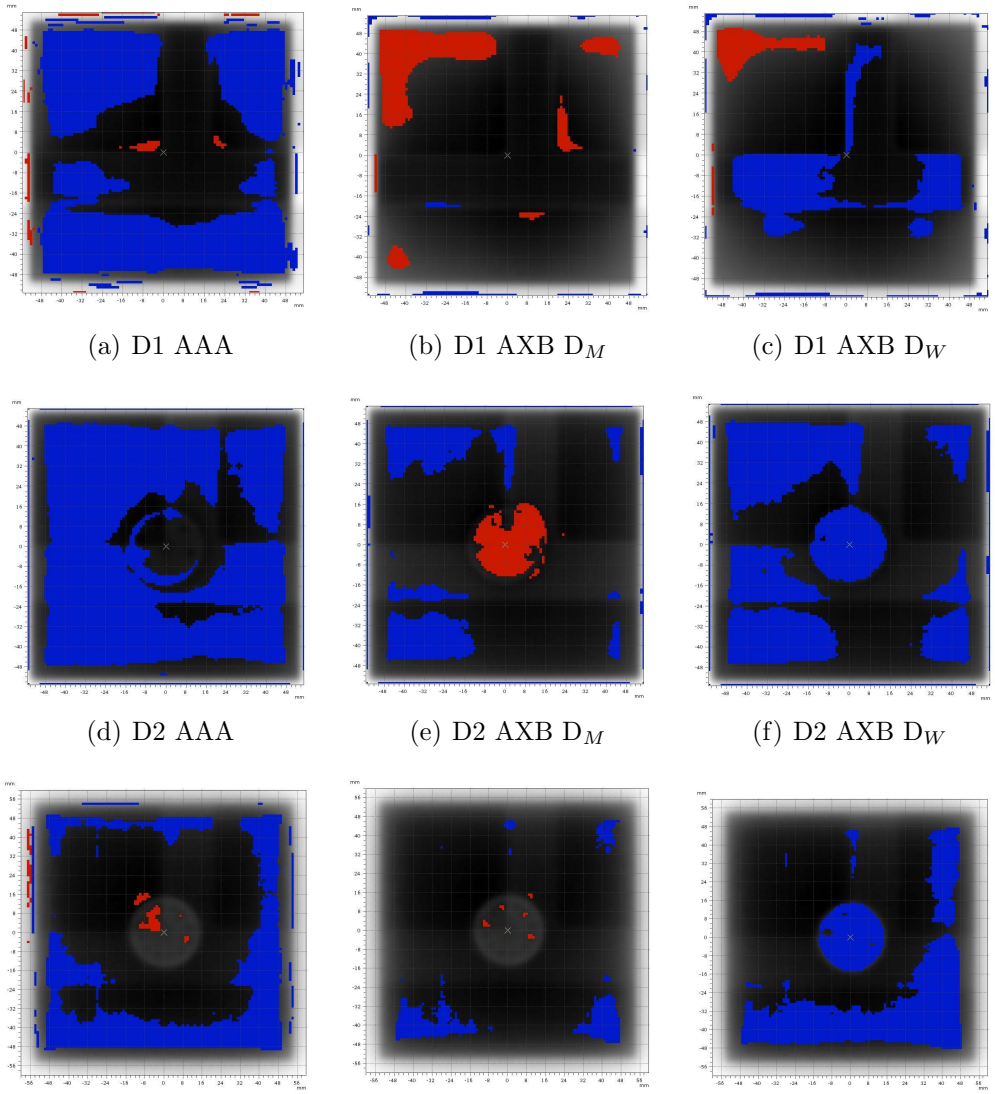

(a) D1 AAA (b) D1 AXB D_M (c) D1 AXB D_W

(d) D2 AAA (e) D2 AXB D_M (f) D2 AXB D_W

(g) D3 AAA (h) D3 AXB D_M (i) D3 AXB D_W

Figure 5.17: Points failing the Gamma evaluation for three film positions in setup D. Red: hot spots, dose underestimated; Blue: cold spots, dose overestimated

5.3 Thermoluminescence dosimetry in the anthropomorphous phantom

The experiments described above were all conducted in simple geometric phantoms with a single open field.

In a radiation treatment, the dose is usually delivered by a rotating gantry. A sophisticated treatment technique is the Volumetric Modulated Arc Therapy (VMAT). Here, the dose rate and the shape of the field is continuously modulated by the MLC during the rotation. A rotation segment of the gantry is called an arc.

The performance of the AXB algorithm in clinical VMAT treatment plans is evaluated by thermoluminescence dosimetry. For these experiments the anthropomorphous ATOM phantom (sec. 3.3.7) was used. The phantom was scanned inside the CT and the scans were imported into the Eclipse TPS. Two VMAT treatment plans were created for two different tumor sites. Target volumes for a tumor in the head and neck region and a tumor in the lung were contoured on the CT scan. The two treatment plans were optimized by the TPS for optimal dose delivery to the target volume. For optimization and initial dose calculation the AAA algorithm was used. Then the dose distributions in the treatment plans were recalculated with the same monitor units by the AXB D_M algorithm.

The TLDs used were chips made out of LiF:Mg,Ti (TLD-100). The dimensions of the chips were 3x3x1 mm^3. For the measurement of point doses in the ATOM phantom, the TLD chips were inserted at the positions of the rod-shaped plugs in several slices of the irradiated volume. For this purpose, the tissue equivalent rods at the measurement points were shortened by $\sim$0.5 cm to create a cavity, which can hold the TLDs. The chips were positioned on the top end of a phantom section. The TLDs were put in a plastic foil for protection and two chips were put at each measurement point. The TLD holes could be seen on the CT scans and the computed dose at these positions could be determined in the TPS. The uncertainty of the TLD position on the CT is 3 mm. The overall measuring accuracy of the TLD chips in the phantom was was found to be $\pm$5% in a former thesis [60].

For one measurement the ATOM phantom was equipped with the TLD chips and set up in the treatment room for irradiation. To achieve exact positioning of the phantom under the linac, a laser positioning system and the On Board Imager (OBI) were used (see Fig. 5.18). The OBI records two kV images in orthogonal directions of the phantom on the treatment couch. These images are matched with reconstructed images from the CT scan and allow for exact repositioning of the couch. The additional dose in the TLDs from the OBI imaging is negligible.

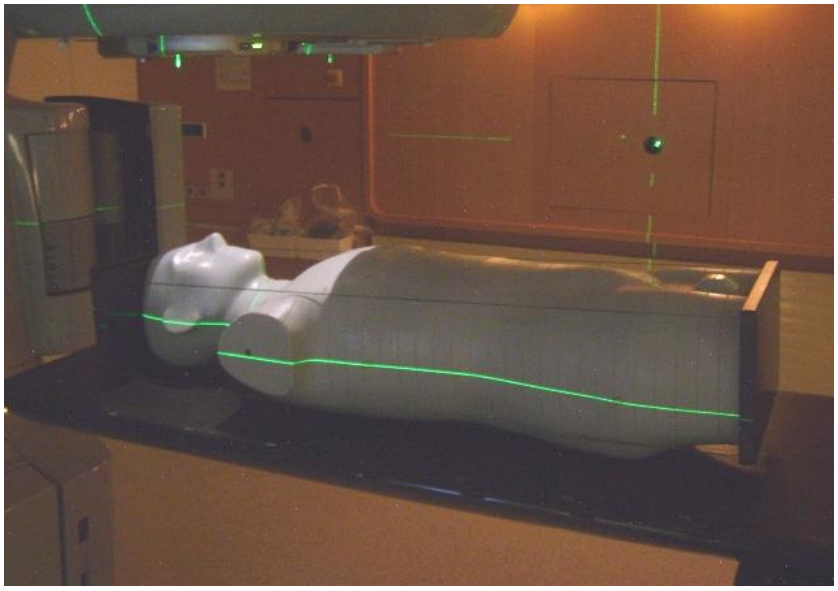

Figure 5.18: Positioning of the ATOM phantom on the treatment couch at the linac.

One fraction of the treatment plan was delivered. After irradiation the TLD chips were removed. The readout of the crystals was done 17 hours later. Before the readout process, the chips were heat treated in an oven at 100°C for 30 minutes. This eliminates the lower energy peaks in the glow curve. After that the TLD glow curves were recorded in a Harshaw 5500 reader and the dose was determined. Since only one fraction was delivered to the phantom, the measured dose was multiplied with the total number of fractions in the treatment plan to give the total dose as it is displayed in the TPS. The mean dose value of the two TLDs per measurement point was calculated.

5.3.1 Head and neck region

The treatment plan for the head and neck tumor featured two arcs. The prescription dose was 50 Gy delivered in 25 fractions. For the measurement, just one fraction of 2 Gy was irradiated on the phantom. In total 11 measurement points were selected for the TLDs in the head and neck region. The points were chosen to cover different biological materials: soft tissue, bone, spinal cord tissue and interfaces between those materials. Some of the points were located inside the target volume, some outside, where a lower dose is delivered. Figure 5.19 shows the positions of the TLDs.

Figure 5.20(a) shows the dose measured by TLD and calculated with AAA

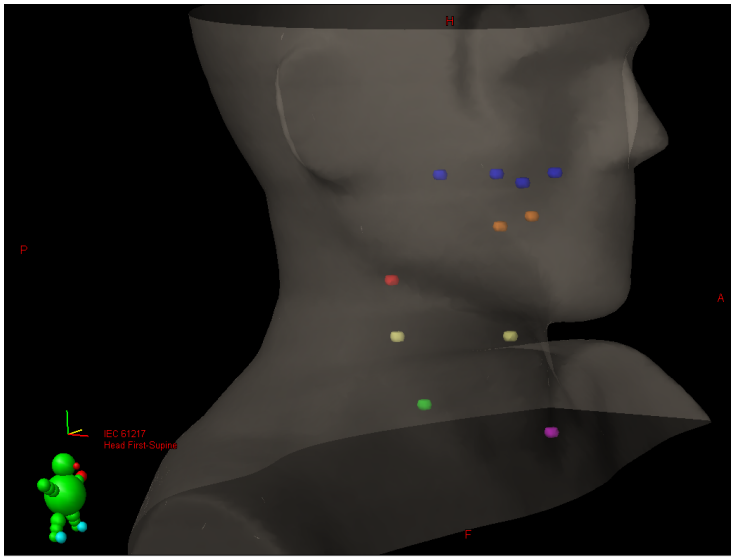

Figure 5.19: Positions of the 11 TLDs in the head and neck region. Points of the same color are in the same phantom layer

and AXB for the 11 measurement points; Fig. 5.20(b) presents the relative deviation of the dose calculations to the measurement. The dose difference between the measurement and the calculations is higher than the dose difference between the two calculations. Therefore it is not possible to compare the accuracy of the two algorithms. The technique of thermoluminescence dosimetry is not precise enough in this environment for this problem. It is noteworthy, that the deviation between measurement and calculation is less than 10% for all measurement points that are located inside the target volume (points: 3, 4, 5, 6, 8, 10, 11), a region with a rather homogeneous dose distribution and low dose gradients.

5.3.2 Lung region

The treatment plan for the lung tumor featured three arcs. The prescription dose was 10 Gy delivered in 2 fractions, and again only one fraction was delivered for the experiment. In total 7 measurement points were selected for the TLDs in the lung region. Again points in different biological materials (soft tissue, lung tissue and bone) were chosen. One measurement point was placed in the target volume. Figure 5.21 shows the positions of the TLDs in the lung region. Whereas all other TLD chips were placed on the top end of a layer, the chip represented by the red dot, was placed in the center of a layer.

Figure 5.22(a) presents the measured and calculated dose values for the

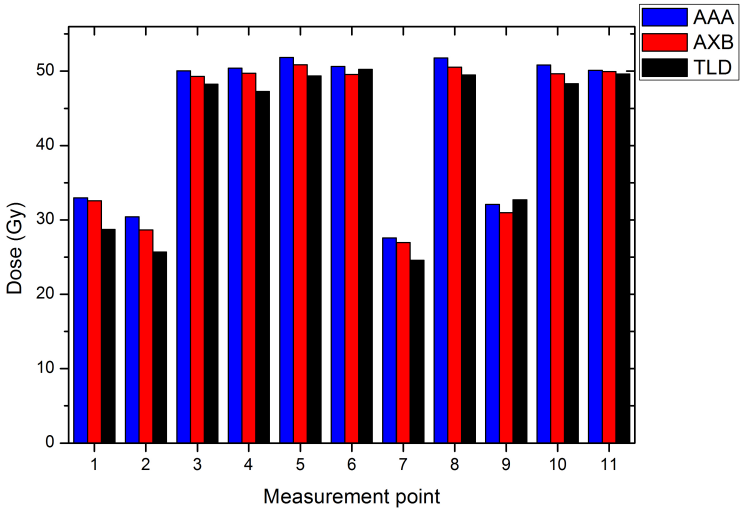

(a) Dose

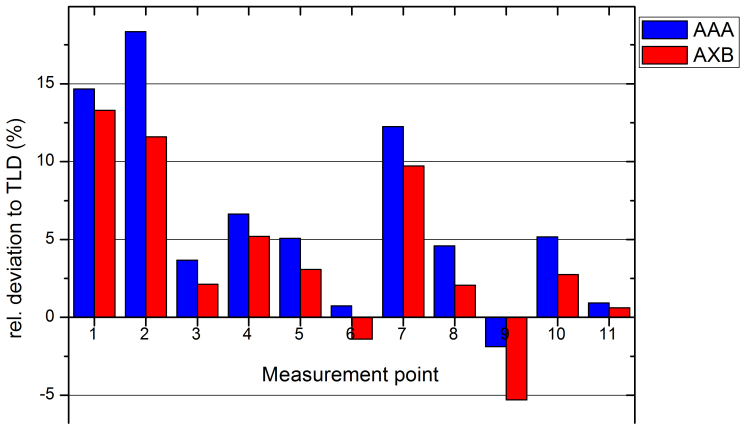

(b) rel. deviation to measurement

Figure 5.20: Point doses in the ATOM phantom for the head and neck treatment plan: TLD measurements and AAA and AXB calculations

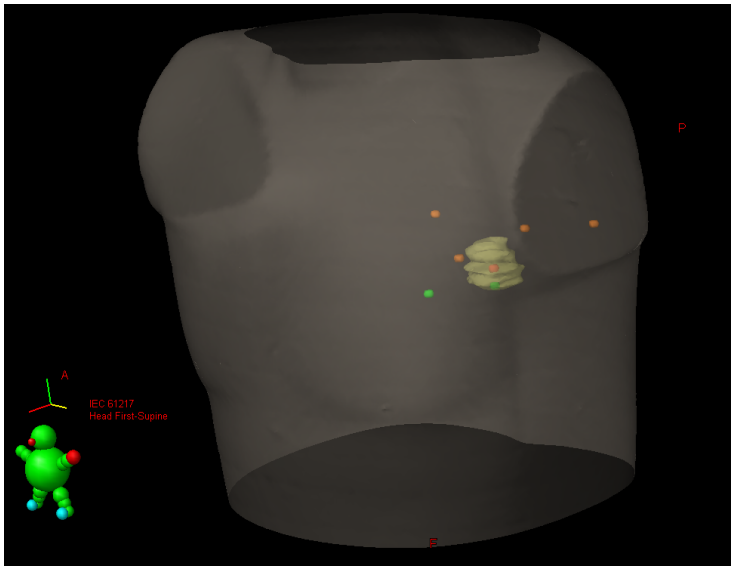

Figure 5.21: Positions of the 7 TLDs and the PTV in the lung region. Points of the same color are in the same phantom layer. The red point is located in the middle of one layer.

7 measurement points and 5.22b depicts the relative deviations of the AAA and AXB simulations to the measurement.

As in the head and neck case, the accuracy of the two algorithms cannot be compared because the measuring error of the TLDs is too high. In the treatment of lung tumors highly precise radiation fields are used, resulting in high dose gradients around the target volume. This leads to additional errors since the position of a TLD chip can only be determined with limited precision on the CT slices in the TPS.

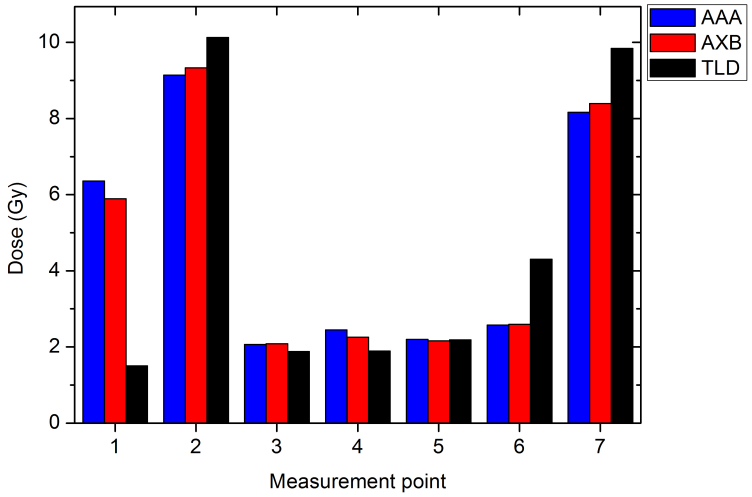

(a) Dose

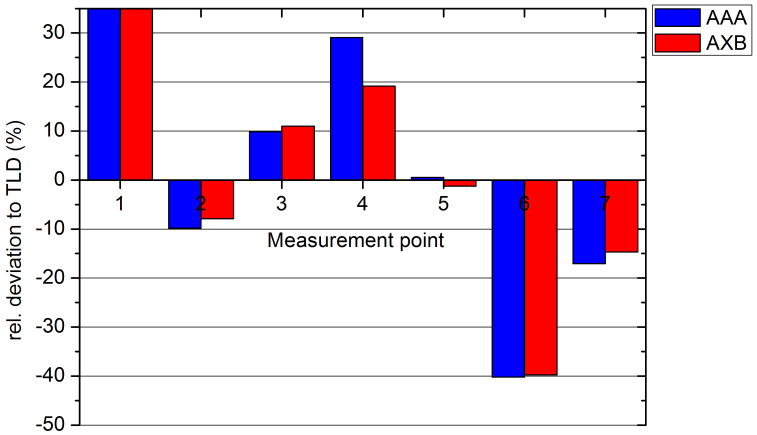

(b) rel. deviation to measurement

Figure 5.22: Point doses in the ATOM phantom for the lung treatment plan: TLD measurements and AAA and AXB calculations. The measurement at point 1 failed completely

6 Dosimetric study for clinical cases

In chapter 5 the accuracy of the Acuros XB algorithm was investigated experimentally in phantoms. The aim of this section is the analysis of the dosimetric impact of using AXB in treatment plans of a cohort of real patients. CT datasets from 11 patients were selected from the patient archive. Five Patients with head and neck tumors and 6 patients with lung tumors were selected as these regions feature tissue of different densities. The radiation treatment plans were recalculated with the Acuros XB algorithm and the changes in the dose distributions were analyzed.

6.1 Head and neck tumors

Five patients with head and neck region tumors were selected. The original radiation treatment plans were all VMAT plans with two arcs. The dose prescription had a range of 49-56 Gy delivered in 25 fractions for 4 patients and in 32 fractions for one patient. The treatment plans were originally planned in the Pinnacle TPS (Philips) and the dose distribution was calculated with the Collapsed Cone Convolution Superposition (CCCS) algorithm. The treatment plans including the CT scans, with contours of the planning target volume (PTV) and the organs at risk (OAR), were imported into the Eclipse TPS. Figure 6.1 shows the view of one of the head and neck patients in the TPS with contours of the PTV and some OAR.

The dose distributions of the treatment plans were recalculated in Eclipse with the same number of monitor units by the dose calculation algorithms Acuros XB and AAA. The Acuros XB algorithm was used in dose-to-medium mode (D_M). For comparing the three resulting dose distributions, isodose curves were inspected, cumulative dose volume histograms (DVH) were produced and dose values for the PTV and OAR were determined.

6.1.1 Isodose curves

Figure 6.2 shows four 2D-isodose curves on one CT slice of one head and neck patient as calculated by the three algorithms. The slice intersects the PTV. Differences in the three dose distributions are clearly visible. Only in the CCCS calculation, the 100% isodose fully covers the whole air section, whereas the dose decreases a little in air in the AAA calculation. In both algorithms, CCCS and AAA, spots with doses higher than 105% occur. The AXB dose distributions exhibits the smallest area with a dose of 100% and higher, and the maximum dose is below 105%. The AXB calculation is the only, where the dose in the air section drops considerably, below 90%. The

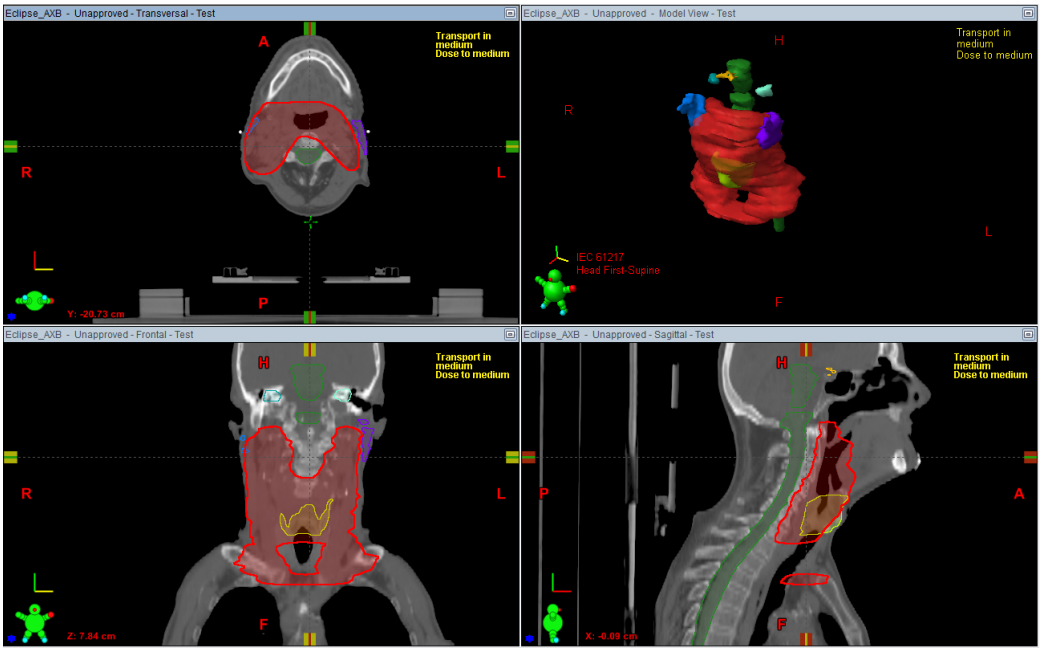

Figure 6.1: View of a head and neck tumor patient in the treatment planning system. The target volume (red) and organs at risk are contoured.

outer 90% and 95% isodose curves are almost identical for all three dose distributions. For this one patient, it can be stated that AXB calculates the lowest overall dose of the three algorithms.

6.1.2 Dose volume histograms

The cumulative dose volume histogram for the OAR in one patient calculated by the three different algorithms CCCS, AAA and AXB D_M is shown in Fig. 6.3. The following OAR are included: spinal cord, parotid glands, larynx, optic chiasm and inner ears. Whereas CCCS and AAA show very similar DVHs, the dose in the AXB calculation is a little lower resulting in a shift to the left of the DVH curves. This trend can only be seen in the OAR receiving high doses, not in the optic chiasm and the inner ears, which receive less than 10% of the prescription dose.

To assess the dosimetric impact to PTVs due to materials of different densities, the bony structures and air cavities included in the target volumes were contoured separately based on HU values. The rest of the target volumes were contoured as PTV in tissue. The DVH for the whole PTV in one patient calculated by CCCS, AAA and AXB D_M is shown in Fig. 6.4. The DVH for the bone, air and tissue sections of the PTV is shown in Fig. 6.5.

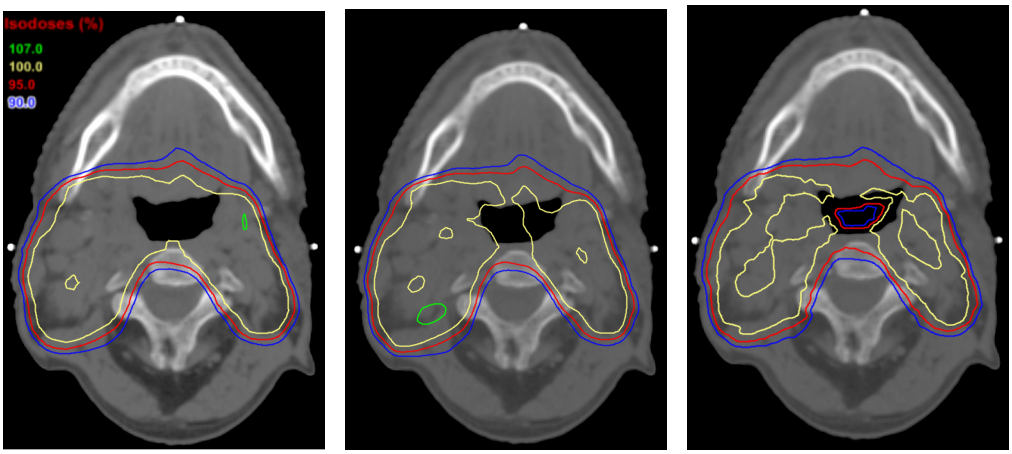

(a) CCCS (b) AAA (c) AXB

Figure 6.2: Isodose curves on one CT slice calculated by CCCS, AAA and AXB for one head and neck tumor patient. The prescription dose is 49.51 Gy

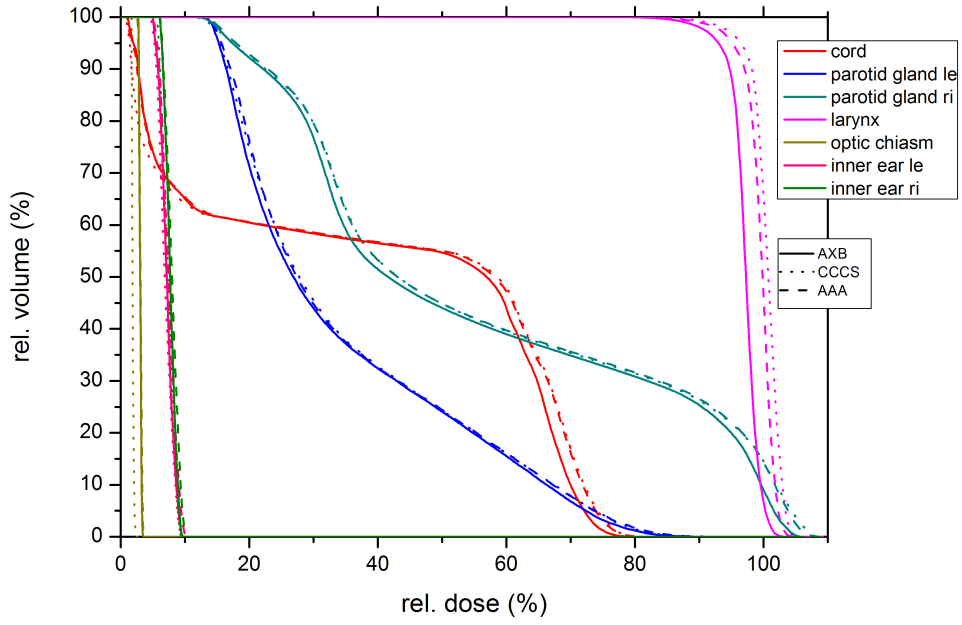

Figure 6.3: Dose volume histogram curves for organs at risk in a head and neck tumor patient calculated with three algorithms: CCCS, AAA and AXB D_M. The prescription dose is 49.51 Gy

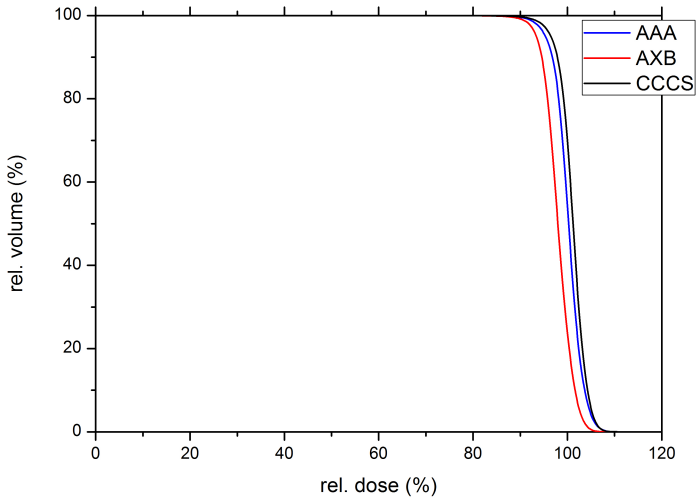

Figure 6.4: Dose volume histogram curves for PTV in a head and neck tumor patient calculated with three algorithms: CCCS, AAA and AXB D_M. The prescription dose is 49.51 Gy

The DVHs for the whole PTV show a very similar curve for the AAA and CCCS calculations. The DVH curve for the AXB is shifted to lower doses. When examining the sectioned PTV, it can be seen that the DVH curves for the tissue section are almost identical to the curves for the whole PTV. In the DVH of the bone section the shift of the AXB curve to lower doses is even more distinctive. The DVH curve for AXB in the air section has a different shape. It is less steep than the curves of the other two algorithms, but coincides with the AAA curve at doses over 100% of the prescription dose.

6.1.3 Dose value comparison

For a more quantitative comparison of the dose to the PTV and the OAR several dose parameters were investigated. The mean dose D_{mean} is the mean dose in an organ. D_{max} and D_{min} are the maximum and minimum dose, but these two parameters are not recommended for dose reporting [61]. Better dose predictors are the near-minimum, $D_{98\%}$, and near-maximum, $D_{2\%}$, dose values. $D_{2\%}$ is the highest dose which is absorbed by 2% of the volume of the organ. $D_{98\%}$ is the highest dose which is absorbed by 98% of the volume. These two parameters can be read from the DVH.

These five dose parameters were determined for the PTV and its sec-

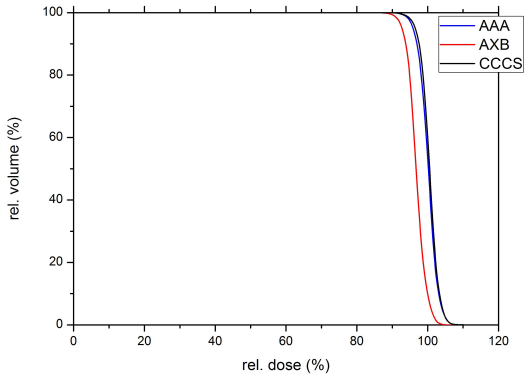

(a) PTV bone

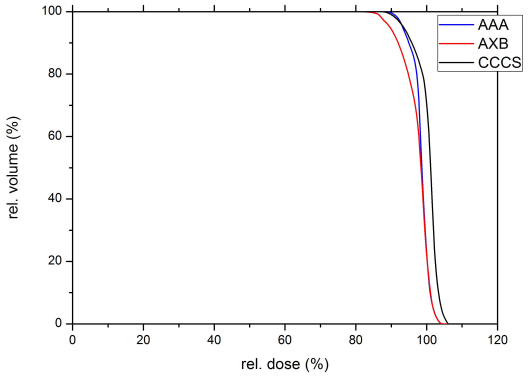

(b) PTV air

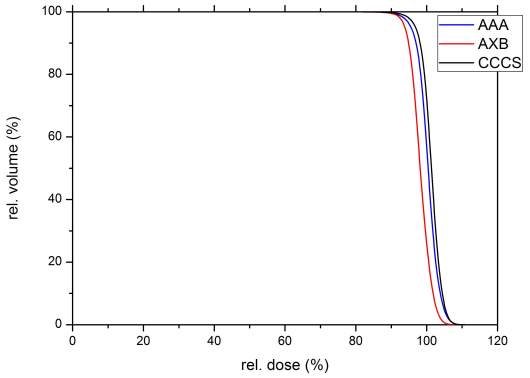

(c) PTV tissue

Figure 6.5: Dose volume histogram curves for PTV sections: bone, air and tissue calculated with three algorithms: CCCS, AAA and AXB D_M. The prescription dose is 49.51 Gy

tions (bone, air, tissue) for all five patients, they are depicted in Tab. 12 (exluding D_{max} and D_{min}). For the OAR only the maximum dose D_{max}, the near-maximum dose $D_{2\%}$ and the mean dose D_{mean} were inspected. Since all treatment plans were originally planned and calculated in the Pinnacle TPS with the CCCS algorithm, the dose distribution calculated by the CCCS is taken as reference. The relative deviations of the parameters in the AAA and AXB calculations were calculated. The average deviations were determined from the 5 patients and are depicted in Fig. 6.6. The significant dose parameters $D_{2\%}$, $D_{98\%}$ and D_{mean} clearly show a lower calculated dose from the Acuros algorithm compared to CCCS and AAA. The relative deviation of the minimum dose D_{min} exhibits a very large standard deviation, indicating that this dose parameter is not useful. The quantities D_{min} and D_{max} may be governed by a dose outlier, a voxel exhibiting a very low or high dose.

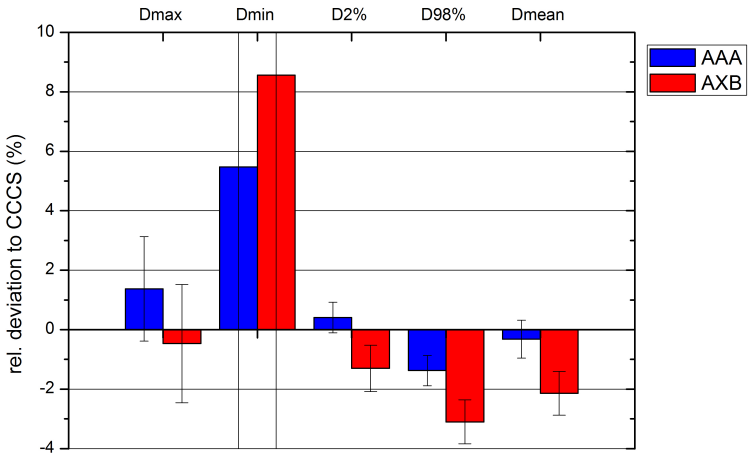

(a) PTV

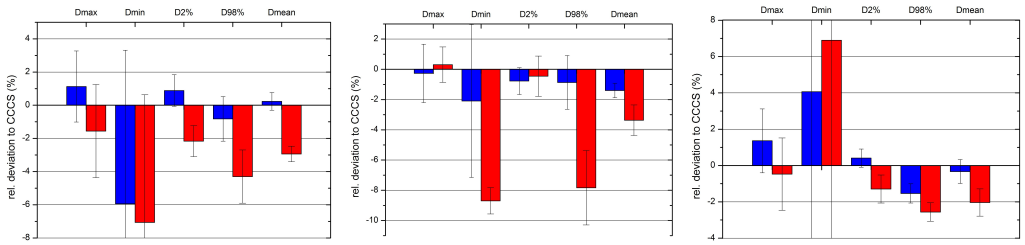

(b) PTV bone (c) PTV air (d) PTV tissue

Figure 6.6: Average relative deviations to CCCS of dose parameters of the planning target volume and sections

Table 12: Maximum ($D_{2\%}$), minimum ($D_{98\%}$) and mean dose to the planning target volume calculated by CCCS, AAA and AXB for 5 head and neck tumor patients

		PTV			**PTV bone**			**PTV air**			**PTV tissue**		
Patient	**Algorithm**	$D_{2\%}$**(Gy)**	$D_{98\%}$ **(Gy)**	D_{mean} **(Gy)**	$D_{2\%}$**(Gy)**	$D_{98\%}$ **(Gy)**	D_{mean} **(Gy)**	$D_{2\%}$**(Gy)**	$D_{98\%}$ **(Gy)**	D_{mean} **(Gy)**	$D_{2\%}$**(Gy)**	$D_{98\%}$ **(Gy)**	D_{mean} **(Gy)**
1	CCCS	52.6	46.8	50.0	52.1	47.1	49.7	52.0	45.2	49.7	52.6	47.0	50.1
	AAA	52.5	46.2	49.6	52.1	46.8	49.6	50.9	45.5	48.7	52.5	46.3	49.7
	AXB	51.4	45.5	48.5	50.5	45.3	48.2	50.9	43.2	48.2	51.4	45.8	48.6
2	CCCS	52.6	48.7	50.7	52.6	48.4	50.5	51.4	48.9	50.5	52.6	48.8	50.7
	AAA	53.1	48.4	50.8	53.0	48.0	50.8	51.2	48.1	49.7	53.1	48.5	50.8
	AXB	52.4	47.7	50.0	51.8	46.6	49.3	51.9	43.5	49.2	52.4	47.9	50.0
3	CCCS	54.1	44.5	50.4	53.7	42.4	49.6	52.7	43.3	49.9	54.2	44.9	50.6
	AAA	54.1	43.9	49.9	53.8	42.4	49.5	52.1	43.9	49.0	54.1	44.1	50.0
	AXB	53.1	43.0	49.0	52.1	40.8	47.9	51.9	40.0	47.3	53.2	43.8	49.2
4	CCCS	54.2	45.0	50.6	54.7	39.5	49.8	52.0	44.6	49.8	54.3	45.3	50.8
	AAA	54.6	44.1	50.6	56.0	38.3	49.9	52.1	43.4	49.3	54.6	44.5	50.7
	AXB	53.8	43.2	49.7	54.2	36.7	48.2	52.4	41.3	48.2	53.8	43.8	49.9
5	CCCS	72.5	52.3	59.9	72.3	52.3	59.9	72.2	53.9	63.2	72.5	52.2	59.8
	AAA	72.9	51.4	60.2	72.9	52.4	60.4	72.0	52.8	62.7	72.9	51.3	60.1
	AXB	71.6	50.6	59.1	70.5	50.6	58.3	72.0	49.0	61.4	71.6	50.9	59.1

Table 13 shows the the dose parameters for the OAR for all patients and calculations and Tab. 14 shows the average relative deviations of the parameters to CCCS for AAA and AXB. As already stated the maximum dose is not a reliable parameter, therefore only $D_{2\%}$ and D_{mean} are presented. Again a trend of lower calculated dose by AXB can be seen, but not as significant as in the PTV. Only the inner ears exhibit a higher dose in the AXB calculation. The larynx is not contoured on the data set of patient 2 and no dose value to this organ could be determined.

Table 13: Maximum ($D_{2\%}$) and mean dose to the organs at risk calculated by CCCS, AAA and AXB for 5 head and neck tumor patients

		Myelon		**Larynx**		**Parotid gland left**		**Parotid gland right**		**Inner ear left**		**Inner ear right**	
Patient	**Algorithm**	$D_{2\%}$**(Gy)**	D_{mean} **(Gy)**	$D_{2\%}$**(Gy)**	D_{mean} **(Gy)**	$D_{2\%}$**(Gy)**	D_{mean} **(Gy)**	$D_{2\%}$**(Gy)**	D_{mean} **(Gy)**	$D_{2\%}$**(Gy)**	D_{mean} **(Gy)**	$D_{2\%}$**(Gy)**	D_{mean} **(Gy)**
1	CCCS	37.7	19.9	51.4	49.7	39.1	17.6	52.6	28.0	4.5	3.4	4.5	3.6
	AAA	37.6	20.0	50.9	49.2	39.3	17.6	52.2	28.1	4.8	3.7	4.9	4.0
	AXB	36.7	19.6	50.1	48.1	38.5	17.2	51.2	27.4	4.6	3.6	4.6	3.8
2	CCCS	33.3	24.7	-	-	51.6	15.1	52.0	16.3	1.6	1.3	1.7	1.4
	AAA	33.5	24.7	-	-	50.9	15.2	52.7	16.6	1.9	1.5	1.8	1.5
	AXB	32.7	24.1	-	-	50.4	14.9	50.4	16.3	1.9	1.6	1.9	1.6
3	CCCS	35.6	19.4	45.9	20.4	54.0	25.1	52.7	23.9	6.8	5.0	6.3	4.6
	AAA	35.5	18.4	46.8	20.4	54.6	25.1	53.2	24.3	7.4	5.4	6.9	5.1
	AXB	34.8	18.0	44.8	19.8	53.7	24.6	52.2	23.8	6.9	5.1	6.5	4.8
4	CCCS	34.5	17.6	50.6	20.6	56.1	24.5	48.8	19.7	20.4	11.5	19.1	11.8
	AAA	34.6	16.9	48.8	20.8	56.5	24.5	46.7	19.2	22.2	12.1	20.7	12.6
	AXB	34.1	16.4	47.0	19.9	55.2	24.0	45.6	18.8	20.8	11.4	19.3	11.8
5	CCCS	45.1	24.9	61.5	53.1	57.4	27.0	71.8	49.1	14.4	7.6	19.6	10.1
	AAA	45.9	25.1	63.0	53.4	57.9	27.0	72.1	49.2	17.3	8.6	21.8	11.1
	AXB	44.7	24.4	61.3	52.2	56.4	26.4	70.5	48.5	16.0	8.2	20.4	10.5

Table 14: Average relative deviations of dose parameters $D_{2\%}$ and D_{mean} for the organs at risk in the AAA and AXB calculations with reference to CCCS

Organ	Algorithm	rel. dev. $D_{2\%}$ (%)	rel. dev. D_{mean} (%)
Myelon	AAA	0.42±0.88	-1.70±2.88
	AXB	-1.80±0.78	-4.05±2.70
Larynx	AAA	-0.04±2.83	0.07±0.80
	AXB	-3.07±2.89	-2.87±0.73
Parotid gland left	AAA	0.40±0.95	0.15±0.29
	AXB	-1.53±0.61	-1.84±0.45
Parotid gland right	AAA	-0.48±2.29	0.43±1.85
	AXB	-3.04±2.16	-1.66±1.90
Inner ear left	AAA	11.85±5.57	9.67±4.54
	AXB	7.09±8.12	6.73±9.84
Inner ear right	AAA	9.06±1.21	8.95±1.62
	AXB	4.60±5.01	6.24±7.06

6.2 Lung tumors

Six patients with lung tumors were selected for this part of the study. The treatment plans were stereotactic body radiation therapy (SBRT) plans delivered by arcs. The prescription dose was 60 Gy for 5 patients and 55 Gy for one patient. The prescription dose in these plans was chosen as the minimum dose, which should be delivered to 95% of the planning target volume. The prescription dose is also called the reference dose, D_{ref}. Therefore the isodose volume of the reference dose and the PTV should overlap. The dose was delivered in 5 or 8 fractions.

The treatment plans were also originally planned in the Pinnacle TPS and calculated with the CCCS algorithm. The same procedure as for the head and neck patients (see sec. 6.1) was applied, the plans were imported into the Eclipse TPS and recalculated with the AAA and AXB D_M algorithms. Figure 6.7 shows the view of one lung tumor patient in the TPS. The dose distribution calculated by AXB is indicated by the color wash. The contours of the PTV (red) and the D_{ref} isodose (green) are included and show a good overlap. The dose is delivered by three arcs.

6.2.1 Isodose curves

Figure 6.8 shows five 2D isodose curves on one CT slice of one lung tumor patient as calculated by the three algorithms. Only the ipsilateral lung is shown. The slice intersects the PTV. The three dose distributions are very similar in overall. The only notable difference is in the 100% isodose, which covers the largest area in AAA and a little smaller area in CCCS and AXB

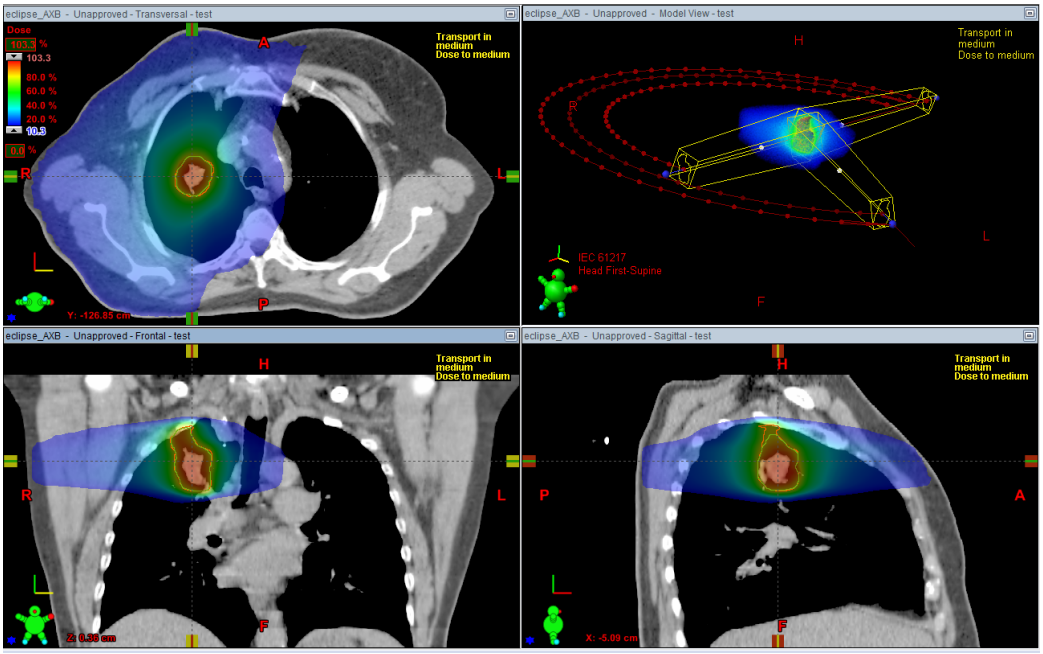

Figure 6.7: View of a lung tumor patient in the treatment planning system. The planning target volume (red) and D_{ref}=60 Gy isodose (green) are contoured.

calculations.

6.2.2 PTV parameters

To compare the three different dose calculations of the treatment plans quantitatively, several parameters were determined, which describe the conformity of PTV coverage. These parameters are routinely used in the evaluation of treatment plans for lung tumors. From the dose distributions the volume of the prescription isodose V_{RefIso} as well as the volume of the 50% prescription isodose $V_{50\%Ref}$ were calculated in the TPS. The overlap volume, PTV_{RefIso}, of the PTV and the prescription isdose volume V_{RefIso} was determined. Table 15 shows the values of reference doses and PTV volumes, V_{PTV}, of the 6 treatment plans.

For each calculation of a treatment plan the following parameters were

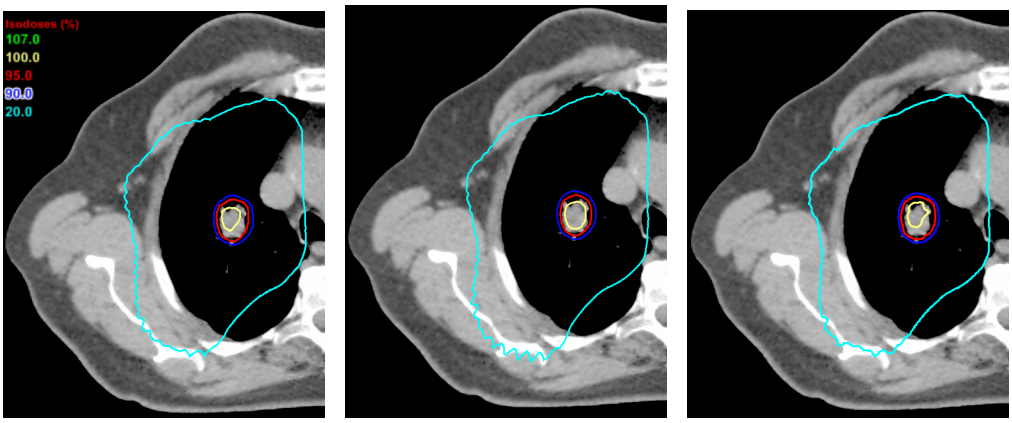

(a) CCCS (b) AAA (c) AXB

Figure 6.8: Isodose curves on one CT slice calculated by CCCS, AAA and AXB for one lung tumor patient. The prescription dose is 73.34 Gy

Table 15: Reference dose D_{ref}, number of fractions and planning target volume size for 6 lung tumor patients

Patient	**Ref. dose (Gy)**	**fractions**	V_{PTV} **(cm^3)**
1	60	5	28.5
2	60	8	20.9
3	60	5	31.1
4	60	8	32.9
5	60	8	116.7
6	55	5	74.1

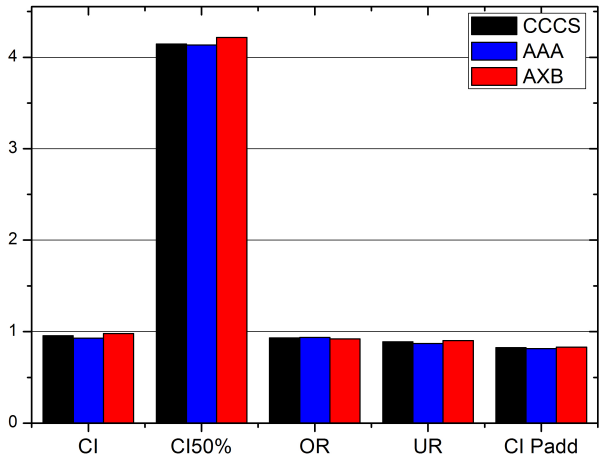

Figure 6.9: Target volume conformity parameters for patient 1 as calculated with CCCS, AAA and AXB

determined:

$$\begin{aligned} CI &= V_{RefIso}/V_{PTV} \\ CI_{50\%} &= V_{50\%Ref}/V_{PTV} \\ OR &= PTV_{RefIso}/V_{RefIso} \\ UR &= PTV_{RefIso}/V_{PTV} \\ CI_{Padd} &= PTV^2_{RefIso}/(V_{PTV} \times V_{RefIso}) \end{aligned}$$

CI and $CI_{50\%}$ are conformity indices defined after ICRU Report 62 [62]. OR and UR are the overtreatment and undertreatment ratio, and the last parameter CI_{Padd} is the Paddick conformity index [63]. Figure 6.9 shows these parameters for the three calculations of the treatment plan of patient 1. No significant deviations between the three algorithms can be seen in that plot. The parameters for all 6 patients are given in Tab. 16.

The relative deviations of these parameters to the CCCS algorithm, which is taken as reference, were calculated for the AAA and AXB algorithms. The average relative deviations were determined from the 6 patients and are depicted in Fig. 6.10. As can be seen from the very high standard deviations, no clear trend in the calculation of these parameters with different algorithms is noticeable.

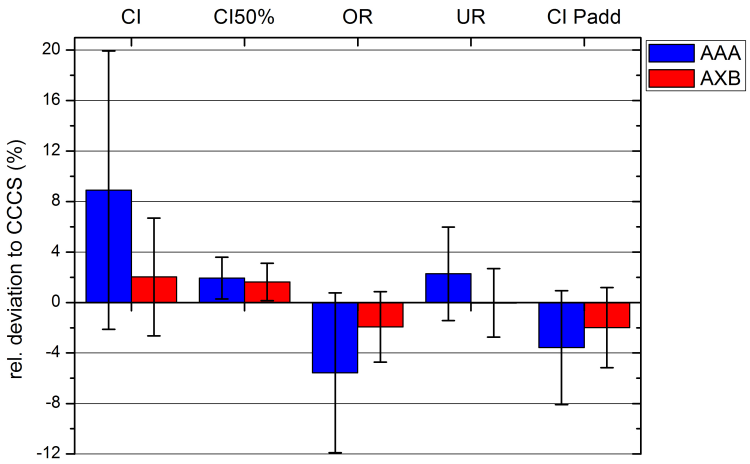

Figure 6.10: Average relative deviation of conformity parameters with reference to CCCS

Table 16: Conformity and healthy tissue parameters calculated by CCCS, AAA and AXB for 6 lung tumor patients

Patient	Algorithm	CI	$CI_{50\%}$	OR	UR	CI_{Padd}	$V_{105\%}$(cm^3)	$D_{2cm,max}$(Gy)	V_{20Gy}(%)
1	CCCS	0.95	4.14	0.93	0.89	0.83	0.11	29.04	4.98
	AAA	0.93	4.13	0.94	0.87	0.81	0.14	29.35	5.03
	AXB	0.98	4.22	0.92	0.90	0.83	0.15	29.40	5.08
2	CCCS	1.11	6.06	0.87	0.96	0.83	0.14	35.11	3.10
	AAA	1.11	6.13	0.86	0.96	0.82	0.09	34.63	3.13
	AXB	1.11	6.06	0.86	0.95	0.82	0.11	35.86	3.17
3	CCCS	0.89	4.55	0.91	0.81	0.74	0.27	35.62	3.78
	AAA	0.92	4.60	0.90	0.82	0.74	0.13	35.55	3.84
	AXB	0.89	4.60	0.92	0.82	0.75	0.21	36.15	3.86
4	CCCS	1.22	6.15	0.81	0.98	0.80	0.64	49.00	4.67
	AAA	1.36	6.30	0.73	0.99	0.72	1.51	47.00	4.78
	AXB	1.31	6.36	0.75	0.99	0.75	1.44	46.70	4.89
5	CCCS	0.99	4.73	0.86	0.86	0.74	1.70	43.04	5.55
	AAA	1.27	4.83	0.73	0.93	0.68	12.30	42.76	6.04
	AXB	0.94	4.73	0.86	0.81	0.70	3.40	42.63	5.74
6	CCCS	1.16	5.84	0.80	0.93	0.74	2.16	43.57	9.45
	AAA	1.30	6.11	0.75	0.98	0.73	4.41	43.35	9.85
	AXB	1.23	6.02	0.77	0.95	0.73	3.63	42.63	9.89

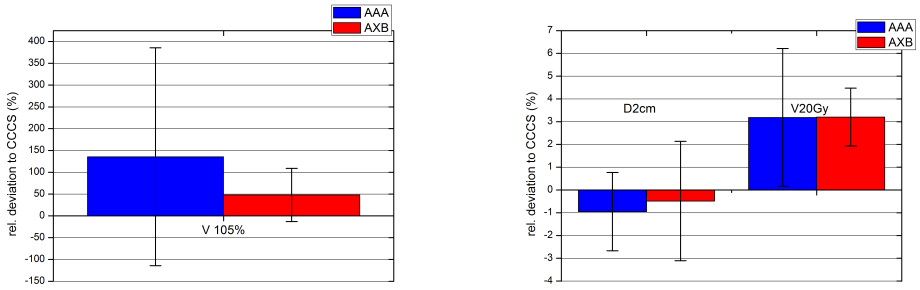

(a) $V_{105\%}$ (b) $D_{2cm,max}$, V_{20Gy}

Figure 6.11: Average relative deviations of healthy tissue parameters with reference to CCCS

6.2.3 Healthy tissue parameters

Additionally to the parameters in sec. 6.2.2, which describe the conformity of the PTV and the isodose, parameters describing the dose to healthy tissue are compared. These parameters are:

$V_{105\%}$: High dose spillage, it is the cumulative volume outside the PTV receiving a dose higher than 105% of the prescription dose.

$D_{2cm,max}$: intermediate dose spillage, is the maximum dose in healthy tissue excluding a margin of 2 cm around the PTV.

V_{20Gy}: is the relative volume of the healthy lung, which receives a dose higher than 20 Gy.

Table 16 shows these parameters for the 6 treatment plans in all three calculations CCCS, AAA and AXB D_M.

The average relative deviations of the parameters to the CCCS calculation was determined for AAA and AXB. The result is shown in Fig. 6.11. No trend in deviation is seen for the $V_{105\%}$ and $D_{2cm,max}$ parameters between the three algorithms. The V_{20Gy} parameter is in average 3% higher in the AXB calculation compared to the CCCS plan. Assuming that AXB is the more accurate dose calculation algorithm, the treatment plans for lung tumors, created in the Pinnacle TPS, may have underestimated the volume of healthy tissue receiving a dose higher than 20 Gy.

6.3 Dose calculation time

The dose calculation time of AAA and AXB for the treatment plans analyzed in secs. 6.1 and 6.2 was compared. The mean calculation time for a head and

neck treatment plan and for a lung treatment plan was determined, as well as the average time difference of an AXB calculation to an AAA calculation for both treatment regions. The results are depicted in Tab. 17.

Table 17: Dose calculation times recorded for AAA and AXB for 5 head and neck plans and 6 lung plans

	mean calc. time (±sd) (s)		**av. rel. diff. AXB-AAA**
	AAA	**AXB**	
head and neck	818(±591)	511(±154)	-15.4%
lung	95(±33)	104(±16)	19.2%

For both algorithms, the head and neck tumor plans have a substantially higher calculation time than the lung plans. For the head and neck cases calculated by AXB the mean time is about 5 minutes lower than by AAA and one plan needs on average 15% less time when calculated by AXB instead of AAA.

In the lung case, both algorithms take on average 1.5 minutes to calculate the dose in the treatment plan. Here AXB performs worse, it is 19% slower in dose calculation on average.

The recorded times have to be considered with care. For a direct comparison of calculation times, the utilized CPU capacity has to be constant over all dose calculations. This can not be guaranteed in this case, as the workstations are also used for routine treatment planning constantly, which may take up CPU power. The results therefore can only a give a rough estimate of the calculation time of an algorithm.

7 Summary and conclusion

The scope of this work was the implementation and evaluation of the Acuros XB dose calculation algorithm in the Eclipse treatment planning system for use in clinical photon radiation therapy.

Implementation

The configuration of the algorithm's source model in the treatment planning system was achieved by comparison of calculated depth dose curves and dose profiles to measured ones. The physical parameters of the source model were optimized. The optimal value for the effective target spot size was determined with 1x1 mm^2. This value leads to the best overall agreement with the measurements, especially for small field sizes which are important in modern radiotherapy techniques. The parameter values for the electron contamination were derived by an automatic optimization process.

Experimental validation

For the experimental evaluation of the AXB algorithm, at first only single open fields were used. The AXB-calculated dose distributions in the Arc-CHECK phantom (sec. 5.1.1) and the slab phantom (sec. 5.2.2) are in very good agreement to dose distributions measured with radiochromic films. A Gamma index evaluation yields a Gamma agreement index of more than 90% (criterion: 3 mm/3%) for all film positions, except for two films in the slab phantom (D1: 89.6%, D2: 79.9%), for AXB in dose-to-medium (D_M) mode. The established AAA algorithm performs considerably worse, with an GAI below 90% for all measurements, and obvious problems of dose overestimation behind air gaps. The AXB in dose-to-water (D_W) mode shows worse agreement with the film measurements than the D_M mode, but is still better than AAA in most cases. Especially close to bone material, which has a considerably higher density than water and tissue, AXB D_W overpredicts the absorbed dose. AXB D_M shows tendencies to calculate a too low dose inside bone material, AAA performs better in this case in the slab phantom. This may be due to the fact that AXB calculates the dose to bone material, whereas the film is made of tissue material. The calculation voxel size may be too large to distinguish the density difference.

Ionization chamber dosimetry was performed with a single chamber for point dose measurements (secs. 5.1.2, 5.2.2) and with a chamber array for the acquisition of 2D dose distributions (sec. 5.2.1) in the presence of heterogeneities. The agreement of AXB D_M and D_W was found to be in the range

of 2% for the point measurements. In the ArcCHECK phantom the AAA has a little better agreement with the chamber measurement, but performs worse in the slab phantom, especially behind an air gap. The chamber array 'seven29' measured the dose distribution under two different setups of slabs with two field sizes (sec. 5.2.1). The AXB calculation is in good accordance the the measurement, with Gamma agreement higher than 90% (2 mm/2%). AAA shows equal accuracy behind bone, tissue and lung-equivalent structures, but exhibits larger discrepancies behind air. A difference with the two field sizes (10x10 and 20x20 cm^2) could not be observed.

One experiment was performed to measure the doses resulting from multiple clinical VMAT fields in an anthropomorphous phantom with thermoluminescence dosimetry (sec. 5.3). The measurement technique using TLD chips turned out not to be precise enough to evaluate the accuracy of the AXB algorithm and compare it to the AAA.

Dosimetric study in clinical cases

The dosimetric implications of recalculating clinical lung and head and neck treatment plans with the Acuros algorithm were assessed. For the head and neck case the isodose curves changed noticeable, indicating a lower overall dose in the AXB calculation compared to CCCS and AAA. The dose volume histograms for the PTV and the OAR indicate a lower dose in the AXB plans than in the AAA and CCCS plans.

The mean dose to PTV is 1-2% lower in the AXB plans than in the AAA and CCCS plans. In the bone section of the PTV this difference is higher with 3% and in the air section it is 3% to the CCCS plans and 1.5% to the AAA plans. Also the maximum ($D_{2\%}$) and the minimum dose ($D_{98\%}$) to PTV and its sections are in general lower in the AXB plans. The largest difference occurs in the air section of the PTV where $D_{98\%}$ is 7-8% lower in the AXB plans. For the OAR the mean and maximum dose is 1.5-4% lower in the AXB plans. For the inner ears, which lie outside the field in the low dose region, this trend cannot be seen. Another study [23] reported similar effects of lower dose estimation in the PTV and OAR in AXB head and neck plans.

In the lung patients, the conformity of dose and target volume was investigated. In this study, no significant change in the dose conformity in the AXB lung plans was observed. Another study [64] reports a significantly lower CI parameter in AXB lung plans compared to AAA plans, this is also indicated here but with a high uncertainty.

Conclusion

The investigations in this study showed that the Acuros XB algorithm is able to calculate dose distribution with high accuracy in the presence of heterogeneous media, even near interfaces of materials with high density differences. The algorithm shows equivalent or better accuracy than the established superposition/convolution algorithm AAA in the same treatment planning system. The computational effort for calculating a VMAT plan with AXB is comparable to AAA.

The flaws of the AAA can be credited to the indirect modeling of the secondary electron transport through scatter kernels. It assumes that the depth-directed and lateral components of the kernel can be scaled independently. The lateral scaling is calculated radially from the origin of the beamlet and neglects the divergent scatter from upper levels [65]. This leads to errors at air-material interfaces in form of dose overpredictions.

Acuros simulates the full particle transport explicitly, but discretization errors may induce errors in the dose calculation. Also, the energy cutoff may lead to errors in or after low density material.

The differences between AXB and AAA are smaller for clinical VMAT fields than for extreme situations with single open fields. Still, AAA slightly overestimates the dose to target volumes and organs relative to AXB. If Acuros is used for treatment planning, more dose will be delivered to the tumor assuming that the prescribed dose remains the same. Whether this change would have clinical impact, is subject to further research.

References

[1] N. Papanikolaou et al. Tissue Inhomogeneity Corrections for Megavoltage Photon Beams. Technical Report 85, American Association of Physicists in Medicine, 2004.

[2] E. Lewis and W. Miller Jr. *Computational methods of neutron transport.* Wiley, 1984.

[3] K. Gifford, J. Horton, T. Wareing, et al. Comparison of a finite element multigroup discrete-ordinates code with Monte Carlo for radiotherapy calculations. *Phys. Med. Biol.*, 51:2253–2265, 2006.

[4] O. Vassiliev, T. Wareing, I. Davis, et al. Feasibility of a multigroup deterministic solution method for three-dimensional radiotherapy dose calculations. *Int. J. Radiat. Oncol. Biol. Phys.*, 72:220–227, 2008.

[5] T. Wareing, J. McGhee, J. Morel, et al. Discontinuous finite element Sn methods on 3-D unstructured grids. *Nucl. Sci. Eng.*, 138:256–268, 2001.

[6] O. Vassiliev, T. Wareing, J. McGhee, G. Failla, M. Salehpour, and F. Mourtada. Validation of a new grid-based Boltzmann equation solver for dose calculation in radiotherapy with photon beams. *Phys. Med. Biol.*, 55:581–598, 2010.

[7] K. Bush, I. Gagne, S. Zavgorodni, et al. Dosimetric validation of Acuros XB with Monte Carlo methods for photon dose calculations. *Med. Phys*, 38:2208–2221, 2011.

[8] M. Kan, P. Yu, and L. Leung. A review on the use of grid-based Boltzmann equation solvers for dose calculation in external photon beam treatment planning. *BioMed. Res. Int.*, 2013, 2013. Article ID 692874.

[9] A. Fogliata, G. Nicolini, A. Clivio, et al. Dosimetric validation of the Acuros XB advanced dose calculation algorithm: Fundamental characterization in water. *Phys. Med. Biol.*, 56:1879–1904, 2011.

[10] T. Han, J. Mikell, M. Salehpour, et al. Dosimetric comparison of Acuros XB deterministic radiation transport method with Monte Carlo and model-based convolution methods in heterogeneous media. *Med. Phys*, 38:2651–2664, 2011.

[11] L. Hoffmann, M. Jorgensen, L. Muren, et al. Clinical validation of the Acuros XB photon dose calculation algorithm, a grid-based Boltzmann equation solver. *Acta Oncologica*, 51:376–385, 2012.

[12] A. Fogliata, G. Nicolini, A. Clivio, et al. Dosimetric evaluation of Acuros XB Advanced Dose Calculation algorithm in heterogeneous media. *Radiation Oncology*, 6:82, 2011.

[13] S. Lloyd and W. Ansbacher. Evaluation of an analytic linear Boltzmann transport equation solver for high density inhomogeneities. *Med. Phys.*, 40:011707, 2013.

[14] M. Kan, L. Leung, and P. Yu. Verification and dosimetric impact of Acuros XB algorithm on intensity modulated stereotactic radiotherapy for locally persistent nasopharyngeal carcinoma. *Med. Phys.*, 39:4705–4714, 2012.

[15] S. Stathakis, C. Esquivel, L. Quino, et al. Accuracy of the Small Field Dosimetry Using the Acuros XB Dose Calculation Algorithm within and beyond Heterogeneous Media for 6 MV Photon Beams. *International Journal of Medical Physics, Clinical Engineering and Radiation Oncology*, 1:78–87, 2012.

[16] S. Rana and K. Rogers. Dosimetric evaluation of Acuros XB dose calculation algorithm with measurements in predicting doses beyond different air gap thickness for smaller and larger field. *J. Med. Phys.*, 38:9–14, 2013.

[17] P. Kroon, S. Hol, and M. Essers. Dosimetric accuracy and clinical quality of Acuros XB and AAA dose calculation algorithm for stereotactic and conventional lung volumetric modulated arc therapy plans. *Radiation Oncology*, 8:149, 2013.

[18] T. Han, F. Mourtada, K. Kisling, et al. Experimental validation of deterministic Acuros XB algorithm for IMRT and VMAT dose calculations with the Radiological Physics Center's head and neck phantom. *Med. Phys.*, 39:2193–2202, 2012.

[19] M. Kan, L. Leung, R. So, et al. Experimental verification of the Acuros XB and AAA dose calculation adjacent to heterogeneous media for IMRT and RapidArc of nasopharygeal carcinoma. *Med. Phys.*, 40:031714, 2013.

[20] T. Han, D. Followill, J. Mikell, et al. Dosimetric impact of Acuros XB deterministic radiation transport algorithm for heterogeneous dose calculation in lung cancer. *Med. Phys.*, 40:051710, 2013.

[21] A. Fogliata, G. Nicolini, A. Clivio, et al. Critical Appraisal of Acuros XB and Anisotropic Analytic Algorithm Dose Calculation in Advanced Non-Small-Cell Lung Cancer Treatments. *Int. J. Radiat. Oncol. Biol. Phys.*, 83:1587–1595, 2012.

[22] A. Fogliata, G. Nicolini, A. Clivio, et al. On the dosimetric impact of inhomogeneity management in the Acuros XB algorithm for breast treatment. *Radiat. Oncol.*, 6:103, 2011.

[23] M. Kan, L. Leung, and P. Yu. Dosimetric impact of using Acuros XB algorithm for intensity modulated radiation therapy and RapidArc planning in nasopharyngeal carcinomas. *Int. J. Radiat. Oncol. Biol. Phys.*, 85:73–80, 2013.

[24] E. Podgorsak. *Radiation Physics for Medical Physicists*. Springer, second edition, 2010.

[25] E. Podgorsak, editor. *Radiation Oncology Physics: A Handbook for Teachers and Students*. IAEA, Vienna, 2005.

[26] J. Seibert and J. Boone. X-Ray Imaging Physics for Nuclear Medicine Technologists. Part 2: X-Ray Interactions and Image Formation. *J. Nucl. Med. Technol.*, 33:3–18, 2005.

[27] G. Knoll. *Radiation Detection and Measurement*. John Wiley and Sons, Inc., third edition, 2000.

[28] H. Krieger. *Grundlagen der Strahlungsphysik und des Strahlenschutzes*. Teubner, second edition, 2007.

[29] K. Zink. Einführung in die Strahlentherapie und Therapie mit offenen Nukliden. Lecture notes, 2004. Mittelhessen University of Applied Sciences.

[30] International Commission on Radiation Units and Measurements. Fundamental quantities and units for ionizing radiation (revised). *Journal of the ICRU*, 11:1–33, 2011. ICRU Report No. 85a.

[31] A. Ahnesjö, P. Andreo, and A. Brahme. Calculation and application of point spread functions for treatment planning with high energy photon beams. *Acta Oncologica*, 26:49–56, 1987.

[32] A. Smith, editor. *Radiation Therapy Physics*. Springer, 1995.

[33] A. Ahnesjö and M. Aspradakis. Dose calculations for external photon beams in radiotherapy. *Phys. Med. Biol.*, 44:R99–R155, 1999.

[34] J. Cunningham. Scatter-air ratios. *Phys. Med. Biol.*, 17:43–51, 1972.

[35] P. Andreo. Monte carlo techniques in medical radiation physics. *Phys. Med. Biol.*, 36:861–920, 1991.

[36] A. De Salles et al., editors. *Shaped Beam Radiosurgery.* Springer, first edition, 2011.

[37] G. Failla, T. Wareing, Y. Archambault, and S. Thompson. *Acuros® XB advanced dose calculation algorithm for the Eclipse^{TM}treatment planning system*, 2010. product documentation, RAD 10156, Varian Medical Systems.

[38] Varian Medical Systems. Eclipse Algorithms Reference Guide. Technical Report P/N B503486R01B, 2011.

[39] T. Wareing, J. Morel, and J. McGhee. Coupled electron-photon transport methods on 3-d unstructured grids. *Trans. Am. Nucl. Soc.*, 83:240–242, 2000.

[40] International Commission on Radiological Protection. *ICRP Publication 23: Reference Man: Anatomical, Physiological and Metabolic Characteristics.* Elsevier, 1975.

[41] L. Lorence, J. Morel, and G. Valdez. Physics Guide to CEPXS: A Multigroup Coupled Electron-Photon Cross-Section Generating Code. Technical Report SAND89-1685, Sandia National Laboratories, 1989.

[42] W. Ulmer and D. Harder. A triple gaussian pencil beam model for photon beam treatment planning. *Z. Med. Phys.*, 5:25–30, 1995.

[43] W. Ulmer and W. Kaissl. The inverse problem of a Gaussian convolution and its application to the finite size of the measurement chambers/detectors in photon and proton dosimetry. *Phys. Med. Biol.*, 48:707–727, 2003.

[44] J. Sievinen, W. Ulmer, and W. Kaissl. *AAA Photon Dose Calculation Model in Eclipse^{TM}*, 2006. product documentation, RAD 7170A, Varian Medical Systems.

[45] P. Mayles, A. Nahum, and J. Rosewald. *Handbook of Radiotherapy Physics: Theory and Practice.* Taylor and Francis, first edition, 2007.

[46] Varian Medical Systems. Clinac-D Series Accelerators. `http://www.varian.com/euen/oncology/radiation_oncology/clinac/clinac_dhx_high_performance.html`. accessed: 02/01/2014.

[47] H. Krieger. *Strahlungsquellen für Technik und Medizin.* Teubner, first edition, 2005.

[48] H. Krieger. *Strahlungsmessung und Dosimetrie.* Springer, second edition, 2013.

[49] P. Andreo et al. Absorbed Dose Determination in External Beam Radiotherapy: An International Code of Practice for Dosimetry Based on Standards of Absorbed Dose to Water. Technical Report 398, International Atomic Energy Agency, 2000.

[50] A. Niroomand-Rad et al. Radiochromic film dosimetry: Recommendations of AAPM Radiation Therapy Committee Task Group 55. *Med. Phys.*, 25:2093–2115, 1998. AAPM Report No. 63.

[51] Varian Medical Systems. Millenium MLC. `http://www.varian.com/us/oncology/radiation_oncology/clinac/millennium_mlc.html`. accessed: 02/01/2014.

[52] PTW Freiburg. 2D-ARRAY seven29 with 729 Ion Chambers. `http://www.ptw.de/2d-array_seven29.html`. accessed: 02/01/2014.

[53] International Specialty Products. Gafchromic EBT3. `http://www.ashland.com/Ashland/Static/Documents/ASI/Advanced%20Materials/gafchromic-ebt3.pdf`, 2011. accessed: 02/01/2014.

[54] PTW Freiburg. Semiflex Ionization Chamber 31010. `http://www.ptw.de/semiflex_chambers0.html`. accessed: 02/01/2014.

[55] CIRS Inc. ATOM® Dosimetry Phantoms brochure. `http://www.cirsinc.com/file/Products/701_706/701_706_ATOM_PB_041613.pdf`, 2013. accessed: 19/01/2014.

[56] D. Low, W. Harms, S. Mutic, and J. Purdy. A technique for the quantitative evaluation of dose distributions. *Med. Phys.*, 25:656–661, 1998.

[57] L. Tillikainen, S. Siljamäki, H. Helminen, J. Alakuijala, and J. Pyyry. Determination of parameters for a multiple-source model of megavoltage photon beams using optimization methods. *Phys. Med. Biol.*, 52:1441–1467, 2007.

[58] Sun Nuclear Corp. ArcCHECK Density, 2012. Application note, Document 1220029 Rev B, 14 Dec. 2012.

[59] Medical Physics at Institute of Radiooncology KFJ Hospital Vienna. Calculation Grid Effects with AAA and the seven29 - The "Solution". `http://www.wienkav.at/kav/kfj/91033454/physik/729/grid_solution.htm`. accessed: 20/01/2014.

[60] E. Haas. Periphere Dosis und Risikoorgandosis bei der Strahlentherapie der Brust in Abhängigkeit von der Bestrahlungstechnik. Master's thesis, Graz University of Technology, 2013.

[61] International Commission on Radiation Units and Measurements. Prescribing, Recording, and Reporting Photon-Beam Intensity-Modulated Radiation Therapy (IMRT). *Journal of the ICRU*, 10:1–106, 2010. ICRU Report No. 83.

[62] ICRU Report 62: Prescribing, Recording and Reporting Photon Beam Therapy (Supplement to ICRU Report 50). Technical Report 62, International Commission on Radiation Units and Measurements, 1999.

[63] I. Paddick. A simple scoring ratio to index the conformity of radiosurgical treatment plans. Technical note. *J. Neurosurg. (Suppl. 3)*, 93:219–222, 2000.

[64] S. Rana, K. Rogers, S. Pokharel, et al. Evaluation of Acuros XB algorithm based on RTOG 0813 dosimetric criteria for SBRT lung treatment with RapidArc. *Journal of Applied Clinical Medical Physics*, 15:118–129, 2014.

[65] M. Kan, J. Cheung, L. Leung, et al. The accuracy of dose calculations by anisotropic analytical algorithms for stereotactic radiotherapy in nasopharyngeal carcinoma. *Phys. Med. Biol.*, 56:397–413, 2011.